INFORMATION TO USERS

This manuscript has been reproduced from the microfilm master. UMI films the text directly from the original or copy submitted. Thus, some thesis and dissertation copies are in typewriter face, while others may be from any type of computer printer.

The quality of this reproduction is dependent upon the quality of the copy submitted. Broken or indistinct print, colored or poor quality illustrations and photographs, print bleedthrough, substandard margins, and improper alignment can adversely affect reproduction.

In the unlikely event that the author did not send UMI a complete manuscript and there are missing pages, these will be noted. Also, if unauthorized copyright material had to be removed, a note will indicate the deletion.

Oversize materials (e.g., maps, drawings, charts) are reproduced by sectioning the original, beginning at the upper left-hand corner and continuing from left to right in equal sections with small overlaps.

Photographs included in the original manuscript have been reproduced xerographically in this copy. Higher quality 6" x 9" black and white photographic prints are available for any photographs or illustrations appearing in this copy for an additional charge. Contact UMI directly to order.

ProQuest Information and Learning
300 North Zeeb Road, Ann Arbor, MI 48106-1346 USA
800-521-0600

UMI®

Molecular Beam Epitaxy Growth and Characterization of Be-based II-VI Semiconductor Materials and Distributed Bragg Reflectors for Potential Application in Visible Light Emitters

by

Oleg Maksimov

A dissertation submitted to the Graduate Faculty in Chemistry in partial fulfillment of the requirements for the degree of Doctor of Philosophy, The City University of New York

2002

ProQuest Information and Learning Company
300 North Zeeb Road
P.O. Box 1346
Ann Arbor, MI 48106-1346

Approval Page

This manuscript has been read and accepted for the Graduate Faculty in Chemistry in satisfaction of the dissertation requirement for the degree of Doctor of Philosophy.

12/04/01
Date

Chair of Examining Committee

12/4/2001
Date

Executive Officer

Maria Tamargo

John Lombardi

Richard Pizer

Supervisory Committee

THE CITY UNIVERSITY OF NEW YORK

Abstract

Molecular Beam Epitaxy Growth and Characterization of Be-based II-VI Semiconductor Materials and Distributed Bragg Reflectors for Potential Application in Visible Light Emitters

by

Oleg Maksimov

Adviser: **Professor Maria Tamargo**

This thesis describes the molecular beam epitaxy (MBE) growth and characterization of $Zn_xCd_yMg_{1-x-y}Se$-based distributed Bragg reflectors (DBRs) and new $Be_xZn_yCd_{1-x-y}Se$ and $Be_xZn_{1-x}Te$ material systems on InP substrates. DBRs can be integrated with $Zn_xCd_yMg_{1-x-y}Se$-based light emitting diodes (LEDs) to fabricate resonant cavity LEDs (RCLEDs) that have better spectral purity and higher emission intensity than the conventional LEDs. The $Be_xZn_yCd_{1-x-y}Se$ alloy can be used as an active layer and the $Be_xZn_{1-x}Te$ alloy can be used as a p-type contact layer in $Zn_xCd_yMg_{1-x-y}Se$-based LEDs. Application of these materials is proposed to improve reliability as well as the optical and electrical properties of light emitters.

DBRs with different numbers of periods and different layer composition were grown by MBE from $Zn_xCd_yMg_{1-x-y}Se$-based materials on

InP substrates. Their reflectivity maxima were controlled by the individual thicknesses of constituent layers, and were adjusted in the range of 615 – 500 nm, covering the red, green, and blue - green regions of the visible spectrum. A maximum reflectivity of 95.5% was obtained for a DBR with 16 periods. Electrical properties of chlorine-doped n-type ZnCdSe/ZnCdMgSe DBR structures were also investigated and high carrier concentration was achieved in the constituent layers. These results demonstrate that $Zn_xCd_yMg_{1-x-y}Se$ is a promising material system for the design of highly reflective, conductive DBRs for application in high efficiency RCLEDs.

$Be_xZn_yCd_{1-x-y}Se$ epilayers and $Be_{0.08}Cd_{0.92}Se/Zn_{0.32}Cd_{0.25}Mg_{0.43}Se$ quantum well (QW) structures were grown and investigated. Their high crystalline quality was established using X-ray diffraction measurements. Efficient excitonic emission was observed both from the $Be_xZn_yCd_{1-x-y}Se$ epilayers and the QWs. Based on these results and on the expected lattice hardening properties of BeSe, we propose that $Be_xZn_yCd_{1-x-y}Se$ is an attractive QW material for light emitters.

The growth and optical properties of a set of $Be_xZn_{1-x}Te$ epilayers were studied. Comparison of the reflectivity and the photoluminescence spectra allowed us to locate the direct-to-indirect band gap crossover for this

alloy at $x \approx 0.28$. Our results indicated that $Be_{0.48}Zn_{0.52}Te$, which is the composition that is lattice matched to InP, is an indirect semiconductor with a $\Gamma \rightarrow X$ indirect band gap of 2.77 eV, and a $\Gamma \rightarrow \Gamma$ direct band gap of 3.14 eV. Therefore, it is transparent for the visible light and can be used as a top p-type contact layer in LEDs.

Acknowledgements

This thesis would never be completed without the guidance of my advisor Prof. M. C. Tamargo, who provided encouragement, inspiration, and help within the last four years.

I would also acknowledge the help I received from Dr. L. Zeng, Dr. Y. Y. Luo, Dr. S. P. Guo, and Dr. F. Fernandez. I also want to thank other members in the research group: Dr. M. Muñoz, Ms. X. Zhou, Mr. M. Sohel, and Mr. M. Shaheed.

I am also very grateful to my wife, Tatiana Mikhelashvili, for her support without which I could not concentrate on my research.

Contents

List of Illustrations

List of Tables

Chapter 1

Introduction

There is a wide technological interest in semiconductor lasers and light emitting diodes (LDs and LEDs) operating in the visible range of a spectrum. These devices can be used in the production of full color displays that have higher brightness and better resolution than liquid crystal displays. Currently fabricated semiconductor displays use three different material systems to produce the three primary colors: red, green, and blue (R-G-B). For example, $In_xGa_yAl_{1-x-y}N$, $Zn_xMg_{1-x}S_ySe_{1-y}$, and $In_xGa_yAl_{1-x-y}P$ material systems are used to produce blue, green, and red light emitters, respectively.[1-3] It is technologically demanding to combine these very dissimilar materials in one device. Therefore, for device integration it is of primary importance to find a single material system that can produce all three primary colors.

Our research group has previously developed $Zn_xCd_yMg_{1-x-y}Se$, a promising wide band gap material family, grown on InP substrates.[4] The band gap versus lattice constant for this material family is shown in Figure 1-1. The vertical dashed line at the center of the figure indicates the position of zero lattice mismatch to the InP substrate. The black squares represent the reported values of the binary ZnSe, CdSe, and MgSe materials. The solid

lines are the ternary boundaries of the $Zn_xCd_yMg_{1-x-y}Se$ quaternary material system. From this figure, it is clear that by adding Mg to the $Zn_xCd_{1-x}Se$ alloy and keeping lattice matched conditions, the band gap of the $Zn_xCd_yMg_{1-x-y}Se$ quaternary material can be varied from 2.18 to 3.5 eV, covering nearly all the visible spectrum, from yellow to blue.

The schematic of quantum well (QW) structures made from these materials is shown in Figure 1-2, where the top figure is the layer structure and the bottom figure is the band gap profile. The QW structures consist of a $Zn_xCd_{1-x}Se$ active layer ($E_g \sim 2.0$ eV) sandwiched between two wide band gap $Zn_xCd_yMg_{1-x-y}Se$ ($E_g \sim 3.0$ eV) barrier layers. Since the barrier layers have a larger band gap than the $Zn_xCd_{1-x}Se$ active layer, a QW is formed in which electrons and holes are confined. Since the active layer is thin (<10 nm), quantum confinement effects result in discreet energy levels in the well. In that case, the QW emission depends on the QW thickness and can be varied through most of the visible range, from yellow to blue. To obtain red emission it is possible to use pseudomorphically strained mismatched $Zn_xCd_{1-x}Se$ QW layers with excess Cd. Thus, R-G-B emission is achieved from nearly identical structures where only QW thickness and composition are varied.

The room temperature photoluminescence (PL) spectra from three $Zn_xCd_{1-x}Se$/ $Zn_xCd_yMg_{1-x-y}Se$ QW structures are shown in Figure 1-3. Spectra in the Fig 1-3 (a) and (b) correspond to the PL emission from the QW structures with 3 and 6 nm thick lattice matched active layers. The spectrum in Fig 1-3 (c) corresponds to the PL emission from a QW structure with a 6-nm thick strained ($\Delta a/a = 1.8$ %) active layer. As expected, QW emission lines are in the blue, green, and red regions of the visible spectrum.

Light emitting diodes (LEDs) based on $Zn_xCd_yMg_{1-x-y}Se$ materials and operating in the visible range of the spectrum, were demonstrated by ours as well as other research groups.[5-7] The schematic of these structures is shown in Figure 1-4. They consist of a $Zn_xCd_{1-x}Se$ QW layer sandwiched between two wide band gap $Zn_xCd_yMg_{1-x-y}Se$ barrier layers. The bottom layer is doped n-type with Cl and the top layer is doped p-type with N to create a p-n junction, necessary for current injection devices. The whole structure is capped with a p^+ $ZnSe_{0.5}Te_{0.5}$ layer that serves as a top ohmic contact layer.

Red-green-blue (R-G-B) emission was obtained from lattice-matched or pseudomorphic $Zn_xCd_yMg_{1-x-y}Se$-based structures grown on InP substrates that differed only in the QW thickness and/or composition.[5] However, the devices reported were not fully optimized. In particular, three aspects are of concern.

First, the optical properties of ZnCdMgSe-based LEDs are not ideal. Light emission from the active region is isotropic and at least 50% of the produced light is lost due to the absorption by InP substrate. Line widths of LEDs are determined by the density of states in the conduction and valence band and the thermal energy of carriers. Typical line widths are on the order of 1.8 kT (47 meV), where kT is the thermal energy. The emission lines, shown in Figure 1-4, have comparable line width (70 meV - 90 meV). [5] However, stronger emission intensity as well as better spectral purity can be achieved by structure modification, as shown later.

Second, strained $Zn_xCd_{1-x}Se$ QWs with excess Cd ($\Delta a/a \sim 1.8\%$) are used for red light emission.[8] The strain in the lattice-mismatched active layer is expected to enhance the multiplication and diffusion of point defects, decreasing the lifetime and reliability of lasers and LEDs.

Finally, the current choice of the p^+ contact layer, which can be either $ZnSe_{0.5}Te_{0.5}$ or $Zn_xMg_{1-x}Se_yTe_{1-y}$, is not optimum. In the case of $ZnSe_{0.5}Te_{0.5}$, which can be doped p-type to carrier concentrations in excess of 10^{19} cm^{-3}, absorption of the visible light by the top contact layer limits the performance of surface emitting LEDs.[9] When $Zn_xMg_{1-x}Se_yTe_{1-y}$ layers, which have a band gap of 3.1 eV and thus do not absorb in the visible range, are used, the

maximum free hole concentration is in the low 10^{18} cm^{-3}, making the formation of ohmic contacts more difficult.[6]

In this work we have addressed and propose solutions to these shortcomings of our current LEDs. We report the molecular beam epitaxy (MBE) growth and characterization of $Zn_xCd_yMg_{1-x-y}Se$-based DBR structures and of two novel Be-chalcogenide alloys: $Be_xZn_yCd_{1-x-y}Se$ and $Be_xZn_{1-x}Te$. Application of these structures and alloys in our devices is expected to improve the optical properties, electrical characteristics, and reliability of R-G-B lasers and LEDs.

The optical properties of LEDs can be dramatically improved by placement of the active region into a resonant optical cavity defined by two distributed Bragg reflectors (DBRs). First, placement of the active region into a resonant optical cavity enhances spontaneous emission. The probability for spontaneous emission is proportional to the matrix element of the initial and final electron state and proportional to the optical mode density. The optical mode density in the resonance cavity is strongly enhanced for the on-resonance wavelengths. As a consequence, on-resonance transitions of the RCLEDs are enhanced. Second, emission of light through the contact (top side) is additionally enhanced due to the highly reflective mirror adjacent to the n-type confinement layer (bottom side).

Since the bottom mirror has a higher reflectivity than the top mirror, light propagates along the optical axis of the cavity and exits the cavity predominantly through the top, eliminating absorption by the InP substrate. This can enhance an emission by about a factor of two. Third, a better spectral purity can be achieved with the RCLED. Since the spontaneous emission from the active region is constrained to emit into the modes of the optical cavity, the design of the cavity allows one to estimate the line width of the RCLED. The cavity Q of a co-planar Fabry-Perot cavity is given by:

$$Q = \nu/\Delta\nu = 2\pi\, L_c/\lambda\, [-\ln \mathrm{sqrt}\,(R_1R_2)]^{-1}$$

where L_c is the cavity length, $\Delta\nu$ and ν are the bandwidth and frequency of the Fabry-Perot resonance mode, R_1 and R_2 are the reflectivity of the top and the bottom mirror. [10] As an example, we choose $L_c = \lambda$, $h\nu = 2$ eV, $R_1R_2 = 0.9$, which yields $Q = 120$. The corresponding line width is $h\Delta\nu = 17$ meV which is much narrower than kT at room temperature.

We also propose to improve the reliability of the LEDs by using beryllium-based II-VI compounds,[11] such as $Be_xZn_yCd_{1-x-y}Se$.[12, 13] Due to a high degree of covalent bonding in Be chalcogenides,[14] introduction of BeSe in the QW region should increase the bonding energy, decreasing the formation of point defects and suppressing the propagation of extended

defects. Therefore, devices made from Be-based alloys are expected to be less prone to degradation than those made from other II-VI materials.

Finally, we explored $Be_xZn_{1-x}Te$, which is a promising alternative material for use as a p-type contact layer. This material can be lattice matched to the InP substrates with a BeTe mole fraction (x) of ≈ 0.48 and can be doped p-type to the 10^{19} cm^{-3} level.[15, 16] Also, since BeTe and ZnTe have direct band gaps of 4.1 eV [17] and 2.26 eV, it is expected that $Be_xZn_{1-x}Te$ layers lattice matched to InP will not absorb in the visible range.

In the following chapters I will discuss my work in details.

In Chapter 2, the basics of the molecular beam epitaxy (MBE) growth technique will be introduced. Also, the sample characterization techniques (X-ray diffraction, photoluminescence, and reflectivity) used will be presented.

In Chapter 3, the growth of $Zn_xCd_yMg_{1-x-y}Se$-based DBRs will be investigated. A way to calculate $Zn_xCd_yMg_{1-x-y}Se$ composition from the lattice constant measured by XRD, and band gap energy measured by photoluminescence, will be discussed. The dependence of reflectivity on the difference in the indeces of refraction of materials used (Δn) and on the number of periods in a stack (N) will be explored. Finally, the electrical properties of n-type doped DBRs will be investigated.

In Chapter 4, I will discuss the growth and characterization of the $Be_xZn_yCd_{1-x-y}Se$ material family. I will present the conditions developed for $Be_xZn_yCd_{1-x-y}Se$ growth and discuss crystalline and optical properties of the $Be_xZn_yCd_{1-x-y}Se$ epilayers. I will also establish the relationship for the $Be_xCd_{1-x}Se$ band gap dependence on composition.

Chapter 5 is devoted to the photoluminescence characterization of the optical properties of $Be_{0.08}Cd_{0.92}Se$/ZnCdMgSe strained quantum well structures. The temperature dependence of BeCdSe QW emission energy and the broadening of the QW emission line width with temperature are studied. Also the distribution of the band offsets ($\Delta E_c/\Delta E_v$) between $Be_{0.08}Cd_{0.92}Se$ and ZnCdMgSe is estimated.

In Chapter 6, I focused on the use of photoluminescence and reflectivity to explore the band structure of the $Be_xZn_{1-x}Te$ material family. The direct band gap dependence ($\Gamma \rightarrow \Gamma$) and indirect band gap dependence ($\Gamma \rightarrow X$) on composition were investigated and the position of the direct-to-indirect cross over was identified.

Finally, the summary chapter and the list of publications highlight the key achievements of this dissertation.

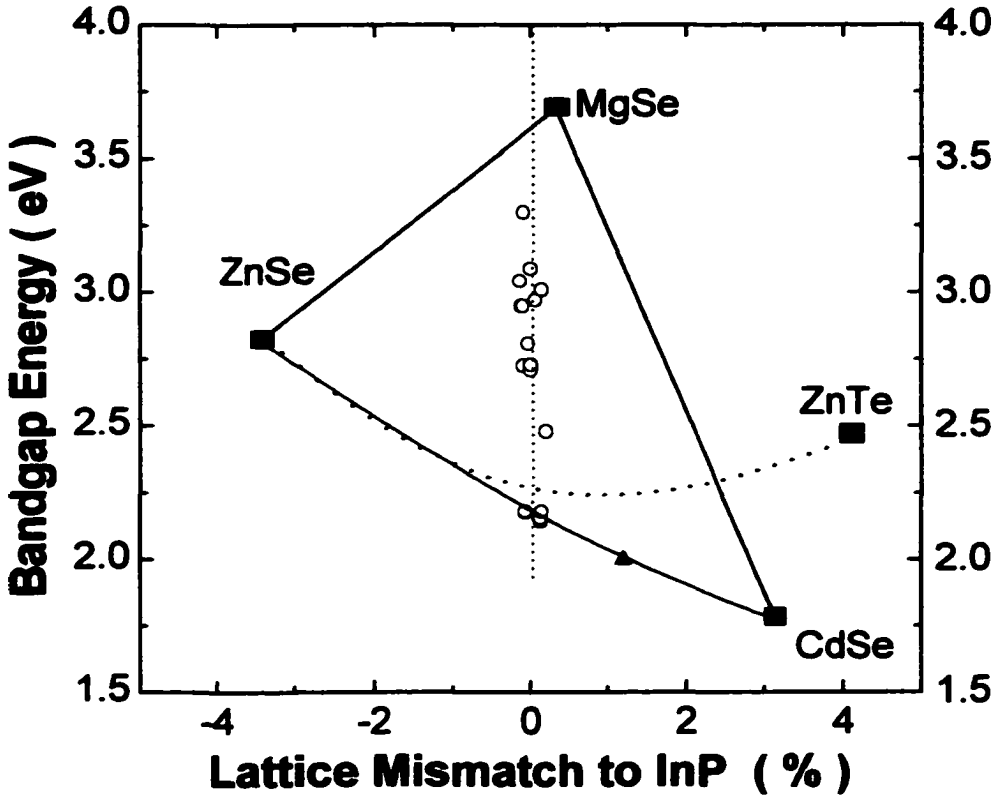

Fig. 1-1 Band gap energy versus lattice mismatch to InP substrate for $Zn_xCd_yMg_{1-x-y}Se$ material family.

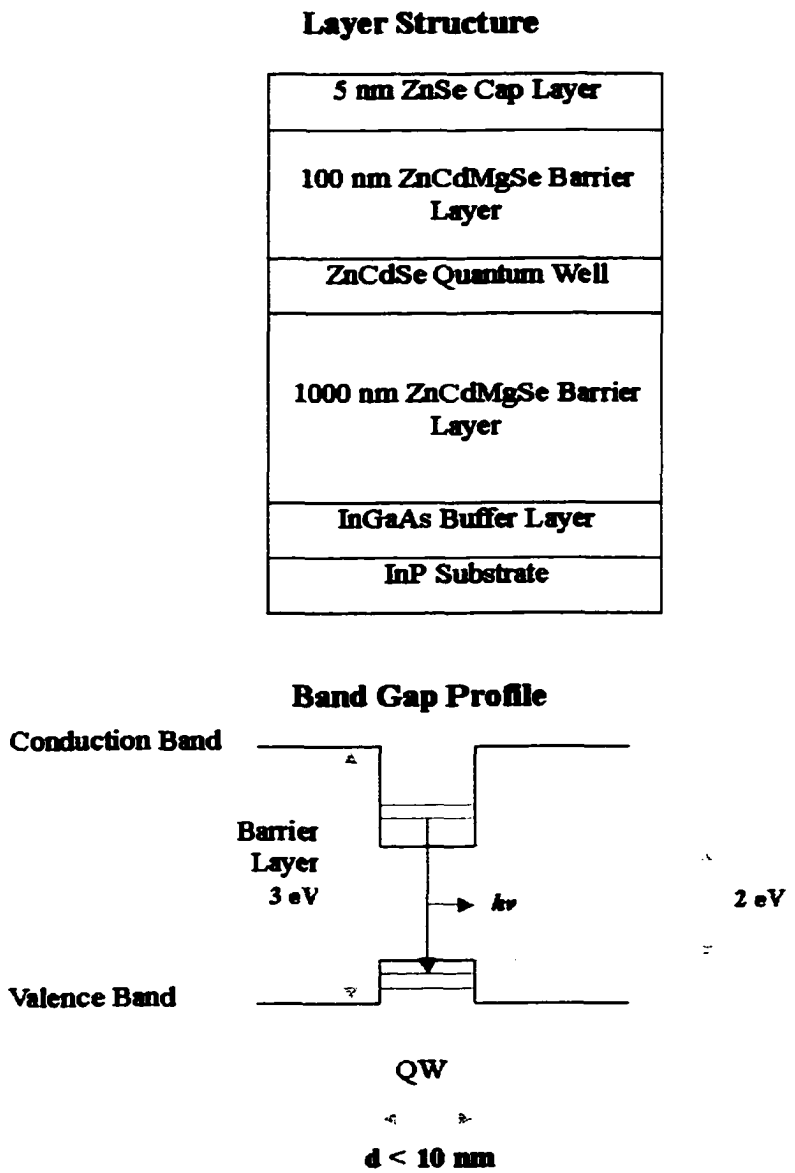

Fig. 1-2: Schematic of quantum well structure and its band gap profile

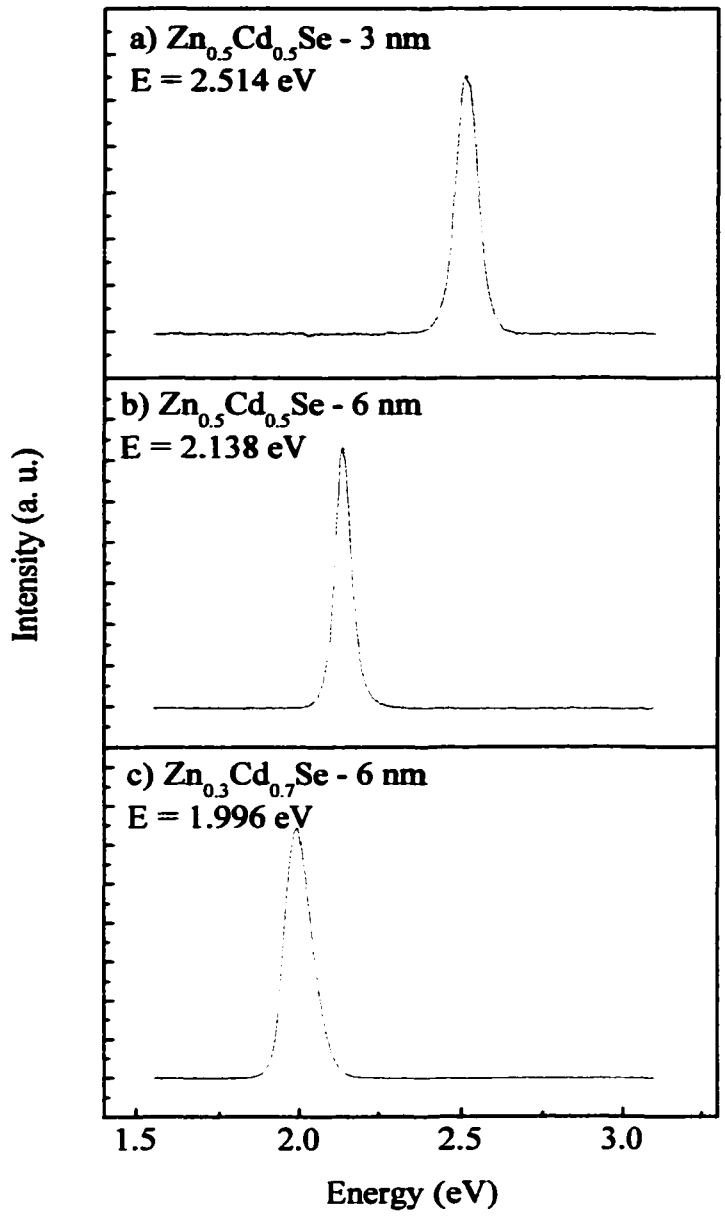

Fig. 1-3: Emission from $Zn_xCd_{1-x}Se/Zn_xCd_yMg_{1-x-y}Se$ QW structures that differ in the QW thickness and/or composition.

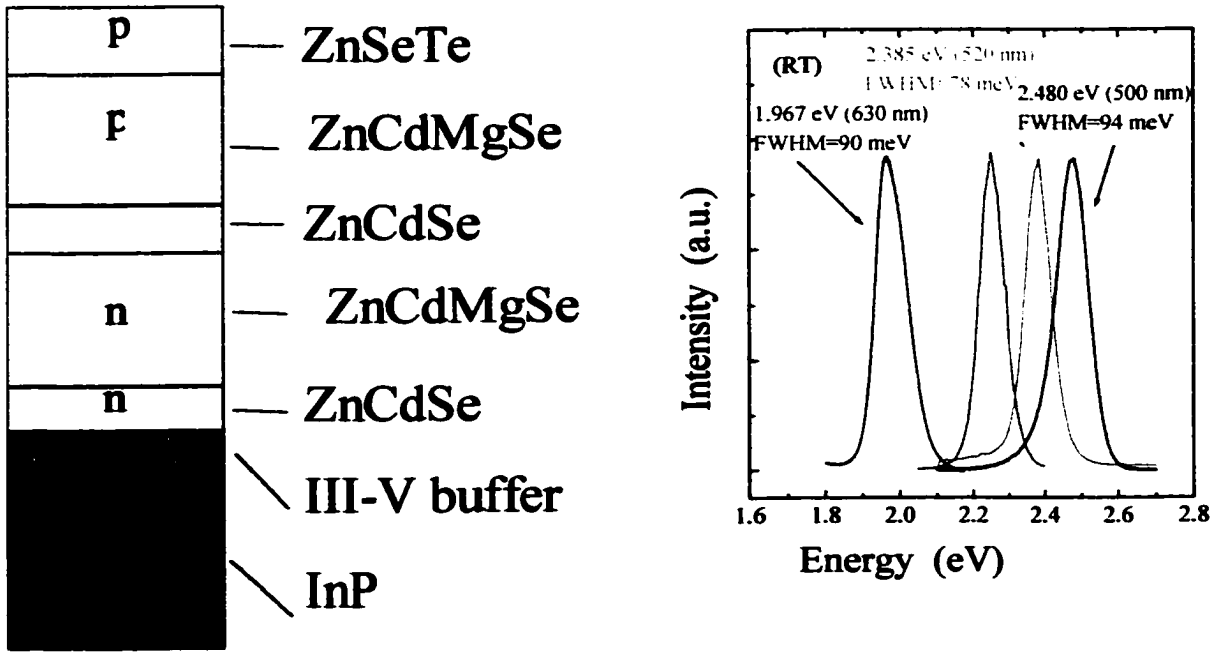

Fig. 1-4: Schematic of LED structures and their room temperature electroluminescence spectra.

Chapter 2

Background and experimental techniques

2-1. Molecular Beam Epitaxy System

Molecular beam epitaxy (MBE) is a versatile technique for epitaxial growth of semiconductor thin films.[1] In MBE, a substrate is held in a vacuum chamber and the atoms that comprise the semiconductor are evaporated onto the surface. A thin, single-crystal layer of material is grown on the surface of a single-crystal substrate. The growth rate of 1 μm/h (approximately one monolayer per second) is slow enough for surface migration to occur. Consequently, a layer-by-layer growth that results in a smooth surface and high single-crystalline quality is achieved.

The arrival rate of various atoms can be calculated from the flux measurements. Atomic flux depends on cell temperature and can be changed by small temperature adjustments. Therefore, doping can be precisely controlled and ternary ($Zn_xCd_{1-x}Se$) and quaternary ($Zn_xCd_yMg_{1-x-y}Se$) layers of known composition can be grown. Many layers of various types of epitaxial composition can be sequentially grown on a substrate in this manner resulting in complex multi-layer structures, such as distributed Bragg reflectors.

A simplified conceptual schematic of the MBE growth chamber is shown in the Figure 2-1. It is an ultra high vacuum (UHV) evaporation system that is pumped by a combination of ion pump, cryo pump, and titanium sublimation pump. Pressures as low as 10^{-8} Torr are reached on a routine basis and 10^{-10} Torr is reached with special care and maintained during the growth. The molecular (or atomic) beams are thermally generated in the source ovens that are resistively heated effusion cells. Individual thermocouples are embedded in the ovens. Shutters are provided for each source, and the entire assembly is surrounded by a liquid nitrogen shroud. The substrate holder is located along the central line of the system. After evaporation, the molecular beams condense and order on the substrate surface under kinetically controlled conditions. During the deposition the substrate is heated and kept at the temperature necessary to allow sufficient surface mobility of the atoms for the epitaxial growth and rotated to provide sample uniformity. A reflection high energy electron diffraction (RHEED) instrument is installed in the growth chamber and is used to monitor the growth. It is described in detail later.

The research described in this dissertation was performed using a Riber 2300P MBE system. A schematic of the system is shown in the Figure 2-2. The system consists of a loading chamber, two growth chambers, a

metallization chamber, and a substrate treatment chamber all connected by UHV channel. One of the growth chambers is dedicated to the growth of III-V materials and the other is dedicated to the growth of II-VI materials. The chambers are isolated by several gate valves to avoid cross-contamination. The growth chambers and transfer channel are pumped by ion pumps and titanium sublimation pumps. A cryo pump is also installed in the II-VI growth chamber and is used during the nitrogen doping. The loading chamber is pumped by a turbo molecular pump. The metallization chamber and substrate treatment chamber were not used in this research and are not described.

The detailed schematic of the growth chambers is shown in the Figure 2-3. The growth chambers are equipped with a manipulator (flux gauge, rotating substrate holder, thermocouple), RHEED (electron gun and phosphorous screen), quadruple mass spectrometer, eight effusion cell ports, and two viewing ports. The effusion cell ports in the III-V growth chamber are equipped with Al, Ga, In crucibles as the group III sources, As crucible as the group V source, and Be and Si crucibles as the p-type and n-type dopant sources, respectively. A pyrometer that can be used to monitor the substrate surface temperature is installed in one of the cell ports and another cell port is empty. The effusion cell ports in the II-VI growth chamber are

equipped with Be, Cd, Mg, Zn crucibles as the group II sources, Se and Te crucibles as group VI sources, and $ZnCl_2$ crucible as the n-type dopant source. A radio frequency (RF) nitrogen plasma source, used for p doping, is installed in one of the cell ports. Gate valves separate growth chambers from the transfer channel.

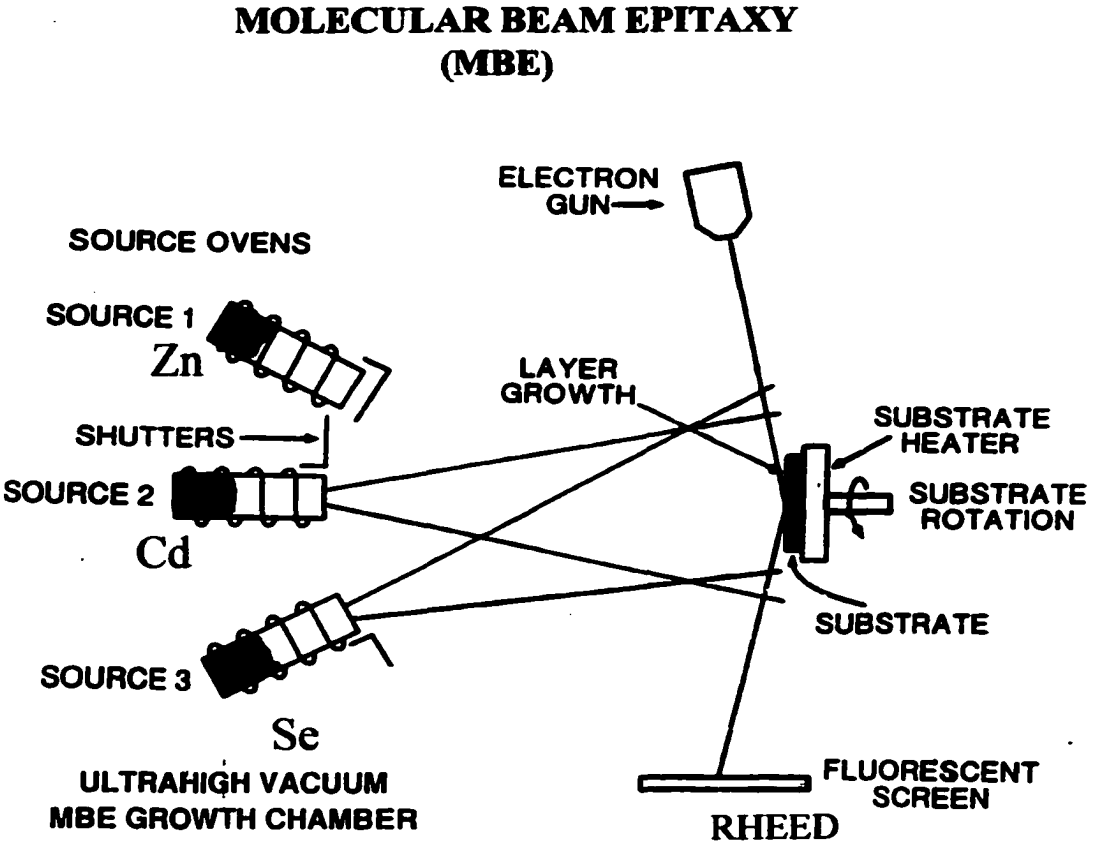

Figure 2-1

Conceptual schematics of MBE growth chamber

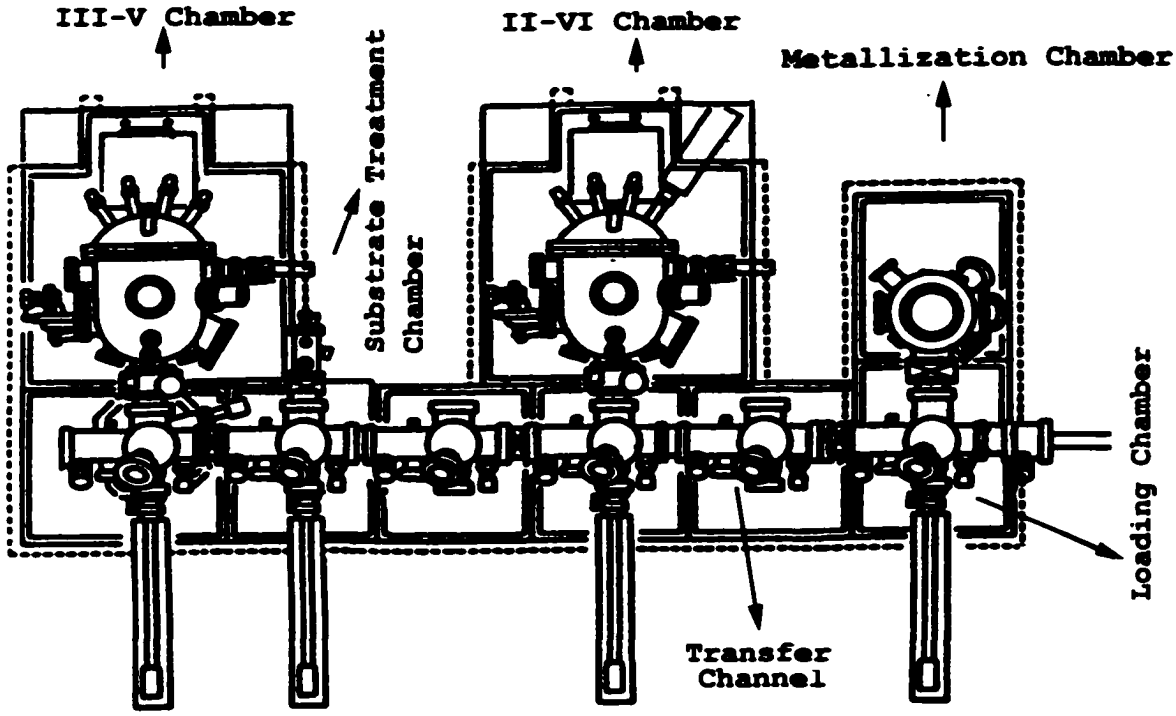

Figure 2-2

Riber 2300 MBE system

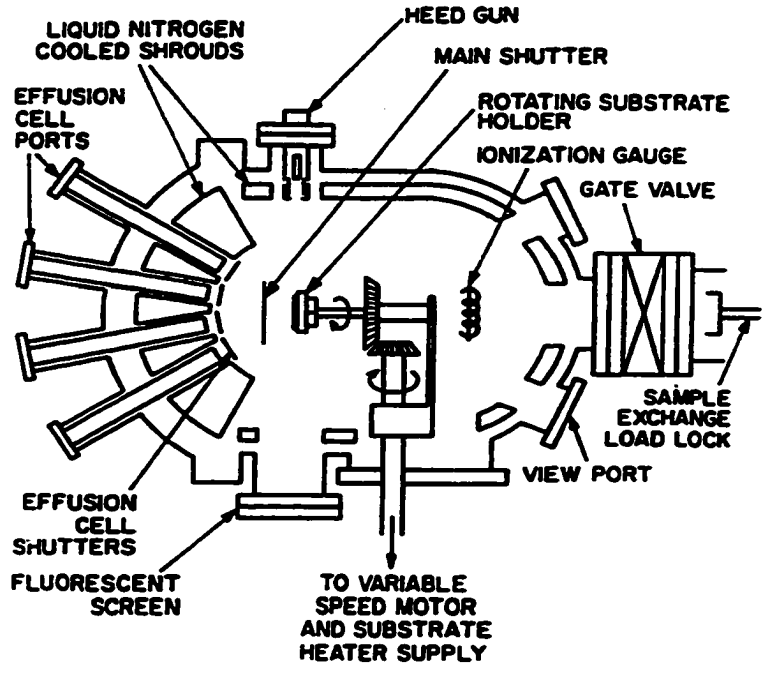

Figure 2-3

Riber 2300 MBE growth chamber

2-2 Reflection High Energy Electron Diffraction

Reflection high-energy electron diffraction (RHEED) is a powerful technique used to monitor epilayer surface *in situ.*[2] The schematic of the RHEED set up is shown on the Figure 2-4. In this technique, electrons with energies 20 – 100 keV are generated by an electron gun and are incident on the sample surface at a very small (glancing) angle. They are diffracted by the surface layers and are detected by the fluorescence they cause on the phosphor screen. The glancing incidence insures that the electrons penetrate only through a very thin layer of the surface. Therefore, RHEED is very sensitive to the processes that occur at the surface and is an ideal method to monitor the surface *in situ.*

The RHEED pattern depends on the atomic arrangement, flatness, and the direction of the surface. A typical RHEED pattern for a disordered surface, such as a substrate surface covered with an oxide layer, is a diffuse or ring pattern. Sharp RHEED lines indicate that the surface is flat and well ordered.[3] The typical RHEED patterns for GaAs and InGaAs are (2x4) for As rich (100) surface and (4x2) for Ga rich (100) surface.[4] The typical RHEED patterns for ZnSe are (2x1) for Se rich (100) surface and C(2x2) for Zn rich (100) surface.[5] These structures represent defect-free, stoichiometric surfaces and the reconstructions occur to accommodate distortions produced

by a redistribution of electrons within the surface bands so that the 'dangling bond band' becomes completely filled. Diffuse, 'spotty', or 'arrow-shaped' pattern indicates a poorly ordered or rough three-dimensional surface and serves as a signal that growth conditions are not optimized. Therefore, the RHEED pattern indicates if the growth is two-dimensional and which elements terminate the surface.

Since the MBE growth occurs in a layer-by-layer mode, RHEED is also used to measure the growth rate.[6] The intensity of one of the RHEED diffraction lines can be monitored via an optical fiber connected to the photomultiplier (PMT) detector (Figure 2.4) as a function of time. The RHEED intensity will be highest when the layer is finished and the lowest when the layer is half-filled (Figure 2.5). Therefore, one RHEED oscillation will indicate that one monolayer has been grown. Since nucleation is not restricted to a single layer but can reoccur before the preceding layer is complete, the subsequent roughening as the next layer develops will cause the oscillation to be damped as the surface becomes statistically distributed over several incomplete atomic layers. Therefore, only a limited number of oscillations is observed. However, if the surface is smooth and the growth conditions are good, a dozen of oscillations can be recorded, giving a good estimate of the growth rate.

In the Figure 2.5, 12 oscillations occur during the first 20 seconds. This corresponds to the growth of 12 monolayers per 20 seconds or 36 monolayers per minute. The GaAs lattice constant is 5.653 Å and one monolayer is equal to a half of it. Therefore the growth rate is 1.7 Å/second or 10 nm/minute.

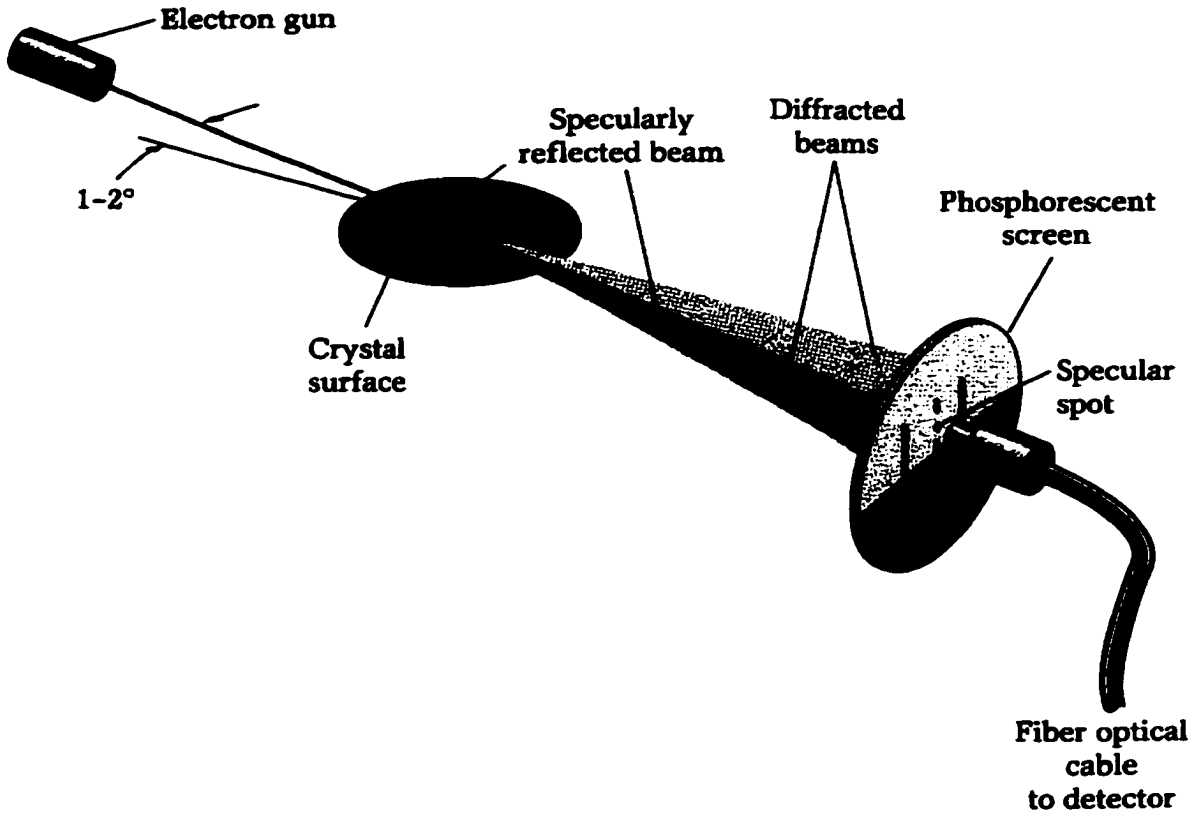

Fig. 2-4. Schematic of the RHEED and RHEED oscillations measurement.

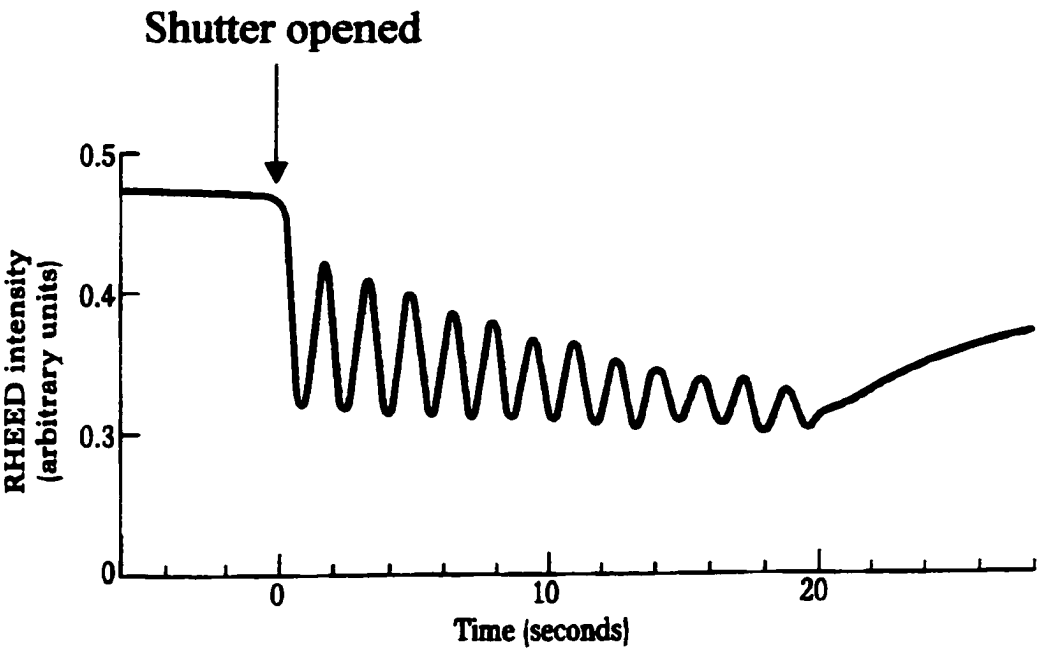

Fig. 2-5. Diagram of RHEED intensity oscillations vs. time.

2-3 X-ray diffraction

X-ray diffraction (XRD) is an important tool for the nondestructive investigation of epitaxial layers, heterostructures, and superlattices.[7] It provides important information that can be used to determine the composition of epilayers, their thickness, and strain. Also, crystalline quality can be evaluated.

The principle of the XRD is based on Bragg's law:

$2d_{hkl} = \lambda/\sin\theta$

$d_{hkl} = a/(h^2 + k^2 + l^2)^{1/2}$

where d_{hkl} is the spacing of lattice planes with Miller indices (hkl) and θ is the corresponding Bragg angle. In Fig. 2-6 the scattering geometry is shown. φ denotes the angle between the lattice plane (hkl) and the surface, k_I is the incident and k_s is the scattered wave vector. The Bragg diffraction is called symmetric if the $\varphi = 0$, i. e the reflecting lattice planes are parallel to the surface. For $\varphi \neq 0$ the Bragg reflection is defined 'asymmetric'.

The (400) symmetric reflection is the one most usually used, since it gives the strongest reflection. Since the InP lattice constant is 0.5867 nm and the excitation wavelength is 0.15406 nm, it is easy to calculate the Bragg angle (θ) for (400) reflection:

$d_{400} = 0.5867/4 = 0.1467$

$2*0.1467 = 0.15406/\sin\theta$

$\sin\theta = 0.15406/0.2934$

$\sin\theta = 0.525$

$\theta = 31.66^{0}$

The schematic of an X-ray diffraction set up used is shown in the Figure 2-7. It consists of an X-ray source, a single crystal X-ray diffraction system (SCXRD), manufactured by RIGAKU, and a double crystal X-ray diffraction system (DCXRD), manufactured by Blake Industries Inc. The description of the two systems is given in detail below.

In SCXRD, only one crystal (the sample) is used. The $\theta - 2\theta$ coupled mode is usually used in SCXRD measurements. For such a scan, the detector is rotated twice as fast and in the same direction around the diffractometer axis as the sample. During this motion the angle ω between the incident beam and the sample surface changes. The incident X-ray is not monochromatic and the two excitation lines (Cu $K_{\alpha 1}$ and Cu $K_{\alpha 2}$) are present. The wavelength spread ($\Delta\lambda$) is also large. Therefore, two broad peaks are observed from each epilayer in the XRD spectrum. SCXRD can be used only to measure the lattice constant and estimate composition for the simple cases, when you have one strongly mismatched epilayer on the substrate. If

more than one epilayer are present and the mismatch is small, the peaks overlap and it is impossible to resolve them. In this case, DCXRD is used.

The simplified schematic of a Double-Crystal Spectrophotometer is also shown in the Figure 2.7 A first crystal (dislocation-free (100) Ge) is used to cut the Cu $K_{\alpha 2}$ line and to minimize the wavelength spread ($\Delta\lambda$). The second crystal is the sample to be investigated. In DCXRD, the detector is fixed in position with wide-open entrance slits and the sample is rotated, i. e. ω is changed. Therefore, the X-ray reflection of a single crystalline bulk sample as a function of the angle ω is measured and the 'rocking curve' is obtained.

Because of its increased resolution, this method is good to measure small lattice-mismatch and to evaluate the layer quality. The full width of half maximum (FWHM) of the diffraction peaks give us information about the material quality. The high resolution facilitates the observation of satellite peaks, which are usually observed for high crystalline quality periodic structures and can be used to estimate thickness of the epilayers.

For example, the XRD rocking curve from an InGaAs epilayer grown on InP substrate is shown in Figure 2-8. Two peaks are evident in the spectrum: the dominant peak is from the InP substrate and the second is

from the epilayer. From the separation between the peaks (Δ) InGaAs lattice constant is calculated using Bragg equation:

$$a_{InGaAs} = 2*1.5406/\sin(31.66 + \Delta)$$

For this case $\Delta = 185$ arc sec $= 0.05^{0}$, and $a_{InGaAs} = 5.860$ Å.

Lattice mismatch is determined as the difference between the lattice constant of the epilayer and the substrate:

$$\Delta a/a = (a_{InGaAs} - a_{InP})/a_{InP} * 100\% = (5.860 - 5.867)/5.867 * 100\% = -0.14\%$$

Since the lattice constants of InAs (6.058 Å) and GaAs (5.653 Å) are known, we can calculate composition assuming that the lattice constant of the alloy depends linearly on the composition (Vegard's law):

$$6.058*x + 5.653*(1-x) = 5.860$$

$$x = 0.51$$

The composition of the epilayer is $In_{0.51}Ga_{0.49}As$.

The schematic of a ZnCdSe/ZnCdMgSe superlattice with 12 periods grown on InP substrate is shown in Figure 2.9. It consists of 12 alternating periods of ZnCdSe (73 nm) and ZnCdMgSe (49 nm) deposited on the InP substrate. The XRD rocking curve for this structure is shown in Figure 2-10. The solid line represents the experimental spectrum. The most intense narrow peak in the center represents the (004) reflection from the InP substrate and the zero order peak from the superlattice is seen as a shoulder

on the InP peak. More than six satellite peaks on each side of the zero order peak are visible in the DCXRD rocking curve, indicative of a high quality periodic structure. The observed satellite peak positions are plotted in the form of sinθ in Figure 2-11. The linear relation to the order of the peaks gives evidence that the observed peaks are diffraction peaks from the superlattice structure. From the slope, the thickness of the period (L) is estimated using the equation:[8]

$$\lambda/2L = 6.345 \times 10^{-4}$$

$$L = \lambda/(12.69 \times 10^{-4})$$

since $\lambda = 1.541$ Å, $L = 1214$ Å

The dotted line in Figure 2-10 represents a theoretical simulation based on the period calculated above. The position and the intensity of the satellite peaks are in a good agreement with the experimental data, indicating a correct estimate of the thickness of a period.

The strain of the epitaxial layers is another important parameter that can be deduced from DCXRD measurements. In a system consisting of an epilayer ***a*** and a substrate with a different lattice constant, the epilayer, as it grows, will adopt to the lattice constant of the substrate by distorting its lattice cell. Such a distortion produces lattice strain. As the layer thickness increases, the strain builds up until it is large enough to produce misfit

dislocations that allow the layer to relax. Therefore, depending on the thickness and the elastic constant of the layer, it can be fully strained, partially strained, or fully relaxed. When the thickness of the epilayer is less than a certain thickness (critical thickness), the epilayer will be pseudomorphic (fully strained), and its tetragonal structure will be distorted as shown in Fig. 2.12. The parallel lattice-mismatch is in the plane between the epilayer and the substrate and is equal to zero. The perpendicular lattice mismatch is in the growth direction and in a cubic lattice is approximately two times larger than the bulk lattice-mismatch between the epilayer and the substrate. When the thickness of the epilayer exceeds the critical thickness, the epilayer first becomes partially relaxed and then fully relaxed. If the layer is partially relaxed, the parallel mismatch is not equal to zero any more, but is still smaller than the perpendicular mismatch. In the case of a fully relaxed layer, the parallel and the perpendicular lattice mismatch are equal to each other. The (400) reflection shows the perpendicular lattice constant and if the layer is not fully relaxed the mismatch will be over estimated. In order to obtain more careful data on the epilayer lattice constant and composition it is necessary to perform (511) asymmetric measurements. The typical (400), $(511)_a$, and $(511)_b$ rocking curves for 1.4 μm $Be_{0.03}Zn_{0.97}Se$ epilayer on the GaAs substrate are shown in the Fig. 2.13.

The subscripts a and b represent (511) reflection geometries with x-ray incident angle of $\theta+\varphi$ and $\theta-\varphi$, respectively (θ is Bragg angle, $\varphi = 15.793$). The peak separation from $(511)_a$ is very close to the peak separation from (400). The peak separation from $(511)_b$ is almost double the peak separation from $(511)_a$. By measuring peak separations $\Delta\theta_a$ and $\Delta\theta_b$, as the difference between the substrate and the epilayer peak, the parallel and perpendicular mismatch can be determined:

$$\Delta(a/a_s)_\perp = (a_\perp - a_s)/a_s = \sin\theta*\cos\varphi/[(\sin(\theta+(\Delta\theta_a+\Delta\theta_b)/2)*\cos(\varphi+(\Delta\theta_b - \Delta\theta_a)/2) - 1];$$

$$\Delta(a/a_s)_{||} = (a_{||} - a_s)/a_s = \sin\theta*\sin\varphi/[(\sin(\theta+(\Delta\theta_a+\Delta\theta_b)/2)*\sin(\varphi+(\Delta\theta_b - \Delta\theta_a)/2) - 1];$$

The perpendicular and parallel strains are related by the Poisson effect and the bulk lattice mismatch can be calculated using:

$$a_0 = a_\perp\{1-[2\nu/(1+\nu)][(a_\perp - a_{||})/ a_\perp]\}$$

where ν is the ratio of the perpendicular and parallel strain:

$$\nu = - \varepsilon_\perp/\varepsilon_{||}$$

defined as Poisson ratio. The Poisson ratio for semiconductor films falls between 0.25 and 0.35.

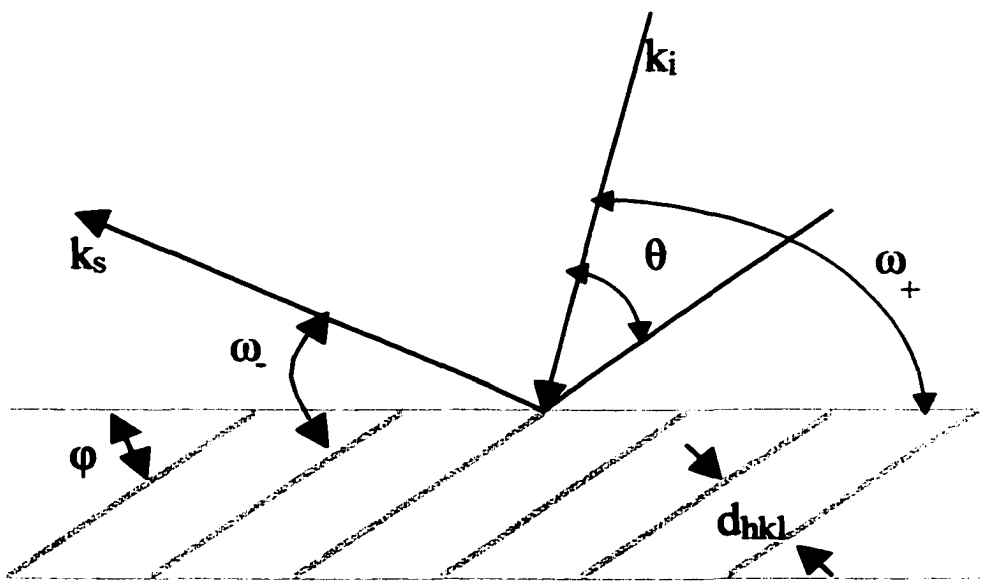

Fig. 2-6: X-ray scattering geometry.

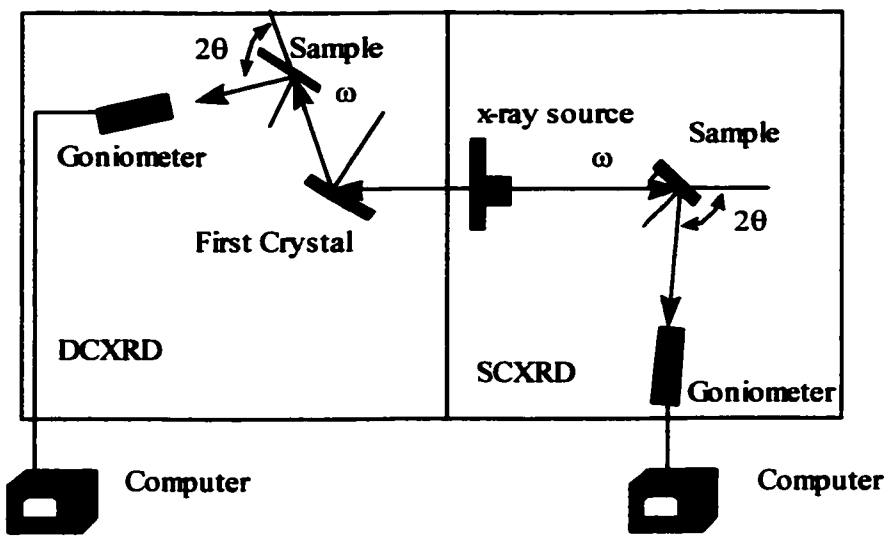

Figure 2-7. X-ray diffraction system

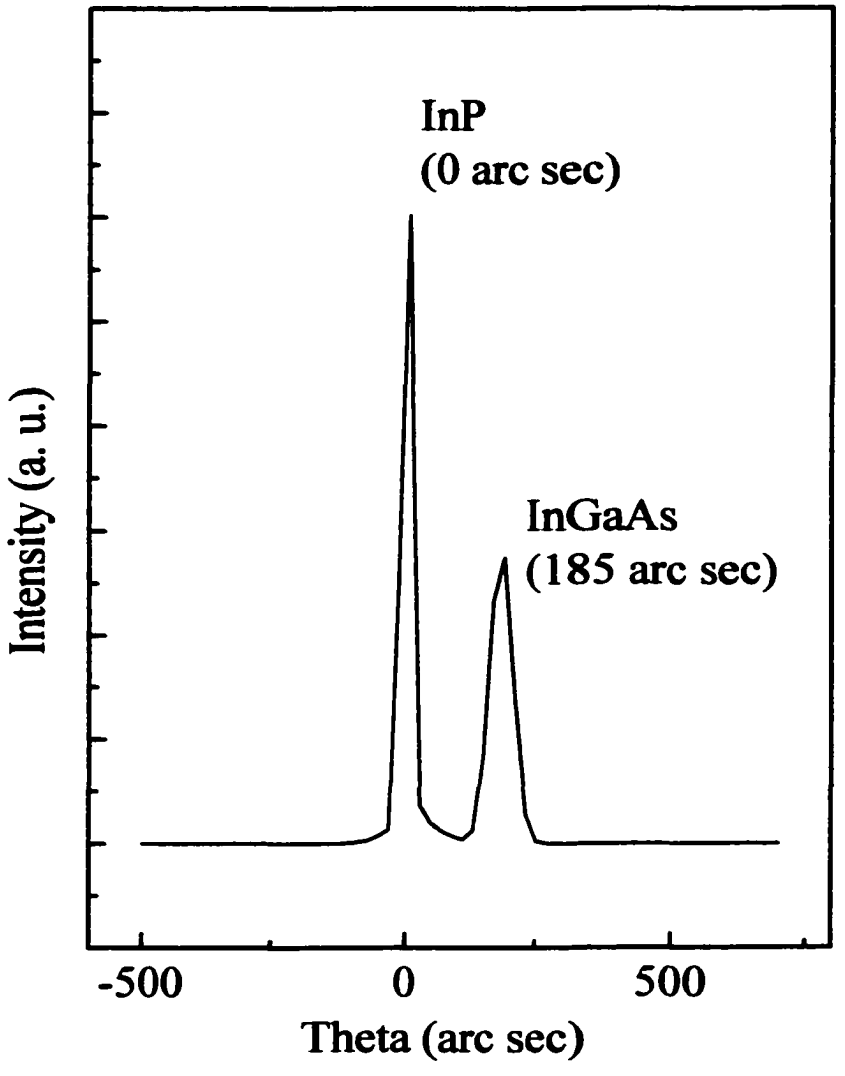

Fig. 2-8: Double crystal x-ray rocking curve from an InGaAs layer grown on an InP substrate.

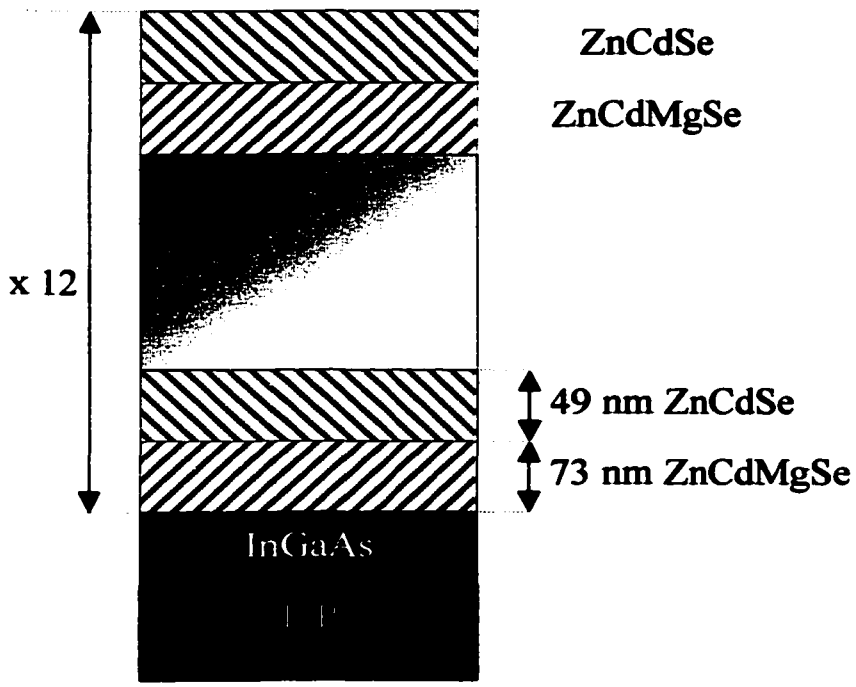

Fig. 2-9: Schematic of a ZnCdSe/ZnCdMgSe DBR with 12 periods grown on an InP substrate.

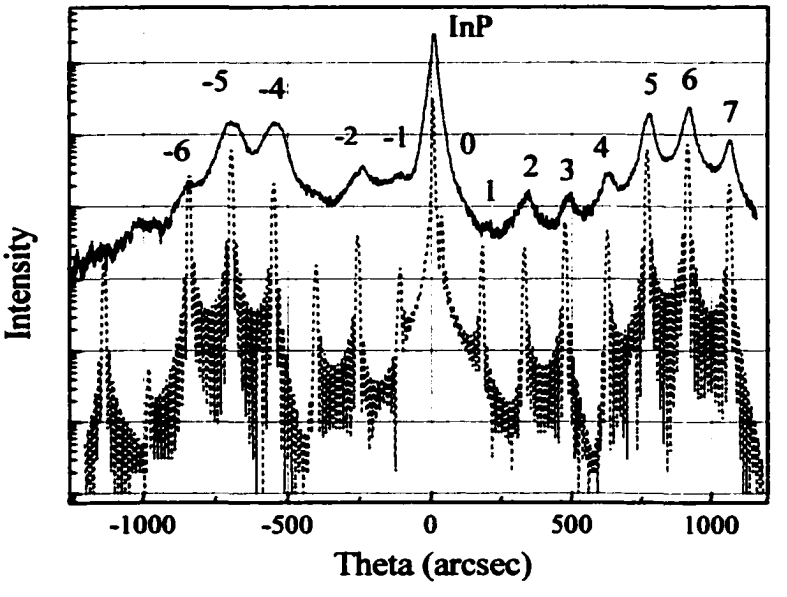

Fig. 2-10: Double crystal x-ray rocking curve obtained from a ZnCdSe/ZnCdMgSe superlattice with 12 periods grown on an InP substrate.

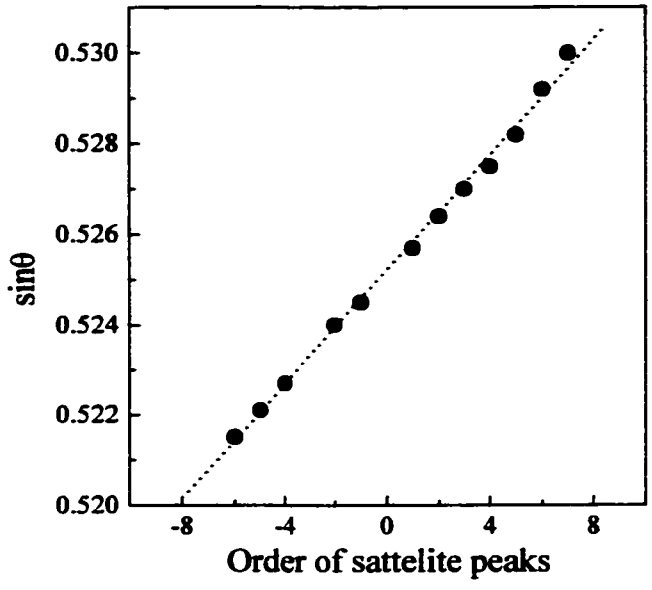

Fig. 2-11: Position (sinθ) of satellite peaks plotted versus satellite peak order for a ZnCdSe/ ZnCdMgSe superlattice with 12 periods.

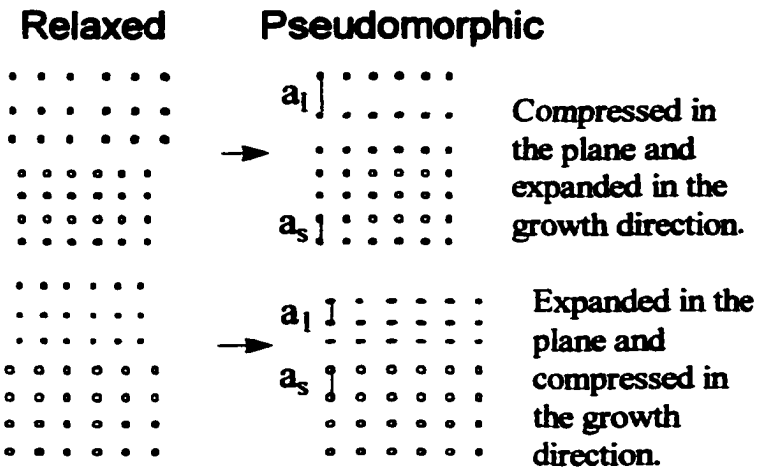

Fig. 2-12: The schematic of the crystalline lattice under compressive and tensile strain.

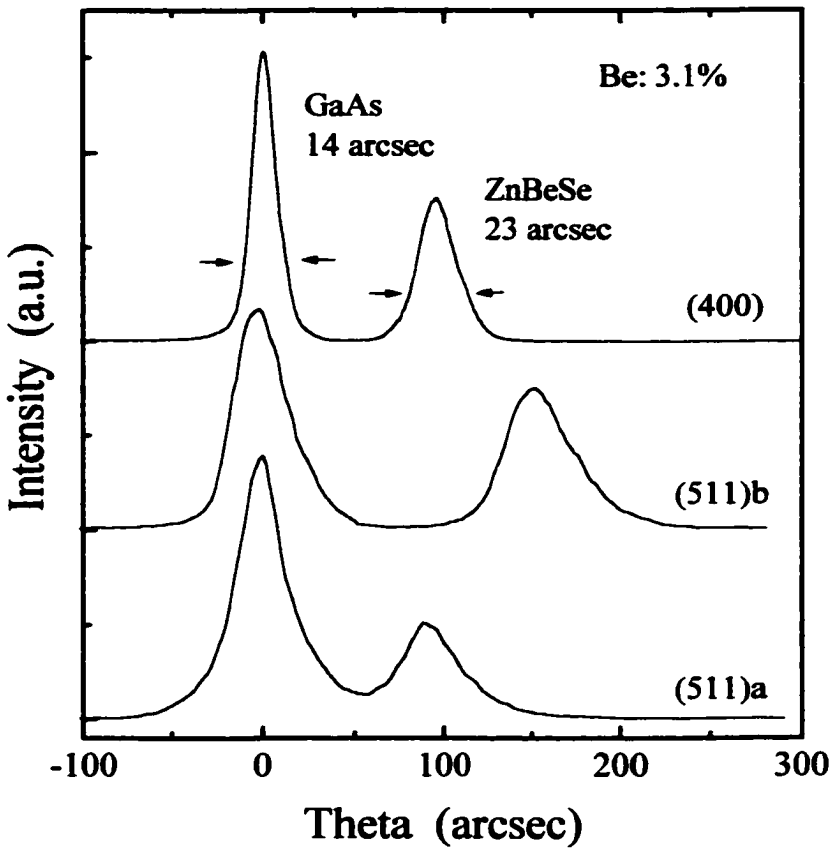

Fig. 2-13: The DCXRD rocking curves for $Be_{0.03}Zn_{0.97}Se$ epilayer on GaAs substrate.

2-4 Photoluminescence

Photoluminescence (PL) plays an important role for the characterization of epitaxial layers. In a PL experiment, electrons are excited by absorption of light from valence to conduction band. In direct band gap materials such as ZnSe, the excitation occurs through direct transition (the electron does not change its wave vector). In indirect band gap materials such as BeTe, the electron changes its wave vector during the excitation. After excitation the electrons reach the conduction band minimum and recombine with the holes in the valence band. Photo excited carriers can recombine through different mechanisms.

A free or bound exciton recombination is the most usual pathway. An exciton is a two-particle system that consists of electron in the conduction band and hole in the valence band bound by Coulomb attraction. Due to Coulomb attraction, the energy necessary to create an electron-hole pair is slightly smaller than the energy gap. If an exciton is localized on a donor or acceptor it is called bound exciton (BE). Otherwise, it is called free exciton (FE).

Donor-to-acceptor (DA) and free-to-bound (FB) recombination can occur in the doped semiconductors. When a doped semiconductor is irradiated with photons with energy greater than the band gap energy, the

photoexcited e-h pairs neutralize the donors and acceptors present in the sample:

$$e^- + D^+ \rightarrow D^0 \qquad h^+ + A^- \rightarrow A^0$$

After a certain time carriers in the neutralized donors and acceptors recombine through either transition of an electron bound to a donor with a hole bound to a neighboring acceptor (DA):

$$D^0 + A^0 \rightarrow D^+ + A^- + h\nu$$

or transition of a free electron (hole) with a hole (electron) bound to an acceptor (donor) (FB) recombination:

$$h^+ + D^0 \rightarrow D^+ + h\nu \qquad e^- + A^0 \rightarrow A^- + h\nu$$

These transitions have energies that are slightly smaller than band gap.

Also, band-to-band transitions can occur in very high quality materials. The simplified band energy diagram with the radiative transitions is shown in figure 2-14.

These pathways can be identified using temperature and intensity dependent measurements. The information that can be obtained using these measurements includes band structure and band gap energy of the semiconductor, identification of impurities and defects present, effective masses for the carriers, phonon properties, and epilayer quality.[9]

The schematic of the PL system is shown in figure 2-15. The samples are mounted on the cold finger of a Janis cryogenic system. Prior to cooling, the system is pumped to ~ 10^{-5} Torr. The cold finger can be cooled down to 5.8 K using liquid helium and 78 K using liquid nitrogen. The temperature of the cold finger can be controlled between 5.8 K to 300 K using a heater installed on the back of the cold finger. A He-Cd laser with the emission wavelength of 325 nm is used as the excitation source. The excitation laser intensity can be changed using a set of zero density filters with transmission varying from 50% to 3%. The laser beam passes through a chopper, which changes the laser beam to a periodic signal (ac), then is focused to a small spot on a sample. The luminescence from the sample is collected by a lens and converted to a collimated beam. The collimated beam is focused to a spot on the first slit of the spectrometer. The beams that pass through the SPEX 1680-B spectrometer are detected by a photo multiplier and are converted to an electrical signal. The ac signal is then fed to a lock-in amplifier to be amplified. Finally, the amplified signal is inputted into the data scan connected to the computer to be collected and analyzed.

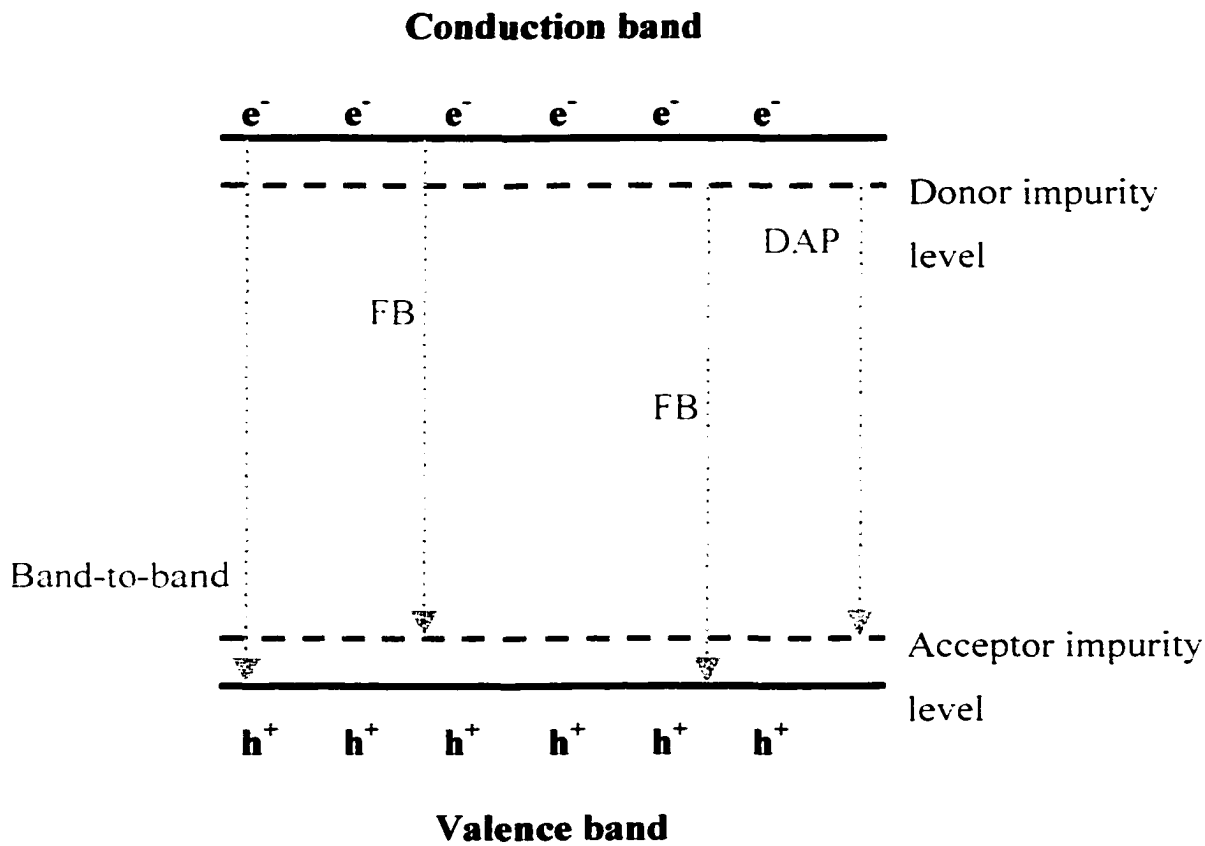

Fig 2.14: Band energy diagram and radiative transitions

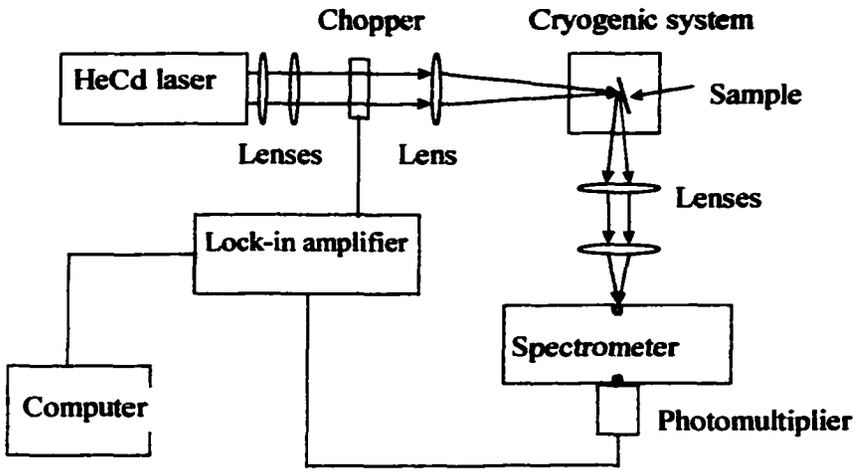

Figure 2-15. Illustration of photoluminescence setup

2-5 Reflectometry

Reflectometry is another non-destructive technique that is used to study energy levels, indices of refraction and thickness of thin films.[10] As a band gap determination technique it has a number of advantages in comparison to the PL. First of all, it is not so sensitive to the material quality. Also, since band gap energy determination is not based on the emission it can be used to measure direct band gap energy for the indirect semiconductors. It also measures band gap energy at room temperature, at which the PL emission is usually very weak.

Reflectometry can be applied both for the epilayers deposited on the substrates and film free materials. In this work we were studying thin films (1 – 2 μm) grown on the top of thick substrates. The band gap of the substrate was smaller than the band gap of the epilayer, while the index of refraction of the substrate was larger than the index of refraction of the epilayer.

An example of a reflectivity spectrum (R) is shown in Figure 2-16. This spectrum corresponds to a ZnTe layer grown on an InP substrate. The complex refractive indices of this system can be described as: $1 + i0$ (air), $n + ik$ (ZnTe), and $n_0 + i0$ (InP), where $n < n_0$. [The sample and the various regions are shown in Figure 2-17.] R is generated by the interference of the

beams reflected at the two interfaces (air/epilayer and epilayer/substrate). Under the normal incidence condition, the reflectance is expressed by

$R = (ax + b/x - 2abcos2\delta)/(ex + a^2b^2x - 2abcos2\delta)$ where

$x = e^{\alpha d}$,

$a = ((n-1)^2 + k^2)/ ((n-1)^2 + k^2)^{1/2}$,

$b = ((n-n_0)^2 + k^2)/ ((n+ n_0)^2 + k^2)^{1/2}$

$\alpha = 4\pi k/\lambda$ is absorption coefficient, d is the epilayer thickness, and $\delta = 2\pi nd/\lambda$.

The R spectrum can be separated into three regions. The lowest energy region (A) is a transparent region in which the epilayer does not absorb light ($hv < E_g$). In this region k vanished and $\alpha d = 0$. The reflectance shows an oscillation as a function of *hv*, having minimum and maximum values of

$R_{min} = ((n_0-1)/(n_0+1))^2$

$R_{max} = ((n^2-n_{0)/(}n^2+n_0)^2$

Where n and n_0 are the indices of refraction of the epilayer and the substrate, respectively. The maximum and minimum values of reflectivity do not depend on the epilayer thickness. Therefore, if the refractive index of substrate is known, the refractive index of epilayer can be calculated.

The middle region (B) is a transition region ($h\nu \approx E_g$) in which the epilayer starts to absorb light. In this region, $k < n$ and $\alpha d \sim 1$. As a result, the reflectance shows a damped oscillation as a function of $h\nu$. It is difficult to calculate the accurate refractive indices from the reflectance measurements in this region. However, the position of the direct band gap, that is located in this region, can be estimated as the point where oscillations end.

The highest energy region (C) is the absorption region ($h\nu > E_g$). In this region $k > n$ and $\alpha d > 1$. It is difficult to determine indices of refraction in this region. It is possible to identify higher energy critical points, but this identification requires knowledge of the band structure of the substrate, good estimate of the band structure of epilayer, and elaborate calculations. The same results can be more precisely obtained using other techniques, e. g. ellipsometry.

A Cary 500 UV-Visible Spectrophotometer with a Variable Angle Specular Reflectance accessory was used in this research. The optical design of the accessory is shown in the Figure 2.18. The accessory features a dual 'V-W' configuration, with one spherical mirror (S1) and two toroidal mirrors (T1 and T2) per beam. The movable mounting of the spherical mirrors allows them to be used for both calibration and sample

measurement. Hence, the same optical components are in the light path during both calibration and measurement. When a sample is mounted, the only change in the system is due to the reflectivity of the sample. An absolute value of reflectance is thus obtained.

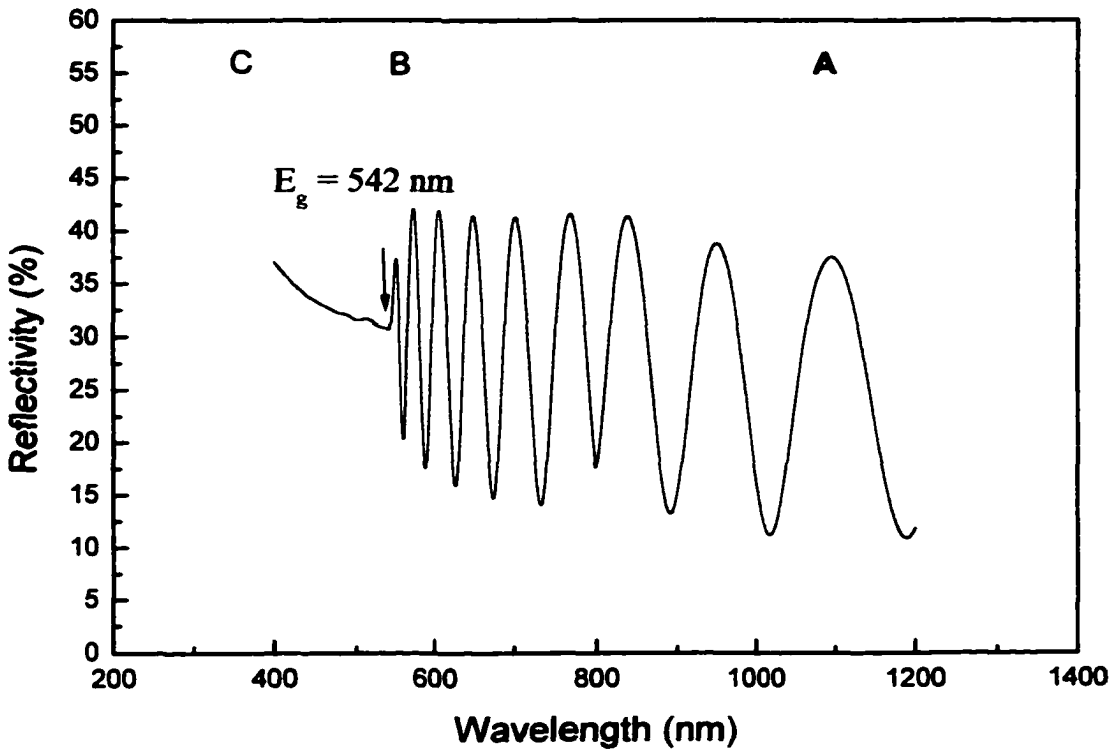

Fig. 2-16: Reflectivity spectrum of a ZnTe epilayer grown on InP substrate.

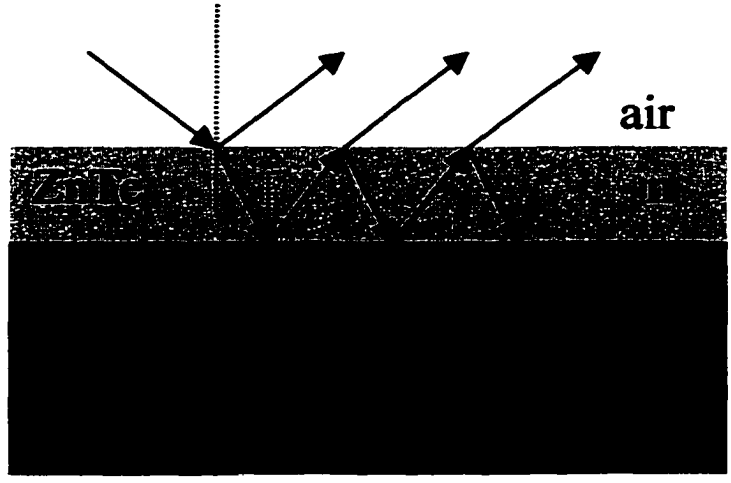

Fig. 2-17: Schematic of a ZnTe epilayer grown on an InP substrate. Reflections and transmissions for two interfaces are shown. The resultant reflected beam is made up of the specular beam and the infinite series of beams which are transmitted from ZnTe back into air.

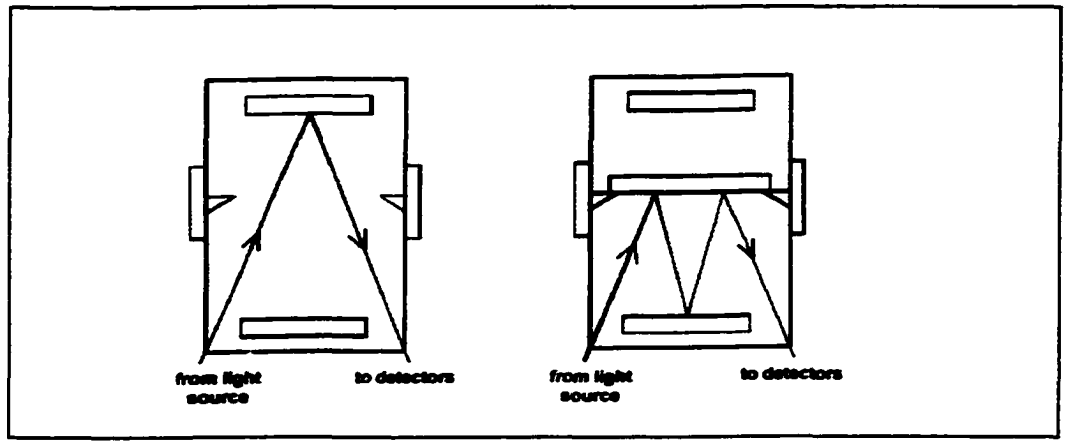

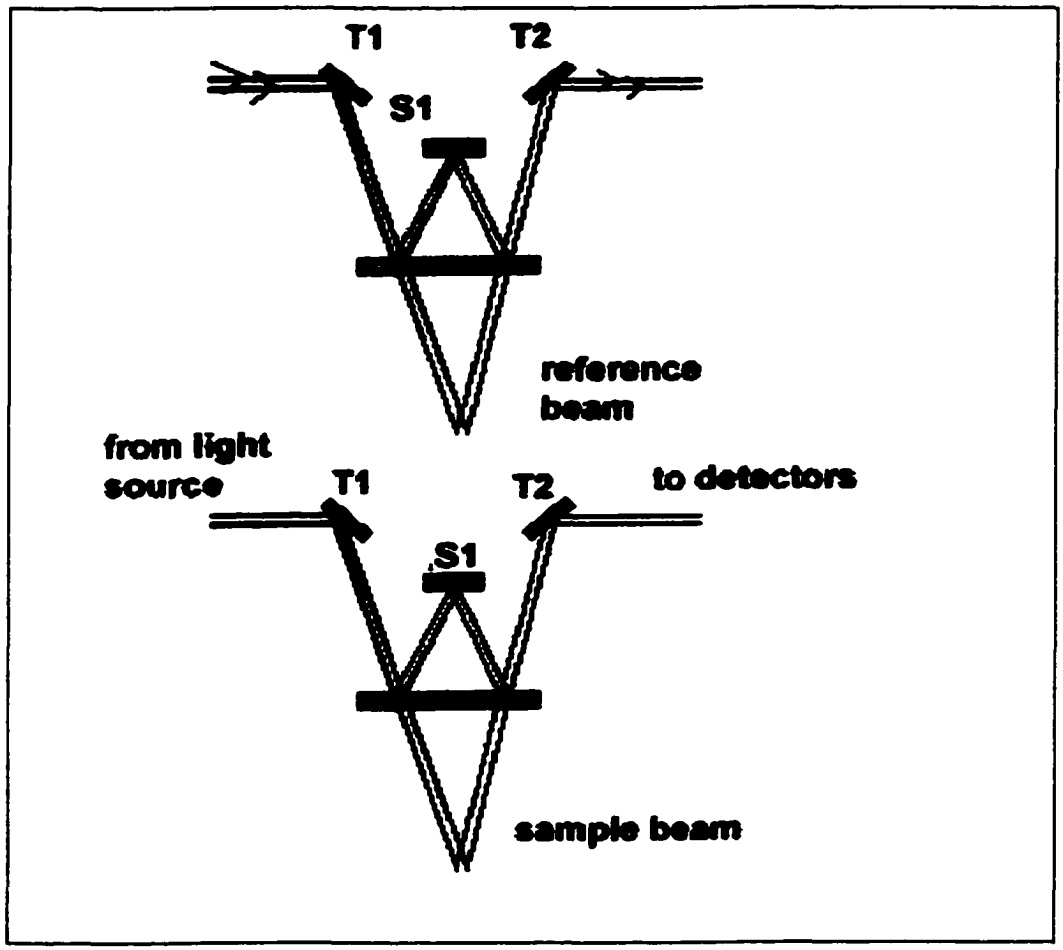

Fig. 2-18: Geometry of the Variable Angle Specular Reflectance accessory

2-6 Molecular beam epitaxy growth procedure

All the samples discussed in this thesis were grown on (100) InP substrates. When available, epi-ready substrates were used. Otherwise, InP substrates were *ex situ* cleaned by degreasing and etching prior to the use. Degreasing was performed by sequential boiling of substrates in thrichloroethylene (TCE), acetone, and methanol solutions. For etching H_2SO_4:H_2O_2:H_2O (4:1:1) solution was used. After etching the substrates were flushed in deionized water and blown dry with ultra pure nitrogen gas. The substrates were bonded with In to the molybdenum blocks and introduced to the MBE system through the loading chamber.

Prior to the growth, the growth chambers were cooled down with liquid nitrogen to achieve better vacuum. Then, effusion cells were heated to the temperatures used during the growth. A computer program was used to perform uniform heating and to avoid rapid material expansion. When the temperature of the effusion cells became stable, flux measurements were performed to estimate arrival rate of the atoms. Flux measurements were performed for each source separately, starting with the source with the smallest flux. For the flux measurements, the shutter on the source measured was opened, while shutters on the other sources were kept closed. At the same time the flux gauge located on the manipulator was positioned to

obtain the maximum reading. If the results of the flux measurements were different from the expected ones, cell temperatures were adjusted.

InP substrates were transferred from the loading chamber to the III-V growth chamber where oxide desorption and buffer layer growth were performed. Oxide desorption was performed by heating the substrate up 500 ^{0}C under the As flux (As passivation).[11] RHEED was used to monitor the surface reconstruction during the heating. When the substrate temperature was below 300 ^{0}C, a half-concentric circular RHEED pattern, indicating the presence of amorphous oxide layer, was visible. As the temperature continued to increase, a diffraction pattern of spots appeared. The spotty RHEED pattern became elongated into lines with the further increase of temperature, indicating that surface became smoother. At around 460 ^{0}C, bright RHEED pattern formed with 2-fold reconstruction lines in the [011] direction and 4-fold lines in the [011] direction corresponding to a (2x4) recombination. The heating was continued until at 480 – 500 ^{0}C the RHEED changed to the 4-fold reconstruction lines in the [011] direction and 2-fold lines in the [011] direction (4x2). The change of surface reconstruction indicated the oxide layer was completely removed. Then, the substrate temperature was decreased until the original (2x4) surface reconstruction was restored and a 150-200 nm-thin lattice-matched $In_{0.5}Ga_{0.5}As$ buffer layer

was grown. The growth was terminated with a (2x4) surface reconstruction, indicating As-terminated surface. After this, the samples were transferred to the II-VI chamber for II-VI material growth.

Prior to the $Zn_xCd_yMg_{1-x-y}Se$ or $Be_xZn_yCd_{1-x-y}Se$ growth, the samples were exposed to a Zn flux (Zn irradiation) for 40 sec to suppress the formation of Ga_2Se_3 complexes on the II-VI/III-V interface.[12] Then, thin (5-10 nm) low temperature (170 °C) $Zn_{0.5}Cd_{0.5}Se$ interfacial layers were grown. The growth was interrupted and under the Se flux the samples were heated to 270 ^{0}C at which the growth was performed. The growth was performed under Se-rich conditions characterized by (2x1) surface reconstruction. This procedure was previously developed to obtain high quality $Zn_xCd_yMg_{1-x-y}Se$ epilayers.[12]

For $Be_xZn_{1-x}Te$ growth, after the transfer from III-V chamber the samples were heated to 270 ^{0}C and were exposed Zn flux 40 sec. No low-temperature buffer layer was grown.. Then, $Be_xZn_{1-x}Te$ growth was performed under Te-rich conditions characterized by (2x1) surface reconstruction. When $Be_xZn_{1-x}Te$ growth was performed without Zn irradiation, the RHEED pattern was spotty during the first few minutes indicating three-dimensional growth, and the samples exhibited lower crystalline quality. A few attempts were made to grow $Be_xZn_{1-x}Te$ using

low-temperature $Zn_{0.5}Cd_{0.5}Se$ or $Be_{0.5}Zn_{0.5}Te$ interfacial layer. However, no improvement in the crystalline quality was observed.

The substrates were rotated during the growth to provide lateral uniformity. Reflection high-energy electron diffraction (RHEED) was used to monitor the growth *in situ*.

Chapter 3

$Zn_xCd_yMg_{1-x-y}Se$ - based distributed Bragg reflectors

3-1 Introduction

For applications that require two-dimensional arrays of light emitters, it is desirable to fabricate surface emitting devices, such as resonant cavity LEDs (RCLED).[1] They have a number of advantages in comparison to conventional LEDs, such as enhanced emission and better spectral purity. RCLEDs are designed by placing the quantum well and barrier layers between two high reflectivity distributed Bragg reflectors (DBRs). Several groups have already fabricated highly reflective DBRs (R > 95 %) operating in various regions of the visible spectrum. For example SiO_2/TiO_2, Si/SiO_2, $ZnSe/CaF_2$, and $ZnSe/MgF_2$ are some of the common materials combinations found in the literature. [2] The growth techniques involved in depositing above systems have been ion sputtering, electron beam evaporation, or thermal evaporation. These DBR systems can be incorporated in resonant cavity structures only externally, after the initial growth and epitaxial lift off (ELO) of the active semiconductor layers. However, there are significant advantages in fabricating the DBRs monolithically with the active layer, in a single epitaxial growth process. In

this case sample processing is minimized and many problems encountered in the ELO method are avoided.

DBRs consist of a sequence of alternating layers of two different materials, each having an optical thickness of $\lambda/4$, where λ is the wavelength within each layer material at which the mirror has the maximum reflectivity. There are three characteristics that should be optimized when designing a DBR: the value of reflectivity, the width of the stop band, and the position of the stop-band. The reflectivity of the DBR depends on the difference between the indices of refraction (Δn) of the two alternating layers and on the number of periods (N) in the stack. Since both of the parameters affect the reflectivity, N can be kept relatively low if Δn is large. The width of the stop-band is large when materials with a large difference in the indices of refraction are used, and is very sensitive to the variations of the individual layer thickness. If one of the layers deviates from the desired thickness $\lambda/4$, then the phase mismatch of the reflected light increases much faster for wavelengths away from the center wavelength, resulting in a narrower bandwidth. The position of the stop-band is adjusted by changing the optical thickness of the two alternating layers.

Several III-V and II-VI materials combinations have been previously explored in order to produce high reflectivity DBRs. Significant success has

been achieved in the development of III-V-based structures (GaAs/AlAs on GaAs substrates,[3] and AlPSb/GaPSb[4] and GaAsSb/AlAsSb[5] on InP substrates), which have shown a maximum reflectivity > 99 % with ≅ 20 periods. The use of II-VI ZnSe-based materials has been less successful due to the low difference in the indices of refraction (Δn) of the semiconductors that can be grown lattice matched to GaAs substrates. Nevertheless, reflectivity in excess of 90 % has been recently reported for lattice-mismatched ZnSe/ZnTe[6] and ZnMgSe/ZnCdSe[7] systems.

In this chapter we report fabrication and characterization of DBR structures using ZnCdSe and ZnCdMgSe wide-gap semiconductors grown on InP substrates. Since ZnCdMgSe layers with a large range of band gaps (2.18 eV– 3.25 eV) can be grown lattice matched to InP, it is expected that high Δn values as well as good crystal quality can be achieved within this materials family. Furthermore, since QW and DBR structures are based on the same materials, using this alloy system it is possible to fabricate the DBRs together with the active layer in a single epitaxial process. This represents the first step towards the development of RCLEDs and other microcavity structures that can operate in the visible range.

We have fabricated several DBR structures from (Zn, Cd, Mg)Se materials. The structures were characterized by X-ray diffraction and

photoluminescence measurements. Reflectivity as high as 95.5 % was achieved for a DBR structure that consisted of 16 periods. The reflectivity maxima were controlled by the individual thicknesses of constituent layers, and were adjusted in the range of 615 – 500 nm, covering the red, green, and blue-green regions of the spectrum.

3-2 Experimental Techniques

Prior to the growth of the DBR structures, a series of calibration layers of ternary ZnCdSe and quaternary ZnCdMgSe alloys were grown to determine the composition, indices of refraction, and growth rates of the alloys used. The composition of the ternary ZnCdSe alloys was calculated assuming a linear dependence of lattice constant on the alloy composition (Vegard's law). The lattice constant was estimated using double crystal X-ray diffraction (DCXRD) measurements. Since the calibration layers could be partially strained, *(115) a* and *b* asymmetrical XRD measurements were made to obtain the perpendicular and parallel lattice constants: $a_{\perp}$ and $a_{||}$. The bulk lattice constant (a_0) was then calculated from the equation:

$$a_0 = a_{\perp}\{1-[2\nu/(1+\nu)][(a_{\perp} - a_{||})/ a_{\perp}]\} \quad (1)$$

where ν is a Poisson ration. A value of 0.28 was used for ν, which is the Poisson ratio for ZnSe.

The composition of the quaternary ZnCdMgSe alloys was determined by combining the lattice constant and bandgap energy data. The bandgap energy was estimated using a photoluminescence (PL) measurement system with a 325nm He-Cd laser as the excitation source. The equation for the dependence of bandgap energy of $Zn_xCd_yMg_{(1-x-y)}Se$ material system on the composition was obtained by assuming a quadratic dependence of bandgap energy on x and y: $E_g = ax^2 + by^2 + cxy + dx + ey + f$. A linear dependence of the bandgap for the $Cd_yMg_{1-y}Se$ ternary on y and for the $Zn_xMg_{1-x}Se$ ternary on x was assumed. A known relationship[10] for the bandgap energy of $Zn_{1-x}Cd_xSe$ was used. These four relationships were combined to describe the dependence of the bandgap energy (E_g) at 10 K on the composition x and y:

$$E_g(x, y) = -0.35xy - 0.83x - 1.87y + 3.65. \qquad (1) \quad 10\ K$$

Solution of this equation simultaneously with the expression for Vegard's law for the quaternary materials, based on the lattice constants for CdSe, ZnSe and MgSe:

$$a(x,y) = 5.667\,x + 6.076y + 5.89(1-x-y) \qquad (2)$$

gives the composition of the quaternary, in terms of x and y. Photoluminescence measurements of the test samples and DBRs were performed at 77 K. Since the variation of the ZnCdMgSe bandgap energy

(E_g) in this temperature range (10 to 77 K) is small (less than 15 meV), the error introduced by substituting the uncorrected E_g value into Equation (1) was negligible. The refractive indices of the epilayers grown was estimated by extrapolation from the dispersion curve[11] that was previously obtained for ZnCdMgSe layers of different bandgap energies using the prism coupler technique.[12] The values for the bandgap energies, alloy compositions, and refractive indices of the layers grown are listed in Table 3-1.

Electrical characteristics of n-type doped DBRs were studied by Hall effect measurements, current-voltage (I-V) measurements, and electrochemical capacitance-voltage (ECV) profiling. The ECV is a C-V measurement with an electrolyte solution is used as a Schottky contact. By making use of an electrochemical dissolution reaction, the material can be profiled to any depth at a controlled and calculated rate. The semiconductor /electrolyte interface behaves as a Schottky diode and thus permits carrier concentration measurements to be made in the conventional way. For the Hall effect measurements, 0.5 x 0.5cm squares (Van der Pauw geometry) were cut from the DBR structure grown on a semi-insulating substrate. For I-V measurements, gold dots (0.3 mm^2) were deposited on the top surface of the DBR structure grown on an n^+-InP substrate. Gold wires were attached to the back of InP substrate, which was covered with In and to the gold dots

on the top. ECV profiling was performed using a Bio-Rad PN 4300 ECV profiler. A solution of 1M NaOH and 1.25 M Na_2SO_3 was used as an electrolyte. This solution was previously developed for electrochemical etching of $Zn_xCd_yMg_{1-x-y}Se$ alloys.

The room-temperature reflectance of the DBRs was measured by a Cary 500 UV-Visible Spectrophotometer with a Variable Angle Specular Reflectance accessory. The data were calibrated using an Ag-coated mirror of known reflectivity as reference.

3-3 Results and Discussion

It is advantageous for the design of DBR structures to select alloys with the largest difference in the index of refraction (Δn). Index of refraction is, generally, inversely proportional to the bandgap energy for II-VI alloys. Therefore, it is desirable to use ZnCdMgSe alloys with the highest possible Mg composition for the low-reflectivity layer. However, there are some limiting factors in the selection of the ZnCdMgSe alloys. As was previously observed, in growing a series of ZnCdMgSe samples with successively increasing Mg concentration, the RHEED evolved from a streaky to spotty pattern, indicating a decrease in materials quality. The deterioration in quality was also verified by significant peak broadening of the DCXRD rocking curve and the PL emission peak.[13] Based on these results, we

conclude that ZnCdMgSe alloys with Mg concentration above 60 % were unsuitable for high-quality DBR structures.

With these constraints in mind we fabricated two ZnCdSe/ZnCdMgSe DBR structures with compositions and layer thicknesses designed to give a stop-band at around 600 nm. These structures have a relatively large difference in the indices of refraction between their layer materials ($\Delta n/n$ = 13% and 12%), and consist of 16 periods. In one DBR structure the two layers are closely lattice matched to the InP substrate ($\Delta a/a = 0.03\%$), while in the other the layers are symmetrically strained relative to the InP substrate ($\Delta a/a = -0.56\%$ for ZnCdMgSe and +0.74% for ZnCdSe). The use of strained layers allowed us to maintain the Zn, Cd, and Mg cell temperatures constant during the growth, greatly simplifying the growth process.

The spectra in Fig. 3-1 are the double crystal x-ray diffraction (DCXRD) scans for the lattice-matched (I) and mismatched (II) DBRs, respectively. In both spectra the sharp narrow peak corresponds to the (004) InP substrate reflection. For the lattice matched DBR-I (top graph), a single peak is obtained from the superlattice structure, suggesting that both layers are closely lattice matched. The full width at half maximum (FWHM) of the peak is only 72 arcsec, indicating good crystal quality. The spectrum of the

lattice-mismatched DBR-II is shown in the lower graph. A peak overlapping with the InP (004) Bragg reflection peak is assigned to the (004) reflection of the InGaAs buffer. The broad peak at 1200 arcsec is due to the ZnCdSe, and the one at –600 arcsec is ZnCdMgSe. The FWHM of the epilayer peaks are 300 to 400 arcsec. This peak broadening demonstrates deterioration in the crystal quality that is probably due to the partial lattice relaxation of the mismatched ZnCdSe and ZnCdMgSe layers. The 77 K PL spectrum of the lattice-matched DBR-I is shown in Fig. 3-2 (a). The strong peak at 2.16 eV is assigned to ZnCdSe, and the one at 2.86 eV to ZnCdMgSe. A similar spectrum was obtained for the lattice mismatched DBR-II, giving a bandgap (E_g) for ZnCdSe of 2.226 eV and for ZnCdMgSe of 3.039 eV. Combining the x-ray and PL results, we obtained the composition of the constituent DBR layers as $Zn_{0.52}Cd_{0.48}Se/Zn_{0.30}Cd_{0.28}Mg_{0.42}Se$ for DBR-I, and $Zn_{0.59}Cd_{0.41}Se/Zn_{0.16}Cd_{0.26}Mg_{0.58}Se$ for DBR-II. The bandgap energies and nominal thicknesses of the individual layers in the two DBR structures are listed in Table I, together with the calculated layer compositions.

The reflectivity spectra for DBRs I and II are shown in Fig. 3-3. A maximum reflectivity of 94.5 % is obtained for the lattice-matched DBR-I at around 605 nm, and of 95.5 % for the lattice-mismatched DBR-II at around 615 nm. The peak reflectance is slightly shifted compared with the intended

wavelength, due to small variations in the growth rate of the test samples and DBRs. The absence of the oscillations in the short-wavelength side of the stop-band is due to the onset of absorption by the $Zn_xCd_{1-x}Se$ layers. In spite of the material degradation in DBR-II, no differences are observed in the maximum reflectivity or the stop-band width of these two DBRs.

Since the absorption edge of the $Zn_{0.52}Cd_{0.48}Se$ is around 575 nm, we cannot use this material for DBRs operating in the green and blue regions of the spectrum. In that case, we have to use quaternary ZnCdMgSe material in both of constituent layers of the DBR. Two DBR structures that used low bandgap ZnCdMgSe as the high refractive index layer and high-bandgap ZnCdMgSe as the low refractive index layer were grown. These DBR structures consist of 14 (DBR-III) and 10 (DBR-IV) periods, and have a difference in the indices of refraction $\Delta n/n = 9\%$. The DBRs were designed to give a stop-band at around 500 nm. The DCXRD scans for the two DBRs are shown in Fig. 4 and 5. In both spectra the sharp narrow peak corresponds to the (004) InP substrate reflection. DBR-III, corresponding to the DCXRD spectrum in Fig. 3-4, is nearly perfectly lattice matched ($\Delta a/a < 0.01$). More than four satellite peaks on each side of the zero order peak are visible in the DCXRD rocking curve, indicative of a high quality periodic structure. The solid line represents the experimental spectrum, while the dotted line is the

theoretical simulation. From the simulation a period of 116 nm is calculated, which is quite close to the intended period of 108 nm. The DCXRD rocking curve of DBR-IV is shown in Fig. 3-5. Two overlapping peaks around 200 arcsec are assigned to the high and low bandgap ZnCdMgSe layers, that are nearly lattice matched. The FWHM of Gaussian fits to these peaks are only 50 and 70 arcsec, suggesting good crystal quality. A weak peak around 450 arcsec is assigned to the InGaAs buffer layer. This assignment is supported by the DCXRD spectrum of a thick InGaAs layer grown under the same conditions (see inset). The 77 K PL spectrum of the DBR-III is shown in Fig. 2 (b), giving E_g for the low bandgap quaternary of 2.688 eV and E_g for the high bandgap quaternary layer of 3.14 eV. For DBR-IV the E_g values are 2.651 and 3.1 eV, respectively. Combining the x-ray and PL data we obtain composition of the constituent layers of these DBR structures as $Zn_{0.22}Cd_{0.18}Mg_{0.60}Se$/ $Zn_{0.33}Cd_{0.33}Mg_{0.34}Se$ (III) and $Zn_{0.23}Cd_{0.18}Mg_{0.59}Se$/ $Zn_{0.34}Cd_{0.33}Mg_{0.33}Se$ (IV).

The reflectivity spectra for DBRs III and IV are given in Fig. 3-6. A maximum reflectivity of 87% is obtained for DBR-III at around 541 nm, and of 77% is obtained at around 507 nm for DBR-IV. The peak reflectance of DBR-III is somewhat red-shifted relative to the intended value. This is in agreement with the increase in the period thickness from 108 (intended) to

116 nm (calculated). The reflectivity spectrum for DBR-III exhibits a significant asymmetry. This asymmetry may be caused in part by a deviation in the optical thickness of a thin (~5 nm) ZnSe top protective layer, that was grown in order to prevent Mg in the top $Zn_{0.23}Cd_{0.18}Mg_{0.59}Se$ layer from oxidation by atmospheric oxygen. The optical characteristics of the DBRs are most sensitive to thickness errors in the layers closest to the surface, since this is where the penetration of the optical wave into the DBR is most significant. Other factors that may contribute to this asymmetry are fluctuations of the individual layer thicknesses.

The maximum reflectivity of DBR can be calculated using the equation, based on the transfer matrix method: [14]

$$R_{2N} = ((1-(n_l/n_1)(n_2/n_3)^{2N})/ (1+(n_l/n_1)(n_2/n_3)^{2N}))^2$$

Where in our case N is a number of pairs in a stack, n_l is the index of refraction of an air (1.0), n_2 and n_3 are the indices of refraction of the alternating layers, and n_l is the index of refraction of the substrate. The results of the calculations, performed by me, are shown in Fig. 3-7. Three lines plot the dependence of the reflectivity (in %R) on the number of periods (N) for ideal DBRs having the structural parameters of the four DBRs investigated. Only one plot is given for DBRs III and IV, since they have similar parameters. Open symbols represent experimental values

obtained from the MBE-grown DBRs described in this paper. As can be seen from the figure, the maximum reflectivity obtained from the DBRs is very close to the theoretical values. The slight discrepancy between the theoretical maximum and experimental results may be due to the absence in the calculation of the effects of interface losses caused by interface roughness, and of the assumption that the substrate is infinitely thick. The calculations predict that superlattices of 20 periods for DBRs I and II, and 26 periods for DBRs III and IV would have reflectivities greater than 99%.

An important aspect that must be addressed before RCLEDs can be seriously considered is the electrical conductivity of the DBRs, which is essential for current injection. A low conductivity is typically observed in Bragg mirrors due to the potential barriers between low and high bandgap layers of DBR. In order to address this problem, we fabricated an n-type doped DBR that was doped with chlorine and consisted of 12 periods (DBR-V). The reflectivity spectrum of a chlorine-doped DBR that consisted of 12 periods was measured and the maximum reflectivity of that structure was 89% at around 597 nm. A maximum reflectivity of 88% was obtained at around 617 nm from an undoped structure that consisted of 12 periods and was grown under the same conditions (DBR-VI). Therefore, the optical properties were not affected by doping.

The electrical characteristics of the n-type DBR structure were studied. Room temperature Hall effect measurement of the DBR structure gave a free electron density of 3.1 x 10^{18} cm^{-3} and a parallel mobility of 72 cm^2/Vs. This electron mobility was lower than that measured for bulk ZnCdSe and ZnCdMgSe epilayers at this doping concentration (≈ 200 cm^2/Vs),[15] possibly due to the interface scattering in the DBR structure. ECV profiling was performed to determine net carrier concentration ($n_d - n_a$) in the individual layers. The ECV profile plot is shown in Figure 3-8. Since the electrochemical etching rate in these materials was not known precisely, etching was continued until the substrate was reached. At this point the measured carrier concentration changed abruptly. The etching depth was then estimated from the known overall thickness of the DBR structure. Net electron concentration of 4.4 x 10^{18} cm^{-3} for ZnCdSe and 1.9 x 10^{18} cm^{-3} for ZnCdMgSe were measured by this technique, in general agreement with the Hall measurements and the expected values.

Electron transport perpendicular to the layers is of primary importance for device applications of these structures. Therefore, I-V measurements were performed on the structure. The I-V characteristics of the n-type DBR stack measured at room temperature is shown in the inset of Figure 3-8. A rectifying behavior, most probably due to the band offsets in the conduction

band, was observed. To explain the origin of the rectifying behavior I will discuss the charge carrier transport across the heterojunction. The band diagram of ZnCdSe and ZnCdMgSe is shown in Fig 3-9 (a). Band discontinuities occur in the conduction and valence band since the band gap of ZnCdMgSe is larger than the gap of ZnCdSe. Transport across the heterojunction barrier can occur via thermal emission or via tunneling. However, when the barriers are thick and high, tunneling and thermal emission of carriers are not efficient. The current flow is impeded, resulting in large series resistance. The rectifying behavior is expected to be minimized by the use of step graded or digitally graded layers, [16, 17] shown in Fig 3-9 (b) and (c). In the step-graded structures an extra intermediate composition layer is inserted and in digitally graded structures is grown at the interface. Since thermal and tunneling currents exponentially depend on the barrier height, the current transport is expected to increase.

3-4 Conclusion

Two types of DBR structures were fabricated using wide-gap II-VI semiconductor materials. Lattice matched (I) and lattice mismatched (II) ZnCdSe/ZnCdMgSe systems consisting of 16 periods showed a reflectivity of 94.5 % and 95.5 % at around 605 nm and 615 nm. Although the lattice mismatched DBR-II had an inferior crystal quality in comparison to the

lattice-matched DBR-I, no significant difference is observed in the reflectivity spectra of the two. To shift the reflectivity maximum toward the blue, two DBRs that used lower bandgap ZnCdMgSe as the high refractive index layer, and higher bandgap ZnCdMgSe as a low refractive index layer were also grown. These DBRs showed a reflectivity of 77 % at around 507 nm after growth of 10 periods and of 87 % at around 541 nm after growth of 14 periods. Theoretical calculations indicate that reflectivity above 99% can be achieved from these DBRs by growing 20 to 26 periods. The optical and electrical properties of chlorine-doped n-type ZnCdSe/ZnCdMgSe DBR structures were also investigated. Reflectivity spectra, similar to those of undoped DBR structures with the same number of periods, were observed from the doped structures. High carrier concentration in the constituent layers was achieved. We have previously demonstrated ZnCdSe / ZnCdMgSe quantum well (QW) structures grown lattice matched to InP substrates.[1] Since these DBR structures are based on the same materials, we should be able to combine the DBRs and the QW structures in a single epitaxial growth process. This will enable the growth of RCLEDs and other microcavity structures based on II – VI materials that can operate throughout the visible spectral range.

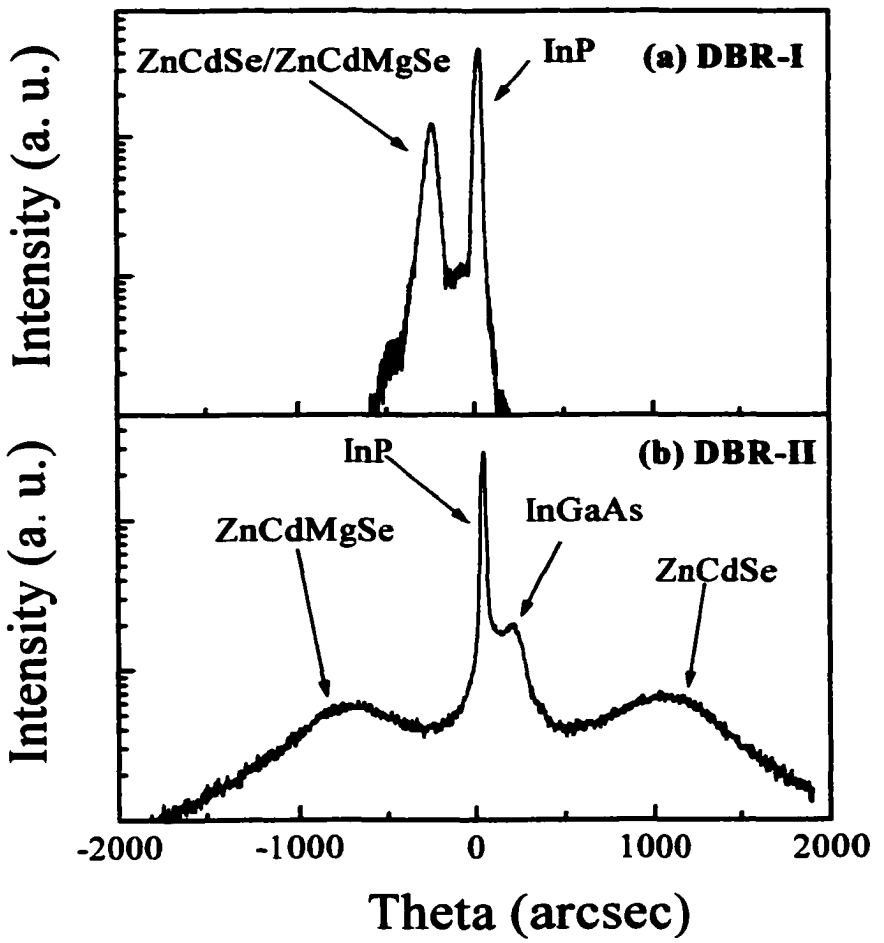

Fig. 3-1: DCXRD rocking curves obtained from DBR-I (a) and DBR-II (b).

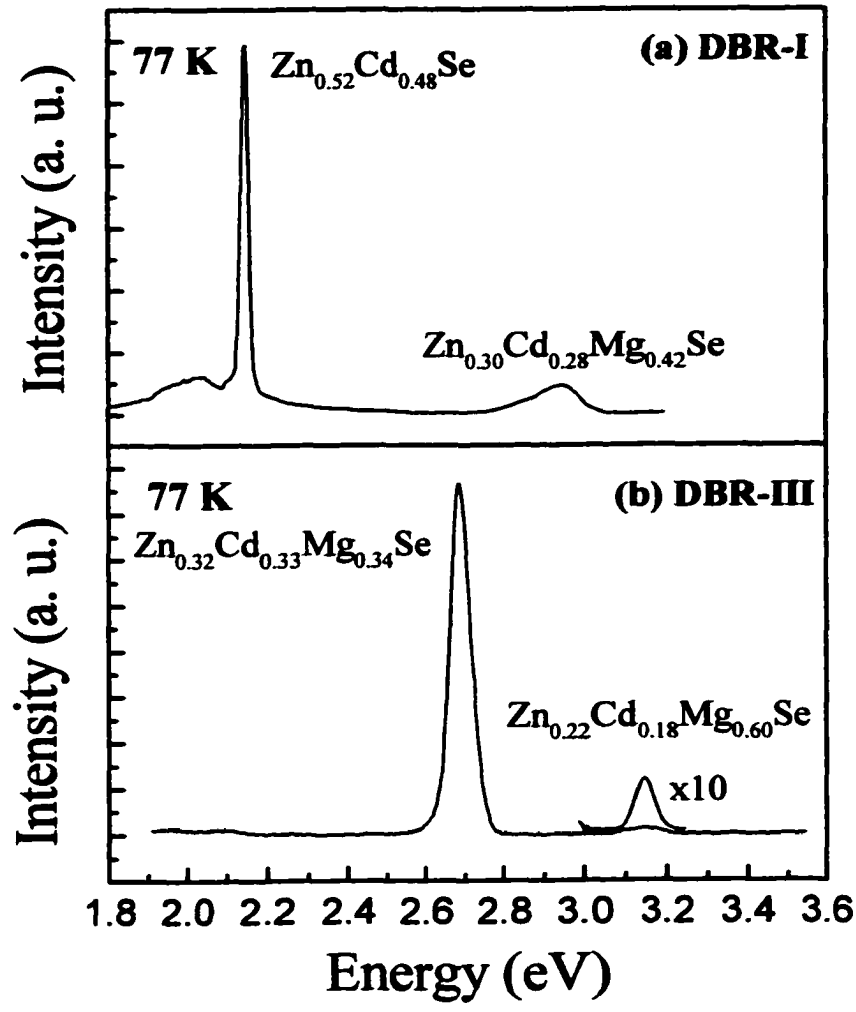

Fig. 3-2: PL spectra at 77 K from DBR-I (a) and DBR-III (b).

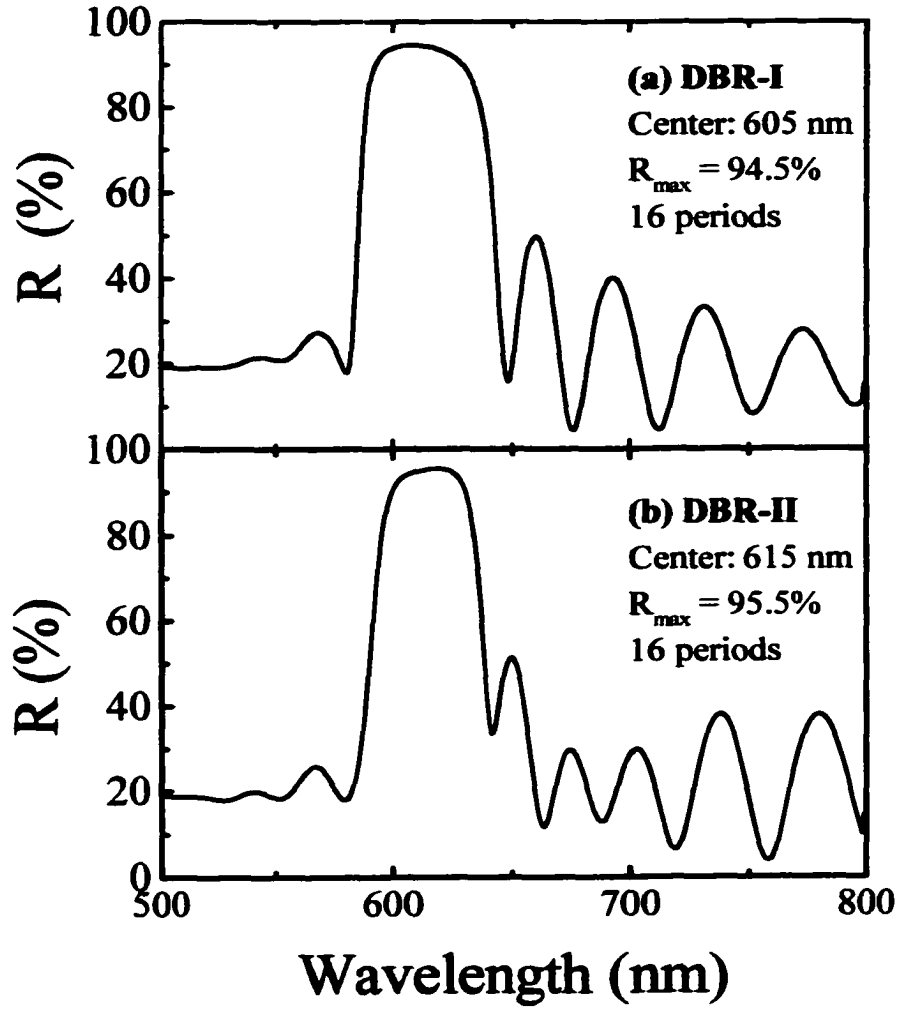

Fig. 3-3: Reflectivity spectra from DBR-I (a) and DBR-II (b) showing maximum reflectance of 94.5 % and 95.5 %, respectively.

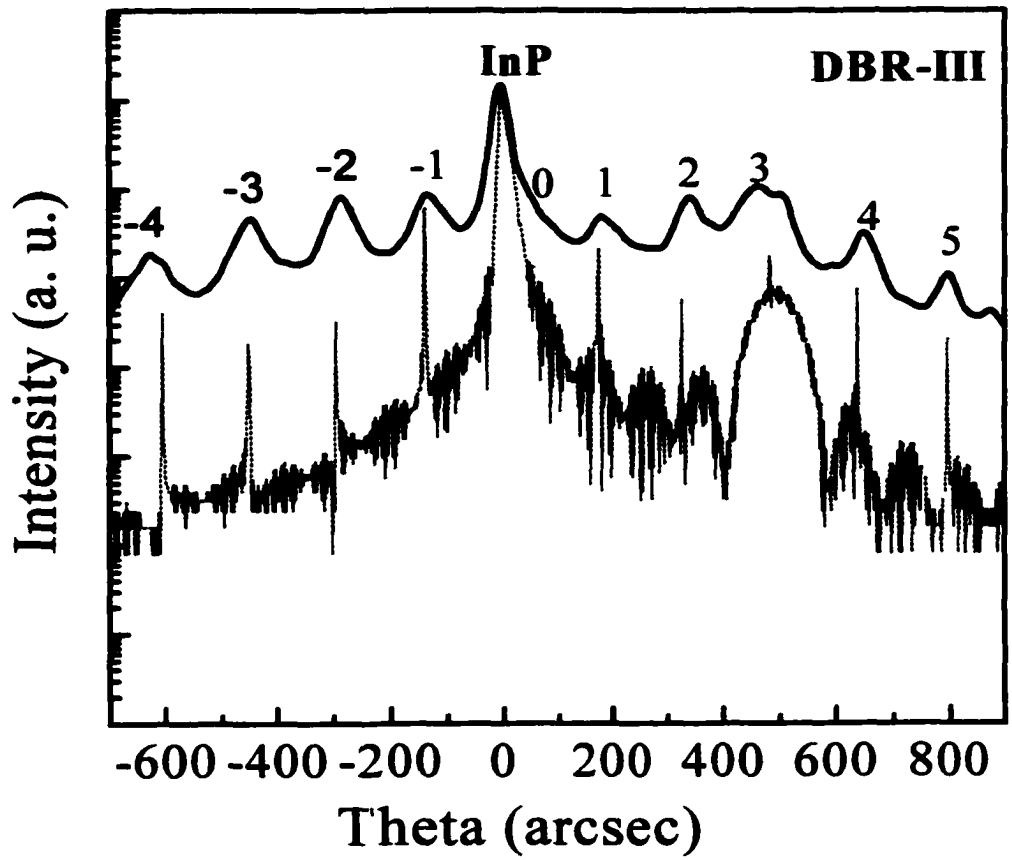

Fig.3-4: DCXRD rocking curve from DBR-III (solid line). Numbers on the figure denote superlattice reflection orders. The dashed line shows an XRD simulation data.

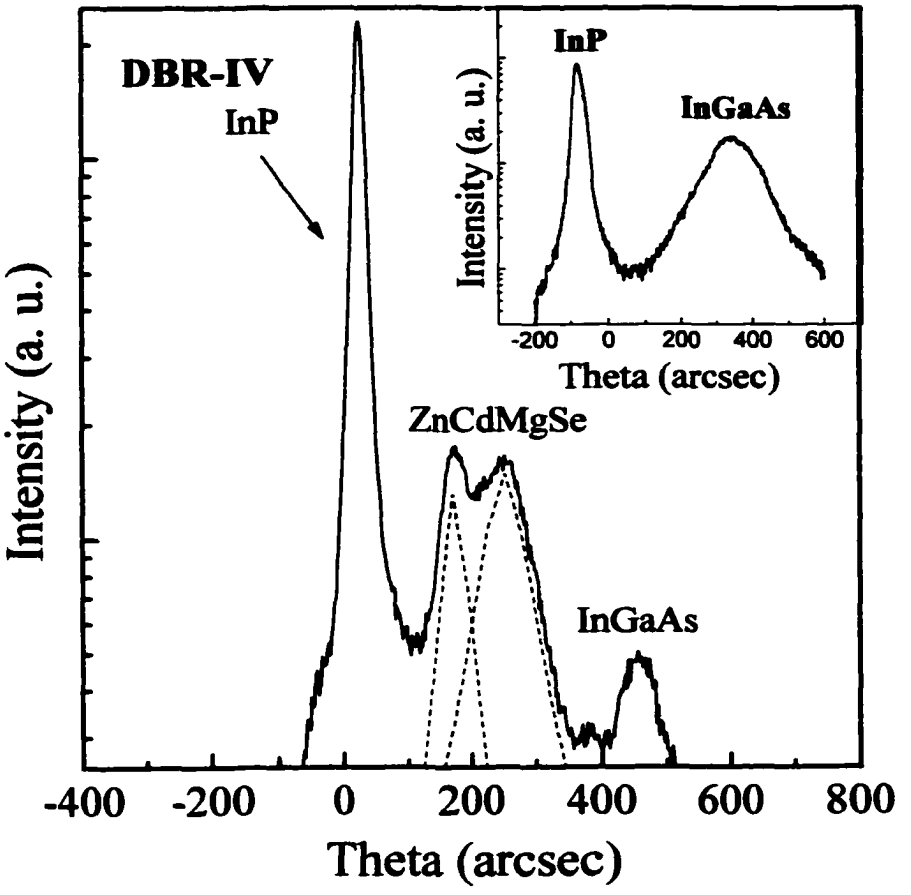

Fig.3-5: DCXRD rocking curve obtained from DBR-IV. The inset in the figure shows a DCXRD rocking curve from an InGaAs test sample grown under the same conditions.

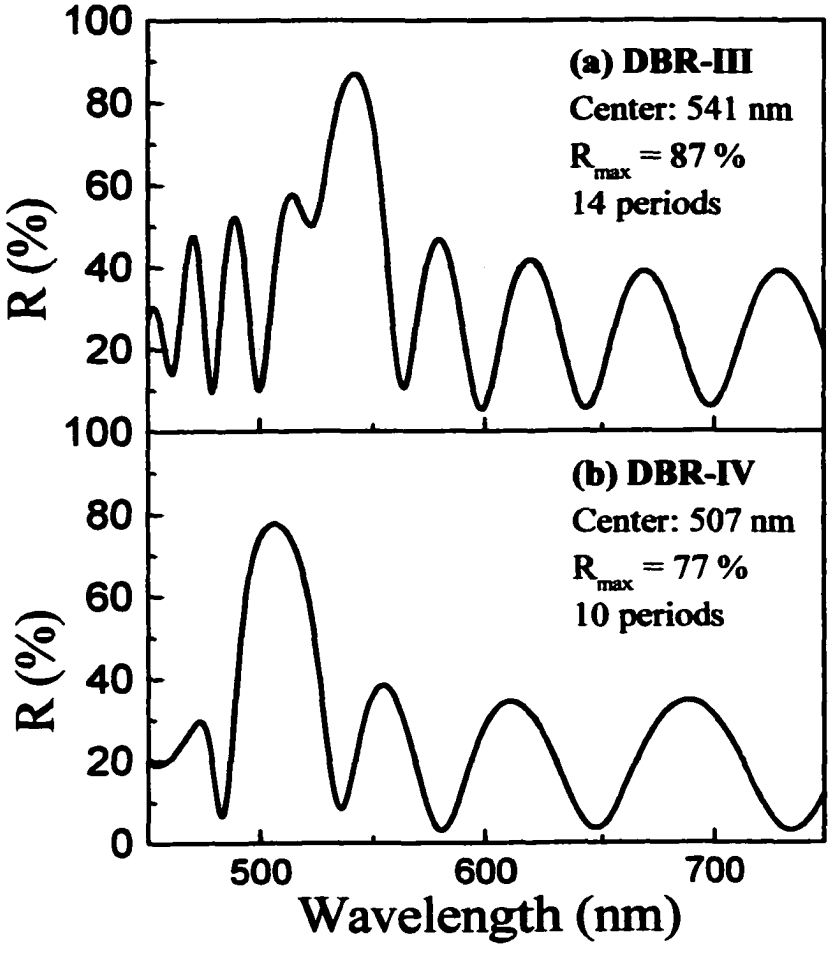

Fig.3-6: Reflectivity spectra from DBR-III (a) and DBR-IV (b) showing maximum reflectance of 87 % and 77 %, respectively.

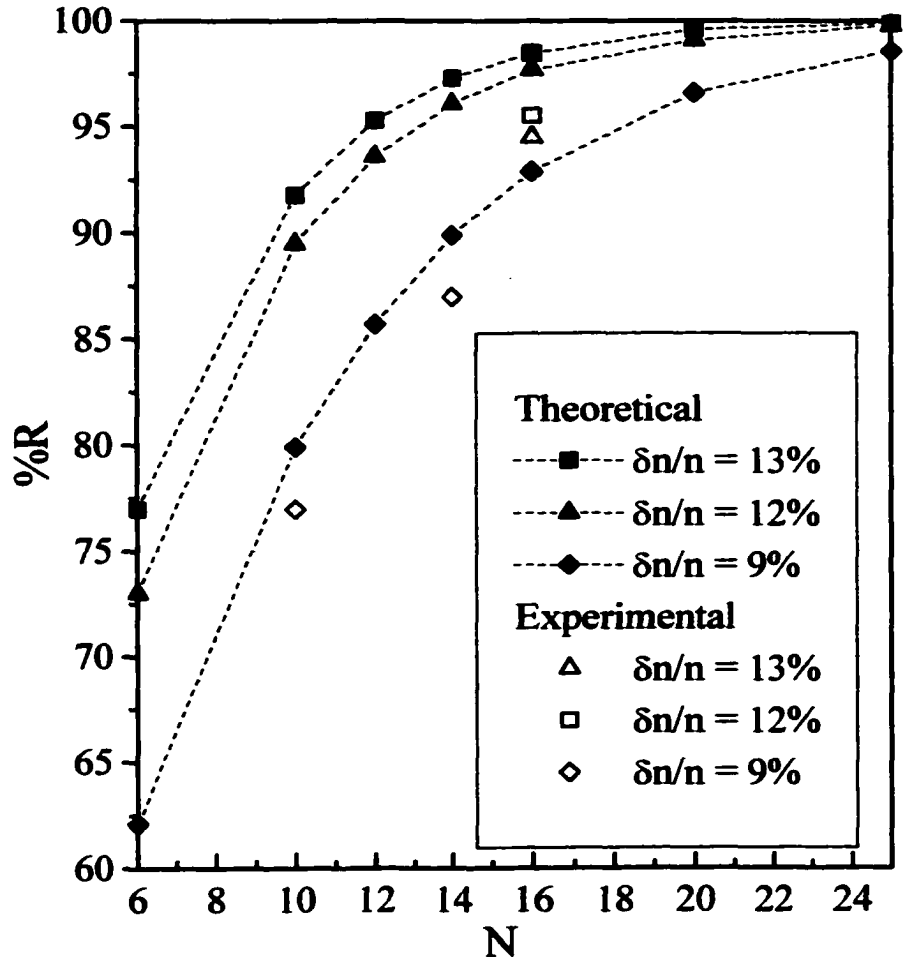

Fig.3-7: Theoretically calculated maximum reflectivity (% R) as a function of the number of periods (N) for DBRs with different Δn/n values (solid lines and symbols). Experimental reflectivity values for the grown DBR structures are shown by the open symbols.

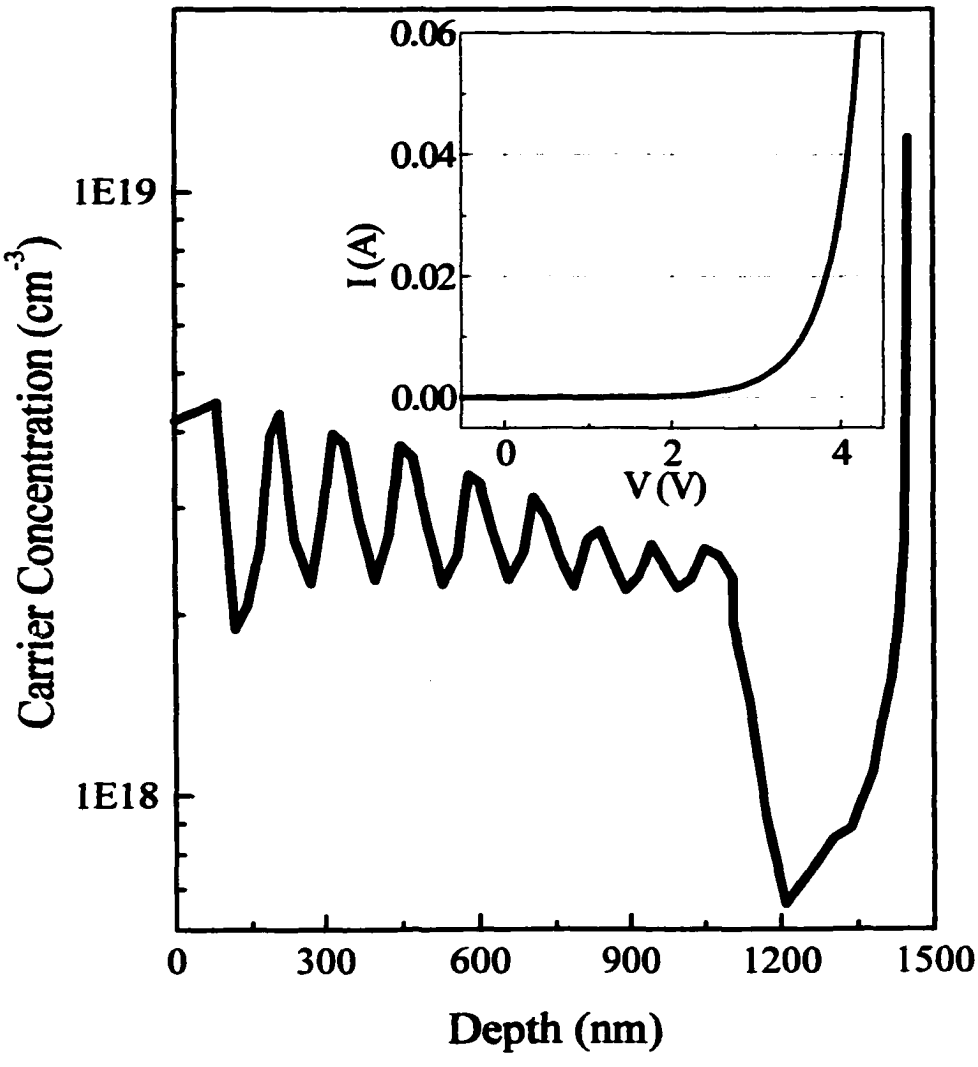

Fig.3-8: Electrochemical C-V profile for ZnCdSe/ZnCdMgSe n-type DBR structure with 12 periods, showing net electron concentration as a function of depth. Inset shows the I-V characteristics of the same structure measured at room temperature.

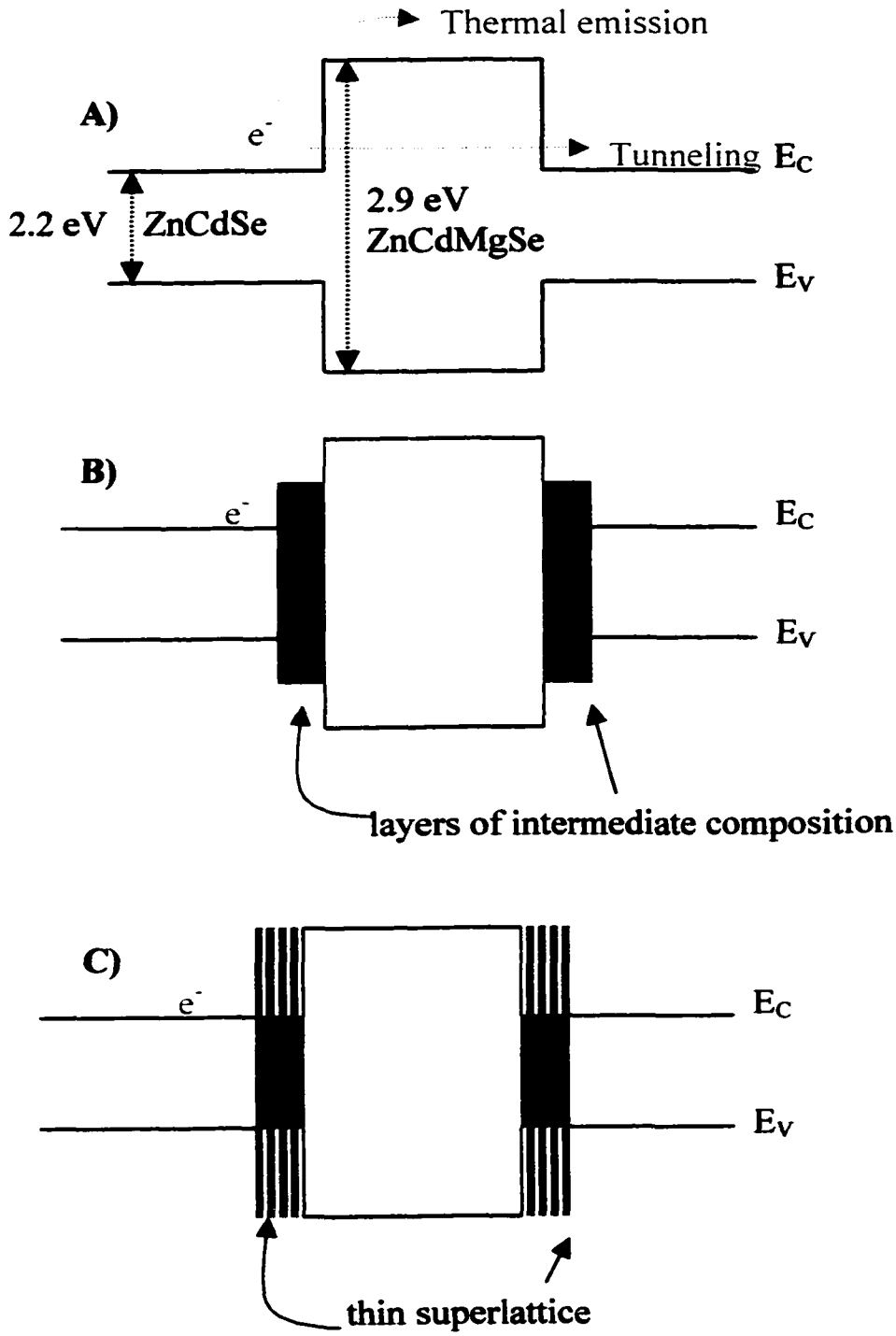

Fig. 3-9: Band diagrams of ZnCdSe/ZnCdMgSe heterostrucutres with ungraded interface (a), step-graded interface (b), and digitally graded interface (c).

Table 3-1. **Parameters of the DBR structures grown**

DBRs	Composition	Nominal Layer Thickness (nm)	Optical Layer Thickness (λ)	Eg (eV)	n	N	λ_{max} (nm)	%R Calc.	%R Exp.
DBR-I	$Zn_{0.52}Cd_{0.48}Se$/ $Zn_{0.30}Cd_{0.28}Mg_{0.42}Se$	56.1 63.9	0.25 0.25	2.16 2.86	2.72 2.39	16	605	97.5	94.5
DBR-II	$Zn_{0.59}Cd_{0.41}Se$/ $Zn_{0.16}Cd_{0.26}Mg_{0.58}Se$	54.6 63.0	0.24 0.24	2.226 3.039	2.71 2.35	16	615	98.5	95.5
DBR-III	$Zn_{0.32}Cd_{0.33}Mg_{0.34}Se$/ $Zn_{0.22}Cd_{0.18}Mg_{0.60}Se$	51.4 56.6	0.25 0.24	2.688 3.14	2.58 2.34	14	541	90.3	87
DBR-IV	$Zn_{0.34}Cd_{0.33}Mg_{0.33}Se$/ $Zn_{0.23}Cd_{0.18}Mg_{0.59}Se$	51.0 55.8	0.26 0.26	2.651 3.1	2.60 2.37	10	507	80.3	77

Chapter 4

Growth and characterization of $Be_xZn_yCd_{1-x-y}Se$ alloys

$Zn_xCd_{1-x}Se$/ $Zn_xCd_yMg_{1-x-y}Se$ quantum well (QW) structures lattice matched to InP substrates and grown by molecular beam epitaxy (MBE) exhibited emission energies from 2.15 to 3.0 eV, overlapping with most of the visible range.[1] For emission in the red, strained $Zn_xCd_{1-x}Se$ QWs with excess Cd ($\Delta a/a = 1.8$ %) had to be used.[2] However, the strain in the lattice-mismatched ZnCdSe QWs may enhance the multiplication and diffusion of point defects, decreasing the reliability of LEDs made from these materials. One of the approaches to improve reliability of LEDs is to increase the bond strength of the materials involved. Recently, theoretical considerations have been published, pointing out that beryllium chalcogenides have a much higher degree of covalent bonding compared to other wide gap II-VI compounds. [3] The covalency of the bonds in beryllium chalcogenides is expected to increase the bond strength. This is demonstrated in Figure 4-1, where the cohesive energy per bond (bond energy) is plotted versus hybrid covalency. [4] It can be seen from the figure that the bond energies for beryllium chalcogenides are in general higher as compared to conventional II-VI compounds like ZnSe and CdSe and reach values comparable with

GaN. It should also be mentioned that an increase in the lattice hardness of $Be_xZn_{1-x}Se_yTe_{1-y}$ alloy with the increasing Be content was reported. [5] Therefore, we propose that introduction of BeSe in the $Zn_xCd_{1-x}Se$ QW region should increase the bonding energy, decreasing the formation of point defects and suppressing the propagation of extended defects. Therefore, devices made from Be-based alloys may be less prone to degradation than those made from other II-VI materials.

In this chapter, we report the MBE growth and the properties of a $Be_xZn_yCd_{1-x-y}Se$ alloy, aimed to improve the active region of the red diodes. $Be_xZn_yCd_{1-x-y}Se$ ($x < 0.2$) epilayers were grown and high crystalline quality and good optical properties were demonstrated. The dependence of $Be_xCd_{1-x}Se$ band gap energy on composition was investigated and fitted to the quadratic equation: $1.78x + 5.6(1-x) - 2.6x(1-x)$.

Two approaches were used to explore the $Be_xZn_yCd_{1-x-y}Se$ material system. Ternary $Be_xCd_{1-x}Se$ epilayers were grown in the first approach. We started with CdSe and were increasing the Be content, until we achieved lattice-matched conditions, with 20% of BeSe ($Be_{0.2}Cd_{0.8}Se$). Quaternary $Be_xZn_yCd_{1-x-y}Se$ epilayers were grown in the second approach. We started with $Zn_{0.5}Cd_{0.5}Se$ and increased the Be content while decreasing Zn content thus remaining lattice matched to the InP substrate.

In order to optimize the growth conditions, the growth of $Be_xCd_{1-x}Se$ was studied with VI/II flux ratios varying from 4 to 12. When the growth was performed with a flux ratio below 8, the RHEED pattern initially showed a (3x1) surface reconstruction. Then, it changed to a diffused spotty pattern during the growth of the first tens of nanometers, indicating a three-dimensional growth mode. The crystalline quality of the samples grown under these conditions was poor, as evidenced by the broad X-ray rocking curve line widths. Either no PL signal or a weak and broad emission was observed from these samples. A similar (3x1) surface reconstruction followed by the fast RHEED pattern degradation was observed for $Be_{0.22}Cd_{0.78}Se$ layers grown on GaAs substrates by Ivanov et al.[6] When the growth was performed with a VI/II flux ratio above 8, a streaky (2x1) RHEED pattern, typical for group VI-rich conditions, was observed. Samples grown with this flux ratio exhibited high crystalline quality and good optical properties. High quality $Zn_xCd_{1-x}Se$ and $Zn_xCd_yMg_{1-x-y}Se$ layers have been previously grown using a VI/II flux ratio of ~ 4.[7] We believe that the higher Se flux required for the growth of $Be_xCd_{1-x}Se$ was due to the additional heating of the sample surface by thermal radiation from the high-temperature Be cell (>900 ^{0}C).

In order to investigate the crystalline properties, $Be_xZn_yCd_{1-x-y}Se$ films were studied by θ-2θ double crystal XRD measurements. The (004) reflection X-ray rocking curves for $Be_{0.2}Cd_{0.8}Se$ and $Be_xZn_yCd_{1-x-y}Se$ epilayers with different Be mole fractions, that are closely lattice matched to InP, are shown in Fig. 4-2 (a), (b), and (c). In all spectra two peaks are observed: one is from the InP substrate and another is from the $Be_xZn_yCd_{1-x-y}Se$ epilayer. The full width at half maximum (FWHM) of the epilayer peaks varies from 39 to 60 arcsec, indicating high crystalline quality of the closely lattice-matched epilayers.

The 10 K PL spectra for $Be_{0.2}Cd_{0.8}Se$ and two $Be_xZn_yCd_{1-x-y}Se$ epilayers discussed above are shown in Fig. 4-3 (a), (b), and (c). The PL emission line for a closely lattice-matched $Zn_{0.5}Cd_{0.5}Se$ epilayer is also shown by a dashed line in Fig. 4-3 (c) for comparison. The PL emission lines from $Zn_{0.5}Cd_{0.5}Se$ is only 36 meV above the PL emission line from $Be_{0.2}Cd_{0.8}Se$, indicating that when lattice matched these alloys have similar band gap energies. The PL emission lines have an asymmetric shape with a tail at the low energy side. The absence of deep level emission is indicating high quality of epilayers.

The (004) reflection X-ray rocking curves for three $Be_xCd_{1-x}Se$ layers with different Be mole fractions are shown in Figures 4-3 (a), (b), and (c). In

all spectra two peaks are observed: one from the InP substrate and another from the $Be_xCd_{1-x}Se$ epilayer. For a closely lattice matched 0.9 μm thick $Be_{0.2}Cd_{0.8}Se$ epilayer ($\Delta a/a = 0.01\%$), the full width at half maximum (FWHM) of the epilayer peak is 49 arcsec, as shown in Fig. 4-4 (a). The narrow line width implies a very high crystalline quality for the nearly lattice-matched epilayer. The X-ray rocking curve for a 0.8 μm thick $Be_{0.14}Cd_{0.86}Se$ epilayer with a lattice mismatch of $\Delta a/a = 0.92\%$ is shown in Fig. 4-4 (b). It has a slightly broader peak, with a FWHM of 68 arcsec, indicating a high crystalline quality in spite of the large mismatch. The X-ray rocking curve for a 1.7 μm thick $Be_{0.09}Cd_{0.91}Se$ epilayer with a lattice mismatch of $\Delta a/a = 1.76\%$ is shown in Fig. 4-4 (c). It exhibits a broad peak with a FWHM of 900 arcsec, indicating a lower crystalline quality. A reduction of the crystalline quality and broadening of the X-ray peak with the increase of lattice mismatch is expected due to the formation of misfit dislocations.

The PL spectra for the three $Be_xCd_{1-x}Se$ layers discussed above are shown in Figure 4-5. The PL emission peaks have an asymmetric shape with a tail at the low energy side. Figure 4-6 shows a plot of the FWHM of the PL emission peaks at 77 K as a function of composition. The top axis shows the lattice-mismatch to the InP substrate. It is interesting to note that the PL line width increases linearly from 23 to 47 meV with increasing Be content.

However the X-ray peaks become narrower as we increase the Be content and thus approach the lattice-matched conditions. This indicates that the observed PL emission line broadening is not due to the decrease in the crystalline quality. A set of $Be_x(Zn_{0.38}Cd_{0.62})_{1-x}Se$ samples which had constant Zn/Cd ratio and differed only in Be content was also grown. The 10 K PL spectra for these epilayers are shown in Fig. 4-7. Again, it is evident that with the increase in Be content, the emission lines become broader and a tail in a low energy side appears. A similar asymmetric broadening with the increase in Mg content was previously observed for the ZnCdMgSe band-edge emission peaks.[8] In that case, it was suggested that the ZnCdMgSe band-edge emission peak was a sum of a narrow free exciton recombination peak and a broad emission peak related to the recombination of excitons localized in the broad band tail by one longitudinal phonon energy.[9] Another possible explanation for the increase of the PL line width is the inhomogeneous broadening due to potential fluctuations with the increase of Be-content in the alloy.

In order to examine the origin of the luminescence, we plotted the integrated PL intensity of $Be_{0.2}Cd_{0.8}Se$ emission line (solid circles), measured at 10 K, as a function of the excitation intensity (I_{ex}) on the logarithmic scale as shown in Fig. 4-8. A linear dependence with a slope

near unity (k = 1.08) was observed. The $Be_{0.2}Cd_{0.8}Se$ emission energy (open circles) as a function of the excitation laser density was studied and no energy shift was observed. These results indicate that the PL emission is dominated by excitonic radiative recombination.

Band gap dependence of $Be_xZn_yCd_{1-x-y}Se$ alloy on composition was studied. Band edge emission energies for $Be_xCd_{1-x}Se$ and $Be_xZn_yCd_{1-x-y}Se$ epilayers are plotted in Fig. 4-9 with solid and open circles, respectively. The dependence of $Be_xCd_{1-x}Se$ band gap energy on composition is fit to the quadratic equation (dotted line):

$$E_g = 1.78(1-x) + 5.6x - 2.6x(1-x) \qquad (1)$$

where 1.78 eV is a band gap energy for CdSe,[10] 5.6 eV is a band gap energy for BeSe,[11] and 2.6 eV is a bowing parameter. Due to a strong bowing, the band gap energy of $Be_{0.2}Cd_{0.8}Se$ is only 2.128 eV (at 10 K), close to the band gap energy of $Zn_{0.5}Cd_{0.5}Se$ (2.213 eV), which is also lattice-matched to InP at this composition. Therefore, $Be_xZn_yCd_{1-x-y}Se$ epilayers, when they are closely lattice matched to InP substrates, have band gap energy that varies only from 2.128 eV to 2.213 eV. Introduction of BeSe in the QW region should increase alloy hardness, without significantly changing the band gap energy.

The $Be_xCd_{1-x}Se$ band gap dependence on composition was also previously investigated by Nekrutina *et al* and a bowing parameter of 4.5 eV was reported. [12] Significant discrepancy exists between their data and ours. The comparison is shown in Fig. 4-9. We believe that our results are more accurate since they are based on the PL emission from the bulk ternary layers, while their band gap values were estimated based on the PL emission from $Be_xCd_{1-x}Se$/ZnSe QW structures.

In conclusion, epitaxial layers of $Be_xZn_yCd_{1-x-y}Se$, with up to 20% of BeSe ($x \leq 0.2$), were grown by MBE on InP substrates. High quality layers with narrow X-ray rocking curves and sharp and intense PL emission lines were obtained. The dependence of $Be_xCd_{1-x}Se$ band gap energy on composition was investigated. Our results indicate that $Be_{0.2}Cd_{0.8}Se$, which is the composition that is lattice matched to InP, has a band gap energy of 2.128 eV at 10 K. These results suggest that $Be_xZn_yCd_{1-x-y}Se$ should be an attractive material for lasers and LEDs emitting in the visible region of the spectrum.

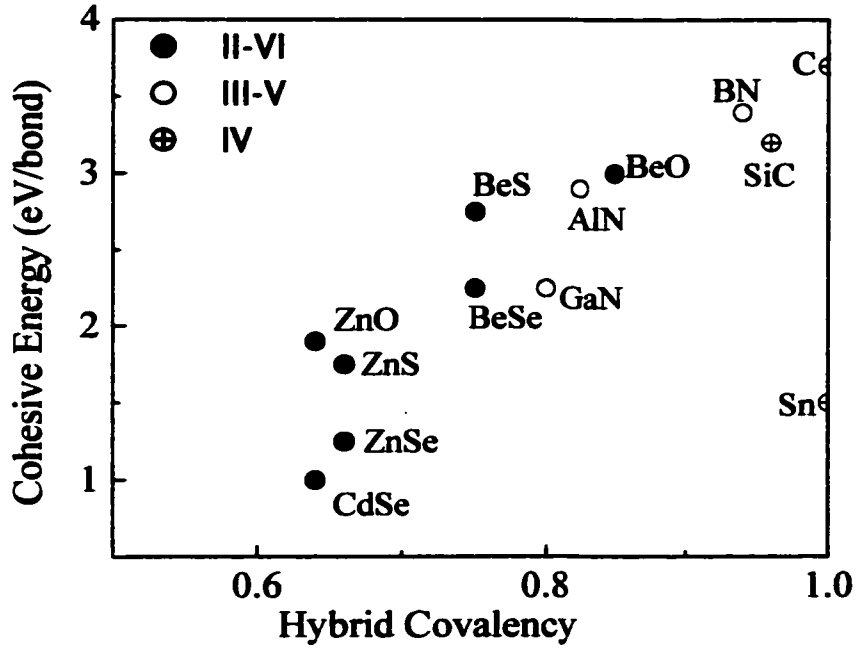

Fig. 4-1: Cohesive energy per bond as a function of covalency.

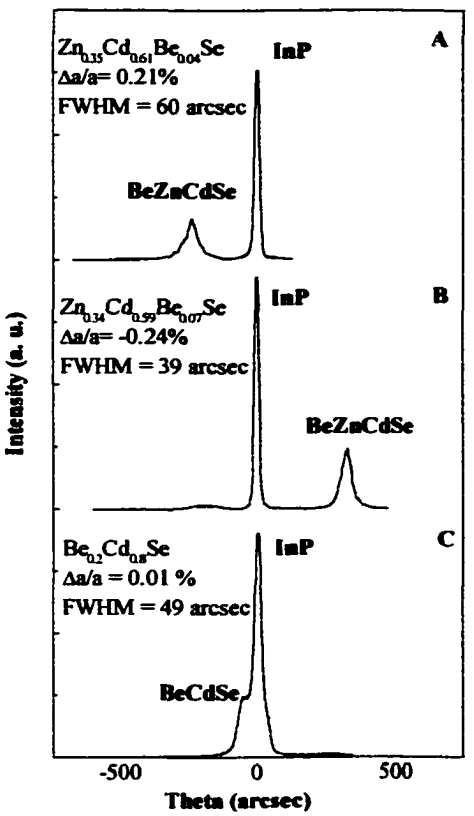

Fig. 4-2: (004) X-ray rocking curves for three $Be_xZn_yCd_{1-x-y}Se$ layers with different composition grown on InP substrates: (a) $Be_{0.04}Zn_{0.35}Cd_{0.61}Se$, (b) $Be_{0.07}Zn_{0.34}Cd_{0.59}Se$, and (c) $Be_{0.2}Cd_{0.8}Se$.

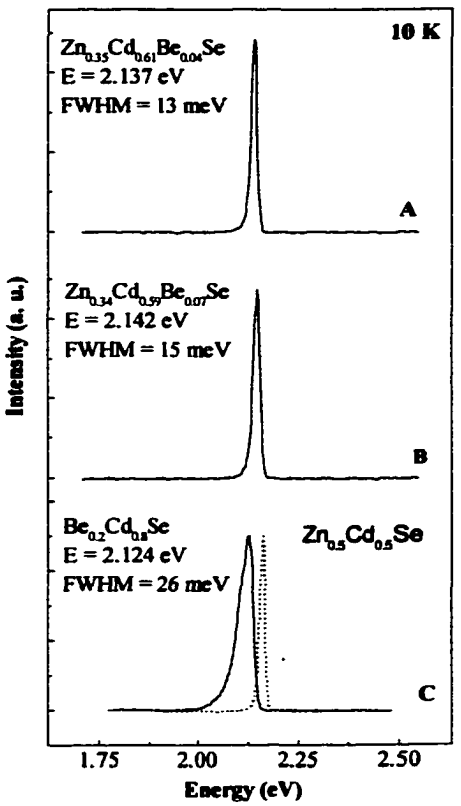

Fig. 4-3: 10 K PL spectra for four $Be_xZn_yCd_{1-x-y}Se$ layers with different composition grown on InP substrates: (a) $Be_{0.04}Zn_{0.35}Cd_{0.61}Se$, (b) $Be_{0.07}Zn_{0.34}Cd_{0.59}Se$, and (c) $Be_{0.2}Cd_{0.8}Se$ (solid line) and $Zn_{0.5}Cd_{0.5}Se$ (dashed line).

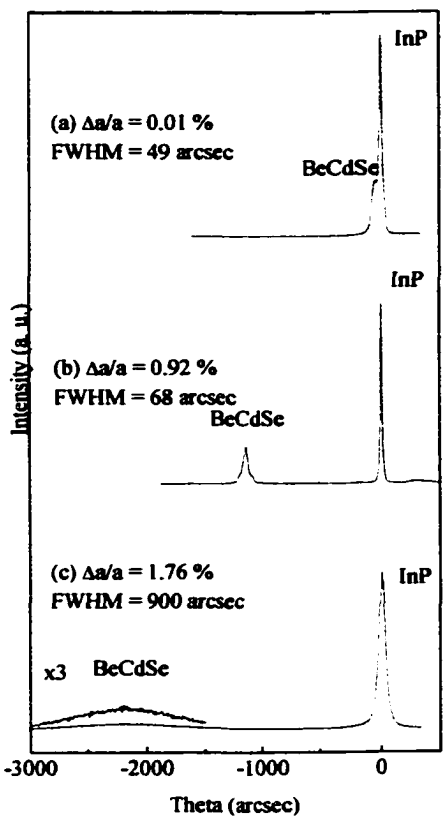

Fig. 4-4: (004) X-ray rocking curves for three $Be_xCd_{1-x}Se$ layers with different composition grown on InP substrates: (a) $Be_{0.2}Cd_{0.8}Se$, (b) $Be_{0.14}Cd_{0.86}Se$, and (c) $Be_{0.09}Cd_{0.91}Se$.

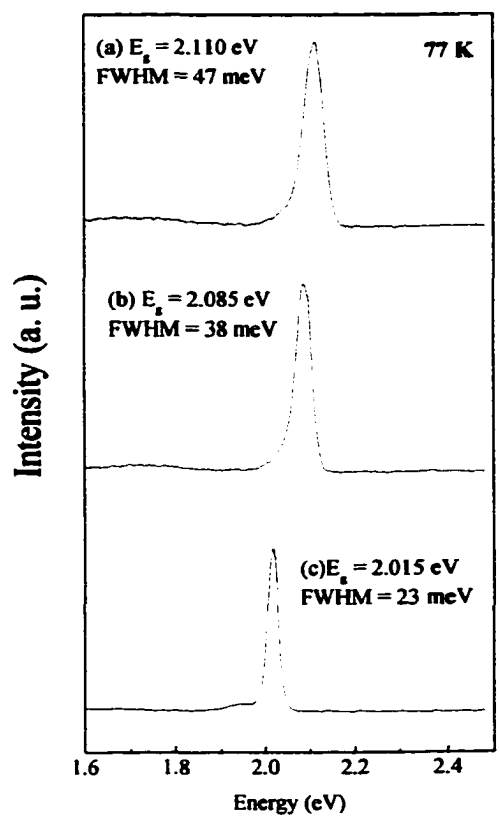

Fig. 4-5: 77 K PL spectra for three $Be_xCd_{1-x}Se$ layers with different composition grown on InP substrates: (a) $Be_{0.2}Cd_{0.8}Se$, (b) $Be_{0.14}Cd_{0.86}Se$, and (c) $Be_{0.09}Cd_{0.91}Se$.

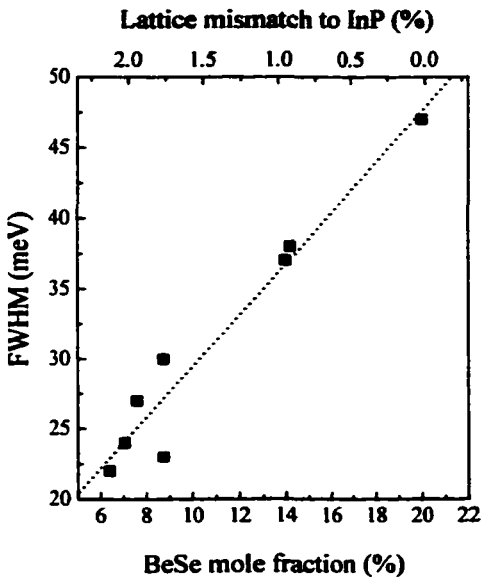

Fig. 4-6: FWHM of the PL emission from $Be_xCd_{1-x}Se$ epilayers as a function of Be mole fraction. Solid squares are the experimental results and the dashed line is a linear fit.

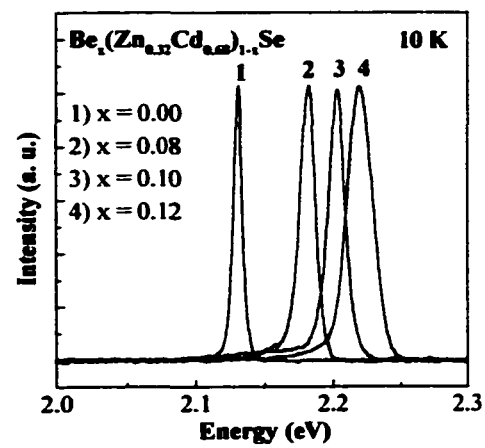

Fig. 4-7: 10 K PL spectra for four $Be_x(Zn_{0.38}Cd_{0.62})_{1-x}Se$ epilayers with various Be composition (x).

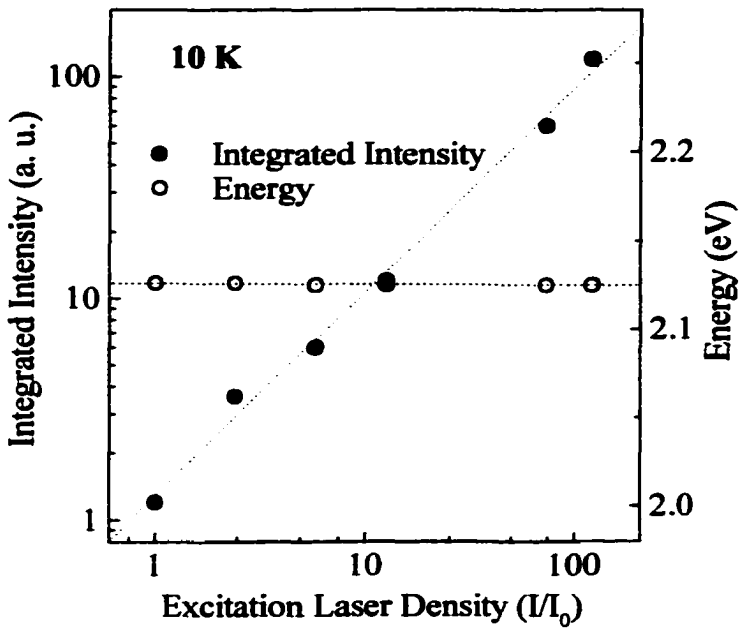

Fig. 4-8: Dependence of the integrated emission intensity (solid circles) and emission energy (open circles) on the excitation laser density at 10 K in a log scale. The dashed lines are linear fits.

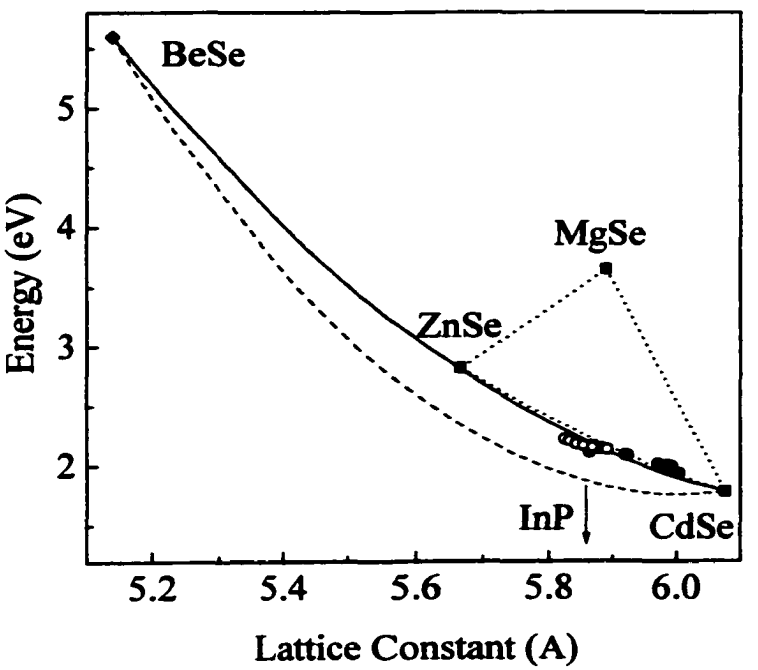

Fig. 4-9: Near band edge PL emission energy at 10 K for $Be_xCd_{1-x}Se$ (solid circles) and $Be_xZn_yCd_{1-x-y}Se$ (open circles) epilayers. The solid line is a fit for the direct band gap energy of $Be_xCd_{1-x}Se$ alloy as a function of composition. The dashed line is the band gap dependence of $Be_xCd_{1-x}Se$ alloy on composition reported by Nekrutina *et al* [14].

Chapter 5

Optical properties of $Be_{0.08}Cd_{0.92}Se$/ZnCdMgSe strained quantum wells

The growth, optical properties and band gap dependence of $Be_xCd_{1-x}Se$ on composition were described in a previous chapter. It was determined that high quality $Be_xCd_{1-x}Se$ epilayers can be grown under the conditions compatible with ZnCdMgSe growth. Strong low and room temperature emission in the visible range of a spectrum was observed from $Be_xCd_{1-x}Se$ epilayers indicating that $Be_xCd_{1-x}Se$ is interesting as a QW material.

In this chapter we report optical properties of BeCdSe/ZnCdMgSe structures with strained BeCdSe ($\Delta a/a = 1.95$ %) QWs. A set of structures with nominal QW thickness varying from 95 to 12 Å was grown by molecular beam epitaxy (MBE). Efficient luminescence from the red to the green regions of the spectrum was observed from QW structures that differed only in the QW thickness. Sharp luminescence lines, consistent with high quality interfaces were obtained. The temperature and the excitation intensity dependence of the photoluminescence (PL) emission were studied for the structure with a 48 Å-thick QW. These studies showed that the QW emission was dominated by exciton recombination processes. From the

Arrhenius plot of the integrated intensity as a function of temperature, activation energies for the BeCdSe QW emission and the ZnCdMgSe barrier layer emission were estimated. The temperature dependence of BeCdSe QW emission energy, an important parameter for design of lasers and light emitters, was investigated and fitted to the Varshni's and Bose-Einstein equations. The broadening of the QW emission line width with temperature was studied using a similar Bose-Einstein type equation.

QW structures were grown using a ternary of nominal composition $Be_{0.08}Cd_{0.92}Se$ (E_g = 2.018 eV at 10 K) as the well layer. The structures consisted of a lower 500 nm - thick ZnCdMgSe ($E_g \approx 2.9$ eV at 10 K) barrier layer, a $Be_{0.08}Cd_{0.92}Se$ active layer, and a top 100 nm - thick top ZnCdMgSe barrier layer with the same composition as the bottom one was grown. The structure was capped by a 5 nm - thick pseudomorphic ZnCdSe cap layer to protect ZnCdMgSe from oxidation by atmospheric oxygen. The ZnCdMgSe barrier layers were nearly lattice matched ($\Delta a/a < 0.15$ %) to InP, and the BeCdSe QW layer was strained with $\Delta a/a$ = 1.95 %. The QW mismatch estimate was based on the single crystal X-ray diffraction (XRD) measurement of a thick BeCdSe layer (E_g = 2.018 eV at 10 K) with the same nominal composition as the QW, grown just prior the QW structures.

Fig. 5-1 (a) shows the 10 K PL spectrum of the structure with a 48 Å - thick QW layer. The band-edge emission from the ZnCdMgSe barrier layer is at 2.909 eV and that from the QW layer is at 2.078 eV. The absence of deep level emission is indicative of the high quality of the QW structure. The asymmetric line shape with a tail in the low energy side may be related to the involvement of localized exciton emission, which may be due to composition fluctuations[1] and/or thickness deviations of the well width.[2, 3]

The RT PL spectrum for the same sample is shown in the Fig. 5-1 (b). A strong emission at 1.996 eV is obtained from the QW while the emission from the ZnCdMgSe barrier layer is thermally quenched. An increase of the full width at half maximum (FWHM) of the QW emission with increasing temperature is observed (from 22 meV to 71 meV) due to the phonon broadening. A weak shoulder at ≈ 2.18 eV originates from the top ZnCdSe cap layer.

The PL emission energy at 10 K from a series of QW structures is plotted as a function of QW thickness in Fig. 5-2 (a). [The data is also shown in table 5-1.] Each data point represents a different growth run. The quaternary barrier layers had a band gap at around 2.9 eV, indicated by a bar on the left axis of the plot. The band gap of a thick $Be_{0.08}Cd_{0.92}Se$, which is

the composition used in the QW, is 2.018 eV and is marked by another bar on the right axis of the plot.

The QW emission energy data fit, indicated by a solid line, was performed using the analytical method by Mathieu et al.[4] For our calculations, we used the effective mass values of CdSe: $m_e = 0.11 m_0$ for electrons and $m_h = 0.44\ m_0$ for holes.[5] These values were used both for the wells and for the barrier materials. The distribution of the band offsets ($\Delta E_c/\Delta E_v$) was varied, and the best fit was obtained with $\Delta E_c/\Delta E_v = 70/30$.

The $Be_{0.08}Cd_{0.92}Se$-based QW structures presented here can be tuned to a lower energy than those based on $Zn_{0.55}Cd_{0.45}Se$ QWs,[6] reaching an emission energy of 2.1 eV (useful for red light emitters) with a 48 Å -thick $Be_{0.08}Cd_{0.92}Se$ QW layer. At this thickness the strained active layer is pseudomorphic and free of misfit dislocations.

From the width of the PL emission lines we can obtain an assessment of the quality of our QW structures. Fig. 5-2 (b) shows a plot of the FWHM of the PL emission lines from the BeCdSe QWs as a function of QW thickness for the same set of samples as those shown in Fig 5-2 (a). Narrow emission lines (FWHM < 25 meV) are obtained for the thick QWs (> 40 Å), suggesting that the interfaces of the QWs are smooth and abrupt.

As expected, the line widths increase with the decrease in QW thickness. This is due to the increasing effect of the interface roughness as the QWs become thinner.

Fig. 5-3 shows the dependence of the integrated QW emission intensity on the excitation laser density measured at 77 K in a logarithmic scale. Solid squares represent the experimental results and the dashed line is a linear fit. A linear dependence with a slope of 1.04 is obtained. The QW emission energy as a function of the excitation laser density is shown by open circles and no energy shift is observed. These results indicate that the QW emission has an excitonic recombination behavior.

The temperature dependence of the PL intensity has been also studied for the structure with a 48 Å -thick QW layer. Figure 5-4 shows an Arrhenius plot of the integrated QW (solid triangles) and barrier (open squares) emission intensity as a function of the inverse temperature. The experimental data can be fitted to the formula:

$$I(T) = I_0/(1 + C\exp(-E_a/kT)) \qquad (1)$$

where I_0 and C are constants, T is the temperature, k is Boltzmann's constant, and E_a is the activation energy. Activation energies of 61 ± 2 meV and 30 ± 1 meV were obtained for the QW and barrier layer emissions, respectively. The activation energy obtained for the

$Be_{0.08}Cd_{0.92}Se$/ZnCdMgSe QW emission was comparable to that reported for $Zn_xCd_yMg_{1-x-y}Se/Zn_{x'}Cd_{y'}Mg_{1-x'-y'}Se$ QWs (68 meV) [7] and much higher than that reported for $Zn_{0.5}Cd_{0.5}Se$/ZnCdMgSe (20 meV) [7] and $Zn_{0.8}Cd_{0.2}Se$/ZnSSe/ZnMgSSe (25 meV) [8] QWs with similar thickness. High activation energies indicate high luminescence efficiencies even at high temperatures, which are desirable for RT operation of light emitting devices. The activation energy obtained for the ZnCdMgSe barrier layer emission was similar to the value previously reported for ZnCdMgSe barriers (31 meV). [7]

We have plotted the luminescence line width of the same structure versus temperature in Figure 5-5. The measured luminescence line width is a sum of an inhomogeneous part (Γ_i), which is due to interface roughness, composition fluctuations, alloy scattering, electron-electron interactions, impurities and dislocations, and a temperature-dependent homogeneous part (Γ_h). The homogeneous component is dominated by the scattering of longitudinal acoustic phonons (LA) at low temperature and by longitudinal optic (LO) phonons at higher temperatures. By neglecting the contribution from the LA phonons, the value of the electron (exciton) -LO-phonon (Fröhlich) interaction constant (Γ_{LO}) and LO phonon energy ($h\nu_{LO}$) can be

determined by fitting of the FWHM of the QW emission to the equations: [9, 10]

$$\Gamma(T) = \Gamma_i + \Gamma_h \qquad (2)$$

$$\Gamma_h = \Gamma_{LO}/(\exp(h\nu_{LO}/kt) - 1) \qquad (3)$$

The best fit gave us $\Gamma_i = 23.3 \pm 0.7$ meV, $\Gamma_{LO} = 82 \pm 16$ meV and $h\nu_{LO} = 26 \pm 3$ meV. The LO phonon energy, obtained through this fit, is very close to that obtained from bulk CdSe epilayers (25.9 meV). [11, 12] This is reasonable, since the BeCdSe QW contains only 8% BeSe. However, the electron-LO-phonon interaction constant is much higher than the reported for the bulk CdSe layer (23 meV). [11] Similar electron-LO-phonon interaction constants have been reported for ZnSe/ZnMgSSe QWs (60 – 80 meV). [13, 14]

We have plotted the QW emission energy versus temperature in Figure 5. The solid circles are the experimental results and the dotted line is a theoretical fit based on the Varshni's relationship: [15]

$$E_V(T) = E_0 - \alpha T^2/(\beta + T) \qquad (4)$$

where E_0 is the fundamental transition energy at 0 K and α and β are constants, known as Varshni's coefficients. The best fit gave us $E_0 = 2.079$ eV, $\alpha = 0.37 \pm 0.03$ meV/K and $\beta = 249 \pm 39$ K.

The data was also fit to the Bose-Einstein relationship (solid line): [16]

$$E_{BE}(T) = E_0 - 2a_B/(e^{\theta/T} - 1) \qquad (5)$$

where E_0 is the fundamental transition energy at 0 K, a_B represents the strength of the electron-average phonon interaction, and θ corresponds to the average phonon temperature. The best fit gave us $E_0 = 2.078$ eV, $a_B = 35 \pm 2$ meV and $\theta = 210 \pm 8$ K. It should be noted that a_B and θ are close to the values reported for the bulk CdSe ($a_B = 36$ meV and $\theta = 179$ K) [12] layers.

The results of the fittings to the Bose-Einstein and Varshni's equations can be compared in the high temperature limit in which the two equations reduce to:

$$E_V \approx E_0 - \alpha T$$

$$E_{BE} \approx E_0 - 2a_B T/\theta$$

From the comparison of these equations it follows that $\alpha = 2a_B/\theta$. By substituting the values of a_B and θ obtained from the fitting to the Bose-Einstein equation we obtain $\alpha = 0.34$ meV/K. This is in a good agreement with the value obtained from the Varshni's relationship ($\alpha = 0.37 \pm 0.03$ meV/K), indicating consistency between the parameters obtained by the two techniques.

In conclusion, quantum well structures having ZnCdMgSe barrier layers and BeCdSe QW layers were grown and their optical properties were investigated. Emission from the red to the green regions of the visible

spectrum was obtained from the QW structures by varying only the QW thickness. Efficient luminescence was observed both at 10 K and at room temperature. The PL intensity as a function of excitation laser density showed a linear dependence with a slope near unity, indicating an excitonic recombination behavior. The temperature dependence of the PL intensity of a structure with a 48 Å -thick QW was studied and an activation energy (E_a) of ≈61 meV was obtained. The LO phonon energy and the electron-LO-phonon interaction constant were estimated and compared with those of other II-VI materials. Also, the temperature dependence of BeCdSe QW emission energy was measured and was fit to the Varshni's and Bose-Einstein equations. Parameters that describe the temperature dependence of the QW emission were obtained. Our results indicate that BeCdSe-based QW structures are attractive for application as red light emitters.

Table 5-1 Parameters of $Be_{0.08}Cd_{0.92}Se$/ZnCdMgSe QW structures

QW Thickness (Å)	Emission Energy (eV)	FWHM (meV)
11.9	2.57	46.2
23.8	2.381	37.6
35.7	2.201	29
47.6	2.078	21.9
95.2	2.034	20.8
Bulk layer	2.010	19

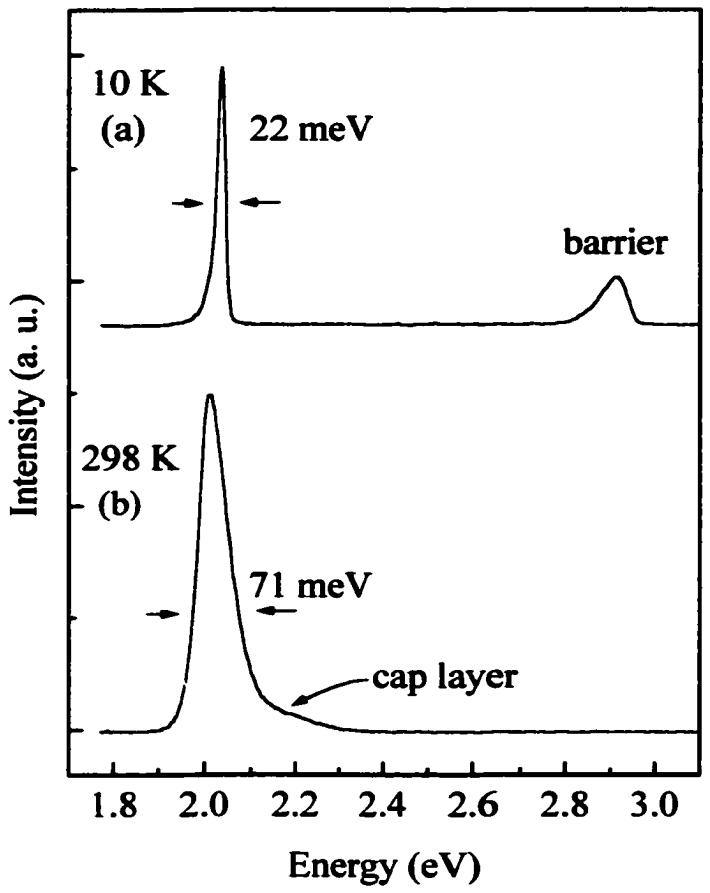

Fig. 5-1: Photoluminescence spectra for a 48 Å - thick BeCdSe/ZnCdMgSe QW at a) 10 K and b) 298 K.

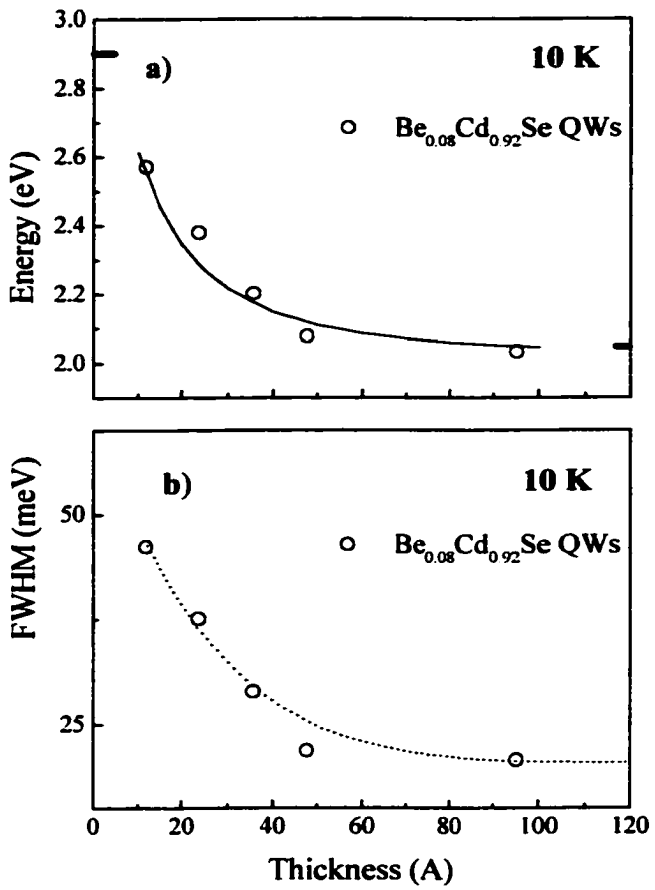

Fig. 5-2: a) Emission energy at 10 K as a function of QW width for BeCdSe/ZnCdMgSe QWs (open circles) grown on InP substrates. The solid line is a fit based on the analytical method by Mathieu et al (Ref. 12). b) FWHM of emission lines for BeCdSe/ZnCdMgSe QWs (open circles) grown on InP substrates. The dashed line is drawn for visualization.

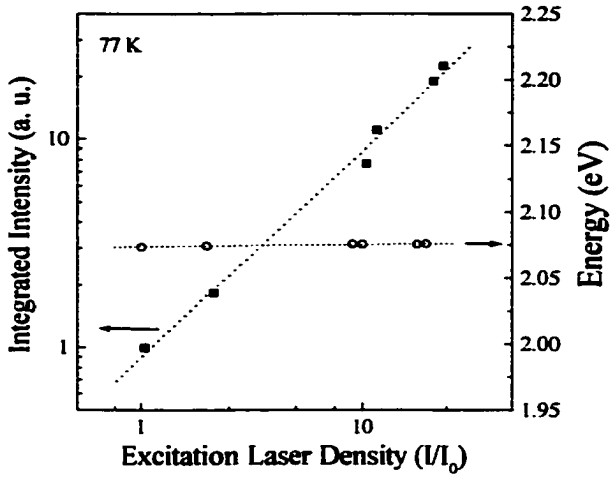

Fig. 5-3: Dependence of the integrated QW emission intensity (solid squares) and emission energy (open circles) on the excitation laser density at 77 K in a log scale. The dashed lines are linear fits.

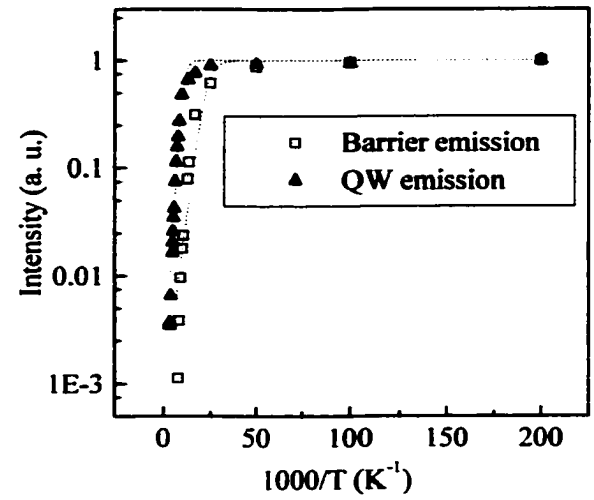

Fig. 5-4: Arrhenius plot of the QW (solid triangles) and the barrier layer (open squares) emission intensities as a function of inverse temperature for a 48 Å-thick BeCdSe/ZnCdMgSe QW.

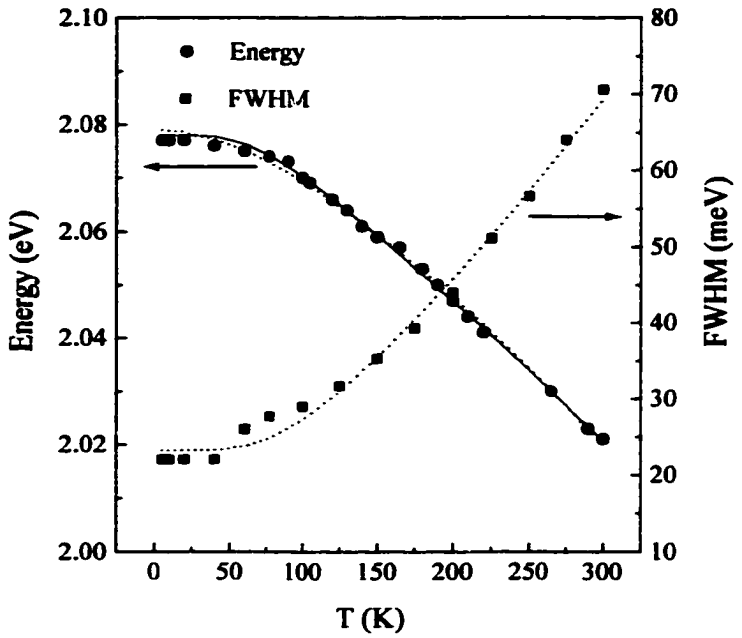

Fig. 5-5: The FWHM (solid squares) and energy (solid circles) of the QW emission as a function of temperature for the 48 Å-thick BeCdSe/ZnCdMgSe QW. The dashed lines represent fits based on the electron-LO-phonon coupling model and Varshni's relationship. The solid line represents a fit based on the Bose-Einstein relationship.

Chapter 6

Growth and characterization of $Be_xZn_{1-x}Te$ alloys

In the past few years ZnCdMgSe-based light emitting diodes (LEDs) operating in the visible range of the spectrum were reported by several research groups.[1-3] The LED structures, which were grown on InP substrates, utilized lattice-matched ZnSeTe or ZnMgSeTe as the top p-type contact layers. However, there are drawbacks involved in the use of each of these materials. In the case of ZnSeTe, which can be doped p-type to carrier concentration levels in excess of 10^{19} cm^{-3}, absorption of the visible light by the top contact layer limits the performance of surface emitting LEDs.[4] When ZnMgSeTe layers with band gaps of 3.1 eV are used, the maximum free hole concentration is in the low 10^{18} cm^{-3}, making the formation of ohmic contacts more difficult.[2]

A promising alternative material for use as a p-type contact layer is $Be_xZn_{1-x}Te$. Previous studies showed that, with a BeTe mole fraction (x) of ≈ 0.48, it can be lattice matched to the InP substrates, and that it can be doped p-type to the 10^{19} cm^{-3} level.[5,6] Furthermore, since BeTe and ZnTe have direct band gaps of 4.1 eV[7] and 2.26 eV, it is expected that $Be_xZn_{1-x}Te$ layers lattice matched to InP will not absorb in the visible range. However, BeTe is

an indirect semiconductor with an indirect $\Gamma \rightarrow X$ band gap transition at 2.8 eV,[7] while ZnTe is a direct band gap semiconductor. Therefore, the band gap of the $Be_xZn_{1-x}Te$ ternary alloy should undergo a direct-to-indirect crossover at some value of x. The position of this crossover is still unknown. The potential development of heterostructures based on this new material requires an investigation of the band gap properties of $Be_xZn_{1-x}Te$.

In this chapter we report the molecular beam epitaxy (MBE) growth and characterization of $Be_xZn_{1-x}Te$ epitaxial layers on InP (100) substrates. The dependence of the Be content on the Be and Zn cell temperatures was investigated and good reproducibility from run to run was observed. Small compositional fluctuations in the $Be_xZn_{1-x}Te$ epilayers were explained by the possible variations of the substrate temperature. Crystalline properties of the epilayers were studied by double crystal x-ray diffraction (XRD) and etch pit density (EPD) measurements. Narrow x-ray rocking curves (72 – 78 arc sec) and low etch pit density (5×10^5 cm^{-2}) were obtained for the closely lattice-matched epilayers indicating high crystalline quality. The crystalline quality of the $Be_xZn_{1-x}Te$ epilayers under the compressive and tensile strain was compared. A slower decrease in the crystalline quality (due to relaxation by formation of misfit dislocations) for epilayers under tensile strain compared to epilayers under compressive strain was observed.

We have investigated the room temperature (RT) reflectivity and low-temperature photoluminescence (PL) of a set of $Be_xZn_{1-x}Te$ epilayers with x varying from 0 to 0.7. We determined the variation of the $Be_xZn_{1-x}Te$ band gap as a function of BeTe content (x) and estimated that the position of the direct-to-indirect crossover is at $x \approx 0.28$. Our results indicate that $Be_{0.48}Zn_{0.52}Te$, which is lattice matched to InP, is an indirect semiconductor with a $\Gamma \rightarrow X$ indirect band gap at 2.77 eV and a $\Gamma \rightarrow \Gamma$ direct band gap at 3.14 eV.

The control of composition during the MBE growth of the $Be_xZn_{1-x}Te$ alloy system was investigated. The composition was controlled by adjusting the Be and/or Zn cell temperatures. Two experiments were performed. In the first experiment several samples were grown in which we increased the Be cell temperature with the Zn cell temperature held constant at 183 ^{0}C. In the other experiment we decreased the Zn cell temperature with the Be cell temperature held constant at 960 ^{0}C. The Be content increased linearly on a logarithmic scale with the increase (decrease) in the Be (Zn) cell temperature, as shown in Figure 6-1. Good reproducibility from run to run was observed.

The crystalline quality of the layers was studied by θ-2θ double crystal XRD measurements. The (004) reflections of the double crystal x-ray

rocking curve for $Be_xZn_{1-x}Te$ epilayers with different Be mole fractions are shown in Fig 2. In all spectra the dominant peak is from the InP substrate and the others originate from the epilayer. In Fig. 6-2 (a) and (b), a single peak with the full widths at half maximum (FWHM) in the range 70 - 90 arc sec is observed, indicating high quality material. In a few cases two closely overlapping peaks related to the $Be_xZn_{1-x}Te$ epilayer were observed, as shown in Fig. 6-2 (c). In this case, similar spectra were obtained from different areas of the wafer suggesting the presence of two regions with slightly different Be content ($x = 0.50$ and 0.51) as a function of depth. A strong dependence of the $Be_xZn_{1-x}Te$ composition on the growth temperature was previously reported. [6] For example, in our experiments we observed that an increase in the growth temperature from 270 ^{0}C to 300 ^{0}C resulted in a compositional change from $x = 0.45$ to $x = 0.50$. This strong substrate temperature dependence may be due to the fact that the Zn sticking coefficient decreases with the increase in the growth temperature, while the Be sticking coefficient remains nearly constant in this temperature range. [8] Therefore, we propose that the observed compositional variations [Fig. 6-2 (c)] may be due to small fluctuations of the substrate temperature during the growth.

The defect density of the epilayers was investigated by EPD measurements. A concentrated HCl solution (32 %) was used. This solution has been previously reported to be a suitable etchant for $Be_xZn_{1-x}Se$, $Be_xMg_yZn_{1-x-y}Se$, and $Mg_xZn_{1-x}S_ySe_{1-y}$ alloys. [9-11] The etching behavior was examined by changing the etching time. The $Be_xZn_{1-x}Te$ layers were etched for 30, 60, 90, and 120 seconds and their surface was studied using Nomarski microscope and AFM. No defects were seen on the as-grown surface. When etched for 30 seconds, etch pits became resolvable. With the increase in the etching time, the pits grew bigger and deeper. However, the density remained constant during the etching and did not depend on etch time. Figure 6-3 shows an AFM image (40 μm x 40 μm) of the $Be_{0.51}Zn_{0.49}Te$ epilayer after the etching for 60 seconds in HCl. The pits have an oval shape with a size of 3μm x 1μm and are very deep, in excess of 150 nm. We suggest that these pits correspond to stacking faults and/or dislocations, although a more detailed study is necessary to verify this.

The properties of the $Be_xZn_{1-x}Te$ epilayers grown in this study are summarized in Table 6-1. The FWHM of the x-ray rocking curves (solid circles) and the EPD values (open circles) for these epilayers are plotted as a function of lattice mismatch (Δa/a) to the InP substrate in Fig. 6-4. The epilayer quality decreases with the increase of the lattice mismatch as is

evident from the broadening of the x-ray rocking curves and the increase in the defect density. This is likely due to relaxation of the layer by the formation of misfit dislocations to accommodate strain. The FWHM of the x-ray rocking curves and the EPD values for the epilayers under tensile strain increase much more slowly with respect to lattice-mismatch than for the epilayers under compressive strain. $Be_xZn_{1-x}Te$ layers under tensile strain have a higher Be content than those under compressive strain, as shown in Table 6-1. An increase in the lattice hardness with the increase in the Be content was previously reported for $Be_xZn_{1-x}Se$ and $Be_xZn_{1-x}Se_yTe_{1-y}$ alloys. [12, 13] We suggest that $Be_xZn_{1-x}Te$ layers with higher Be content can accommodate a larger misfit strain by elastic deformation without the formation of misfit dislocations, due to the expected increase in the lattice hardness.

Figure 6-5 shows reflectivity spectra measured at 298 K for six $Be_xZn_{1-x}Te$ layers ranging in composition from $x = 0.06$ to $x = 0.52$. The end of Fabry-Perot oscillations in the reflectivity spectrum corresponds to the onset of interband absorption and can be identified as the $\Gamma \rightarrow \Gamma$ direct band gap transition. The exact position of the absorption edge was taken to be the first minimum of the derivitive of the reflectivity spectrum. The reflectivity measurements shown in Figure 6-5 indicate that the band gap continuously

shifts to a higher energy as the Be concentration increases. The band gap energy increases linearly with BeTe content at a rate of 18 meV for a change of 1% in BeTe content.

Figure 6-6 shows normalized PL spectra measured at 6 K for the same group of samples. The PL spectra are dominated by narrow emission lines. In several spectra a second, usually weak peak is present at lower energy, about 50 meV below the high-energy peak. It can be seen from the data in Figure 6-6 that the energy of the dominant PL peak initially increases with Be content and then becomes nearly constant at a value of $x \geq 0.28$. It should be noted that the intensity of the PL decreased sharply as the BeTe content became larger than that value, and continued to decrease as the Be content increased.

Based on their optical properties the samples can be divided into two different groups. For $Be_xZn_{1-x}Te$ with $x < 0.28$, the PL emission energy increases with Be content. In this group of samples, the PL emission energy, which is measured at 6K, is about 90 meV above the room temperature bandgap value obtained from the reflectivity measurements, consistent with the expected variation of bandgap with temperature. Thus, the PL emission in this group of samples is assigned to the $\Gamma \rightarrow \Gamma$ near bandedge emission. For the $Be_xZn_{1-x}Te$ with $x \geq 0.28$ the PL emission energy is nearly constant

while the direct bandgap value continues to increase linearly with composition. Therefore, our results suggest that the $Be_xZn_{1-x}Te$ layers with $x \geq 0.28$ are indirect band gap materials. This conclusion is also supported by the reduced PL intensity observed for these samples.

In Figure 6-7 we have plotted the direct band gaps obtained from reflectivity measurements (open circles) and the PL emission energies (crosses) as a function of Be content for a larger set of samples that includes the six shown in Figures 6-5 and 6-6. Using the room temperature band gap measured for ZnTe (2.263 eV) and the reported value for the direct bandgap of BeTe (4.1 eV)[7], the reflectivity data can be well fitted to the linear equation:

$$E^{\Gamma}_{g}(x) = 2.263*(1-x) + 4.1*x \qquad \text{for } 0 \leq x \leq 1 \quad (1)$$

which describes the RT direct bandgap dependence on composition for this alloy. The same equation corrected for the temperature difference describes the behavior of 6 K PL data for samples with $x < 0.28$.

To analyze the PL data for $x \geq 0.28$, we must consider the $\Gamma \rightarrow X$ band gap energy for the binary end points. The value for BeTe is well known to be at 2.8 eV.[7] However, the $\Gamma \rightarrow X$ transition energy for ZnTe is not known precisely. Recently, a value of 3.05 eV was reported,[14] while a value of 3.45 eV was obtained using *ab initio* calculations.[15] The values the same

authors report for the X → X transition (5.45 eV[14] and 5.63 eV[15]) are comparable to the values measured by other groups (5.23 eV[16] and 5.30 eV[17]). Assuming that the PL emission energies for the samples with x above 0.28 correspond to the Γ → X indirect band gap transition, we have fitted the variation of the Γ → X indirect band gap with composition (x) to the equation:

$$E^{X}_{g}(x) = 3.05*(1-x) + 2.8*x - 0.5*x*(1-x) \text{ for } 0 \leq x \leq 1 \quad (2)$$

where 0.5 eV is a bowing parameter. A good correlation of this equation with our data was obtained, while attempts to fit to an equation that uses 3.45 eV as the ZnTe Γ → X indirect band gap was not successful. This supports our interpretation of the data and indicates that the Γ → X band gap transition for ZnTe is about 3.05 eV.

Comparison of the reflectivity and photoluminescence data shows that the direct-to-indirect crossover occurs at $x \approx 0.28$. This result implies that $Be_{0.48}Zn_{0.52}Te$, which is the alloy composition that is lattice matched to InP, is an indirect semiconductor with a Γ → X indirect band gap of 2.77 eV and a Γ → Γ direct band gap of 3.14 eV. A previous report[5] predicted that the direct-to-indirect crossover for $Be_xZn_{1-x}Te$ alloy would occur at a much higher Be content ($x > 0.7$). This prediction was based on the assumption that the Γ → X ZnTe band gap is at 5.97 eV. Our data gives a clear evidence

of the position of the direct-to-indirect crossover and indicates that 5.97 eV is not the correct value for the $\Gamma \rightarrow X$ transition for ZnTe.

In summary, epitaxial layers of $Be_xZn_{1-x}Te$ were grown by MBE on InP substrates and their band structure and optical properties were investigated. A linear dependence of the Be content (in the log scale) on the Be (Zn) cell temperatures was observed indicating good control of the composition. Narrow x-ray rocking curves down to 72 arc sec with a low etch pit density of mid 10^5 cm $^{-2}$ were obtained for closely lattice matched epilayers suggesting high crystalline quality. Variations in $Be_xZn_{1-x}Te$ composition as a function of depth were observed in a few cases and attributed to the small fluctuations of substrate temperature during the growth. $Be_xZn_{1-x}Te$ layers under tensile strain exhibited less tendency to form misfit dislocations than layers under compressive strain. This was attributed to the enhanced lattice-hardening in layers with higher Be content. It was shown that $Be_xZn_{1-x}Te$ has a direct bandgap for low BeTe concentrations and becomes indirect, exhibiting a $\Gamma \rightarrow X$ character, for $x \geq 0.28$. The $\Gamma \rightarrow \Gamma$ direct band gap increases linearly with BeTe content at a rate of 18 meV for a change of 1% in BeTe content for the entire compositional range. The dependence of the indirect band gap on composition was also established and a good fit was obtained when a value

of 3.05 eV was used for the ZnTe Γ → X transition. Our results indicate that $Be_{0.48}Zn_{0.52}Te$, which is the composition that is lattice matched to InP, is an indirect semiconductor with a Γ → X indirect band gap of 2.77 eV, and a Γ → Γ direct band gap of 3.14 eV. Therefore, it is well suited for use as a p-type contact layer in LED structures emitting throughout the visible range.

Table 6-1 Parameters of $Be_xZn_{1-x}Te$ epilayers grown

Composition	Mismatch (%)	FWHM (arc sec)	EPD (cm^{-2})	Thickness (nm)
$Be_{0.38}Zn_{0.62}Te$	0.85 %	280	1.5×10^7	740
$Be_{0.4}Zn_{0.6}Te$	0.65 %	190	6.5×10^6	690
$Be_{0.46}Zn_{0.54}Te$	0.17 %	72	5×10^5	560
$Be_{0.51}Zn_{0.49}Te$	-0.06 %	78	5×10^5	680
$Be_{0.53}Zn_{0.47}Te$	-0.34 %	76	1.4×10^6	560
$Be_{0.58}Zn_{0.42}Te$	-0.78 %	91	4.5×10^6	690

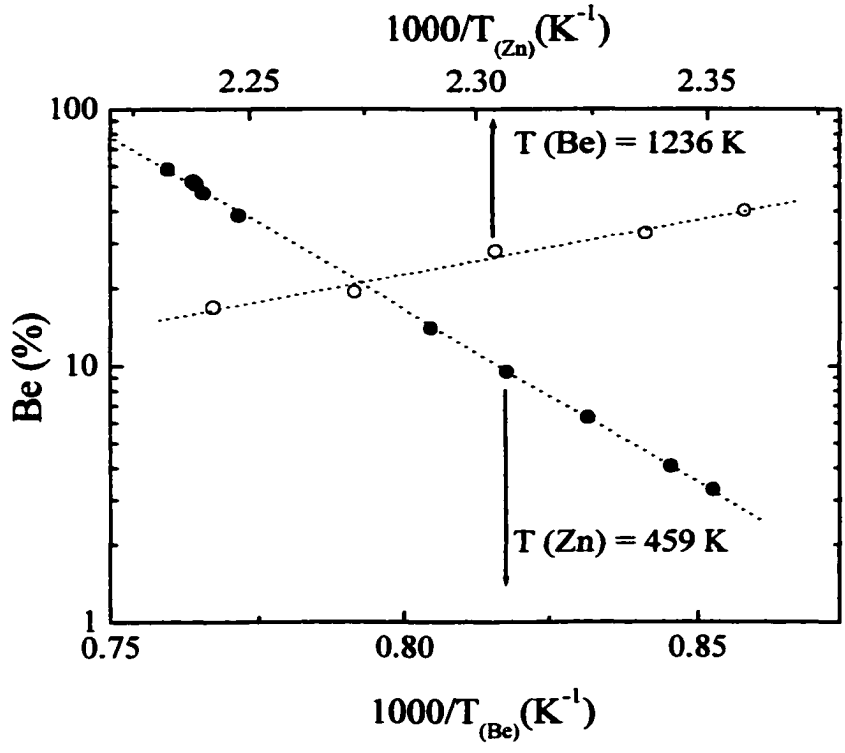

Fig. 6-1: Dependence of the Be content (x) on the Be (solid circles) and Zn (open circles) cell temperatures for $Be_xZn_{1-x}Te$ alloy. Dashed lines are linear fits.

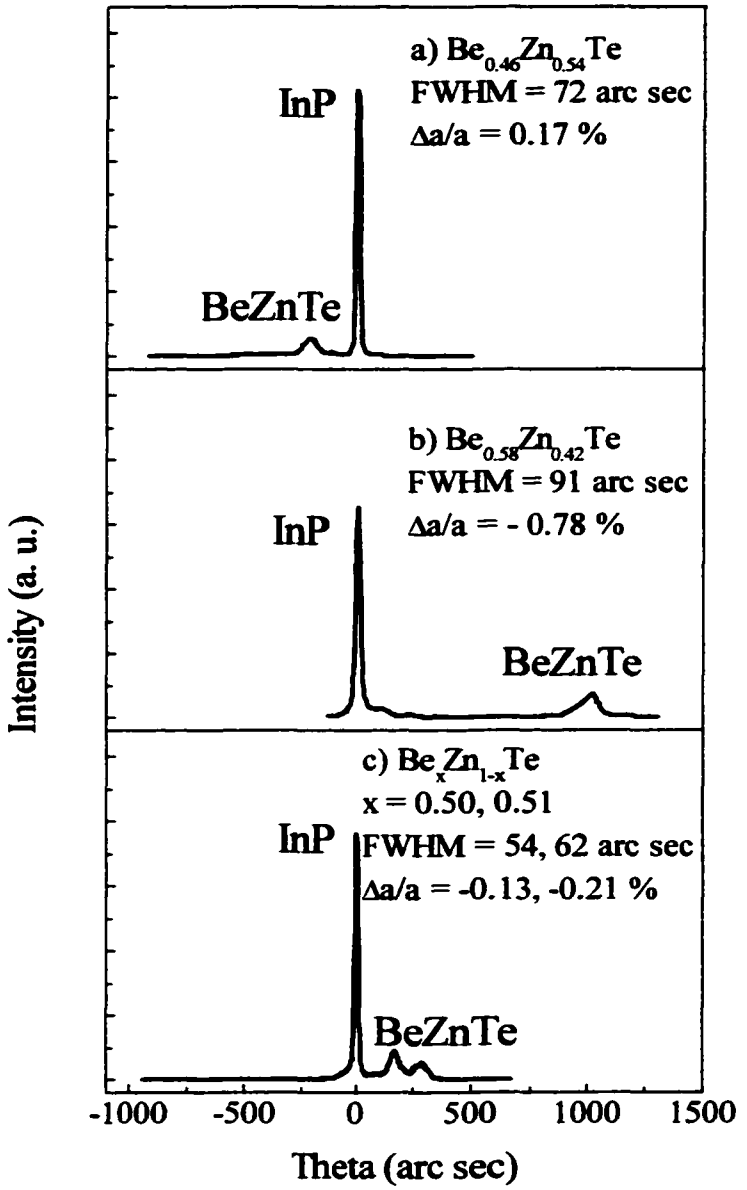

Fig. 6-2: (004) X-ray rocking curves for three $Be_xZn_{1-x}Te$ layers with different composition grown on InP substrates: (a) $Be_{0.46}Zn_{0.54}Te$, (b) $Be_{0.58}Cd_{0.42}Te$, and (c) $Be_xZn_{1-x}Te$ with x = 0.50, 0.51.

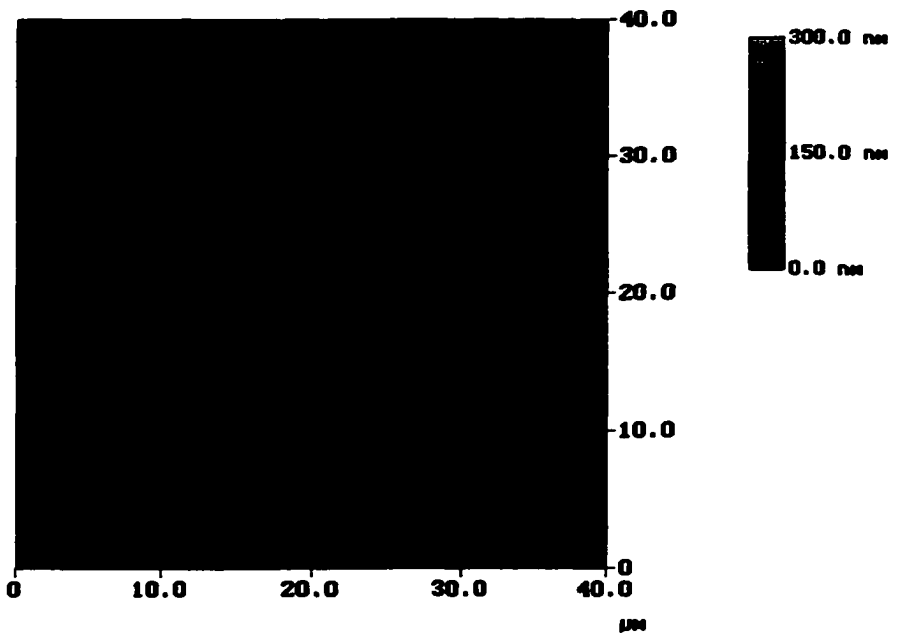

Fig. 6-3: Atomic force micrograph for a $Be_{0.51}Zn_{0.49}Te$ epilayer etched for 60 seconds in HCl (32 %).

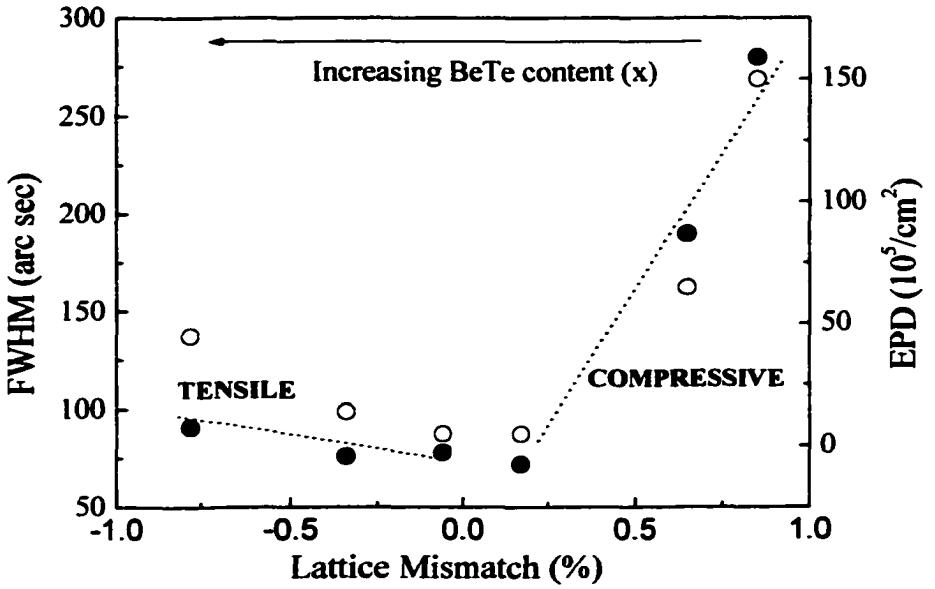

Fig. 6-4: Full width at half maximum (solid circles) and etch pit density (open circles) for $Be_xZn_{1-x}Te$ epilayers as a function of lattice mismatch to InP. Dashed lines are drawn for illustration.

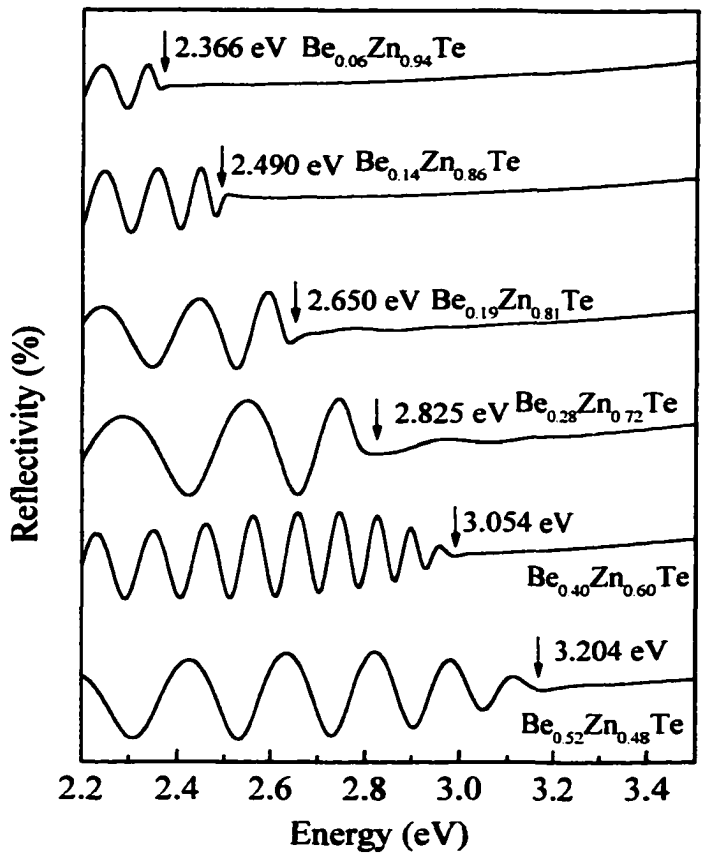

Fig. 6-5: Room temperature reflectivity spectra for several $Be_xZn_{1-x}Te$ alloys of different compositions.

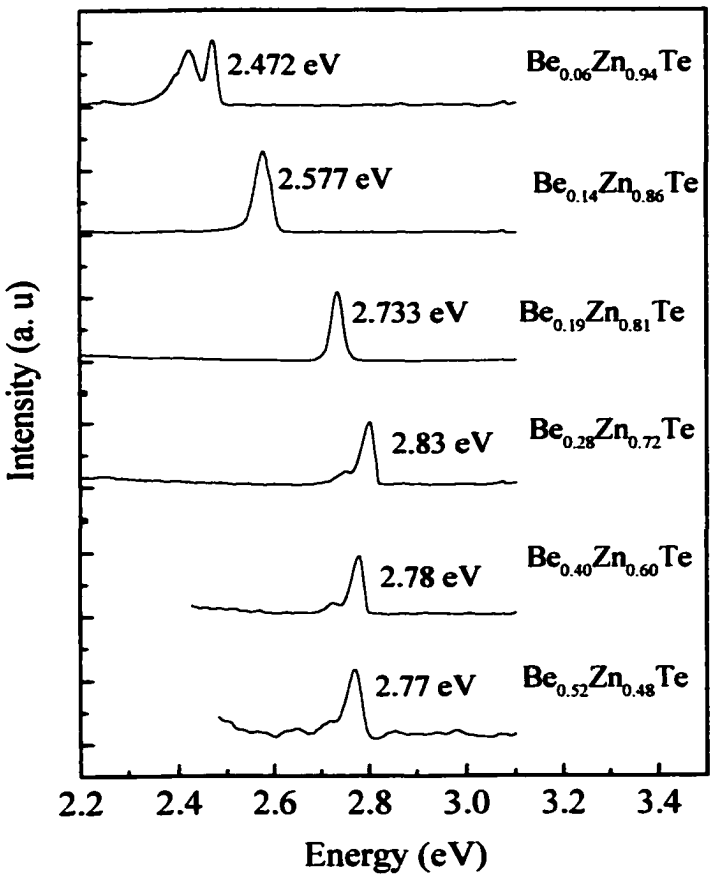

Fig. 6-6: Low temperature (6K) photoluminescence spectra for several $Be_xZn_{1-x}Te$ alloys of different compositions.

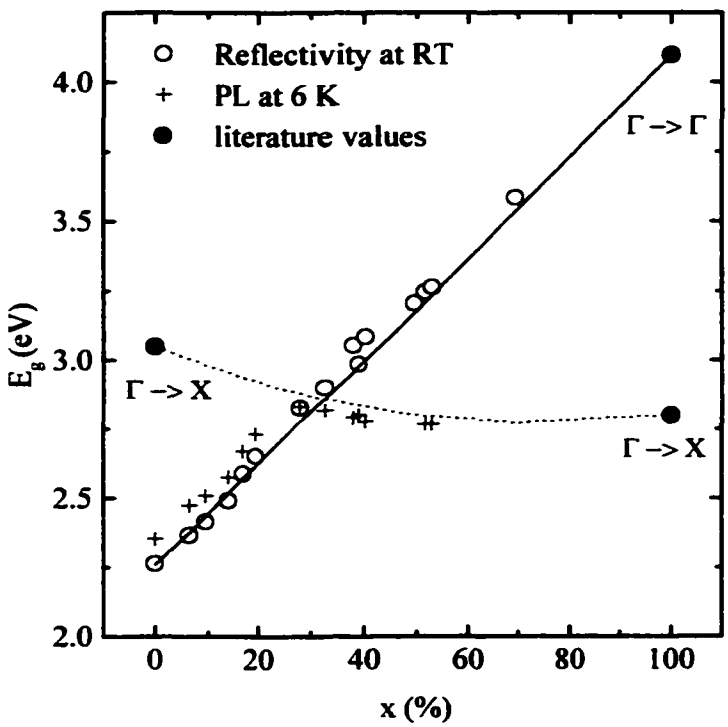

Fig. 6-7: Direct band gap at 298 K from reflectivity data (open circles) and PL energy at 6K (crosses) as a function of BeTe content (x) in $Be_xZn_{1-x}Te$. The dashed line is a fit for the Γ → X transition and the solid line is a fit for the direct band gap Γ → Γ transition of $Be_xZn_{1-x}Te$ alloys as a function of composition.

Chapter 7

Summary

The main purpose of the research presented in my dissertation was to grow and study new ZnCdMgSe-based structures and novel Be-based alloys that can be used to improve the quality of ZnBeCdSe-based LEDs. The following is the summary of my research:

- ZnCdMgSe-based distributed Bragg reflectors were grown. High crystalline quality was demonstrated by DCXRD measurements. A 95.5% reflectivity was obtained from a 16-period DBR structure. The optical and electrical properties of chlorine-doped n-type ZnCdSe/ZnCdMgSe DBR structures were also investigated. Reflectivity spectra, similar to those of undoped DBR structures with the same number of periods, were observed from the doped structures. High carrier concentration in the constituent layers was achieved. These results demonstrate that $Zn_xCd_yMg_{1-x-y}Se$ is a promising material system for the design of highly reflective, conductive DBRs for application in RCLEDs and other microcavity devices.
- Epitaxial layers of $Be_xZn_yCd_{1-x-y}Se$ were grown. High quality layers, that demonstrated narrow X-ray rocking curves and sharp, strong, and

excitonic PL emission lines, were obtained. The dependence of $Be_xCd_{1-x}Se$ band gap energy on composition was investigated and fitted to the quadratic equation. It was determined that $Be_{0.2}Cd_{0.8}Se$, which is the composition that is lattice matched to InP, have band gap energy of 2.128 eV at 10 K. These results suggest that $Be_xZn_yCd_{1-x-y}Se$ is an attractive material for lasers and LEDs emitting in the visible region of the spectrum.

- Quantum well structures having ZnCdMgSe barrier layers and $Be_{0.08}Cd_{0.92}Se$ QW layers were grown and their optical properties were investigated. Efficient excitonic emission in the red region of the spectrum was observed from a structure with 48-Å thick QW. Parameters that describe the temperature dependence of the QW emission were obtained. Our results indicate that $Be_xCd_{1-x}Se$ -based QW structures are attractive for application as red light emitters.
- Epitaxial layers of $Be_xZn_{1-x}Te$ were grown and their band structure and optical properties were investigated. It was shown that $Be_xZn_{1-x}Te$ has a direct band gap for low BeTe concentrations and becomes indirect, exhibiting a $\Gamma \rightarrow X$ character, for $x \geq 0.28$. Our results indicate that $Be_{0.48}Zn_{0.52}Te$, which is the composition that is lattice matched to InP, is an indirect semiconductor with a $\Gamma \rightarrow X$ indirect

band gap of 2.77 eV, and a $\Gamma \rightarrow \Gamma$ direct band gap of 3.14 eV. Therefore, it does not absorb visible light and can be used as a p-type contact layer.

As a conclusion, growth, crystalline properties, and band structure of the two new Be-based alloys were investigated. The band gap dependence on composition was explored and shown in Figure 7.1. Integration of these alloys with ZnCdMgSe-based LEDs and DBRs, as shown in Figure 7-2, will result in the RCLEDs that are expected to have better optical and electrical properties as well as will be less prone to degradation.

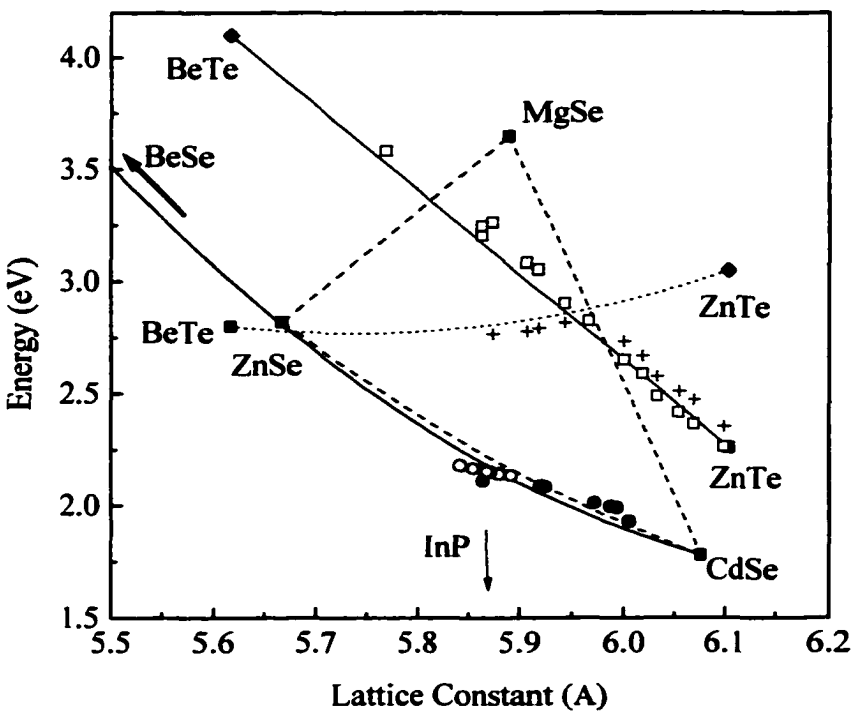

Fig. 7-1: Band gap energy versus lattice constant for wide band gap II-VI materials.

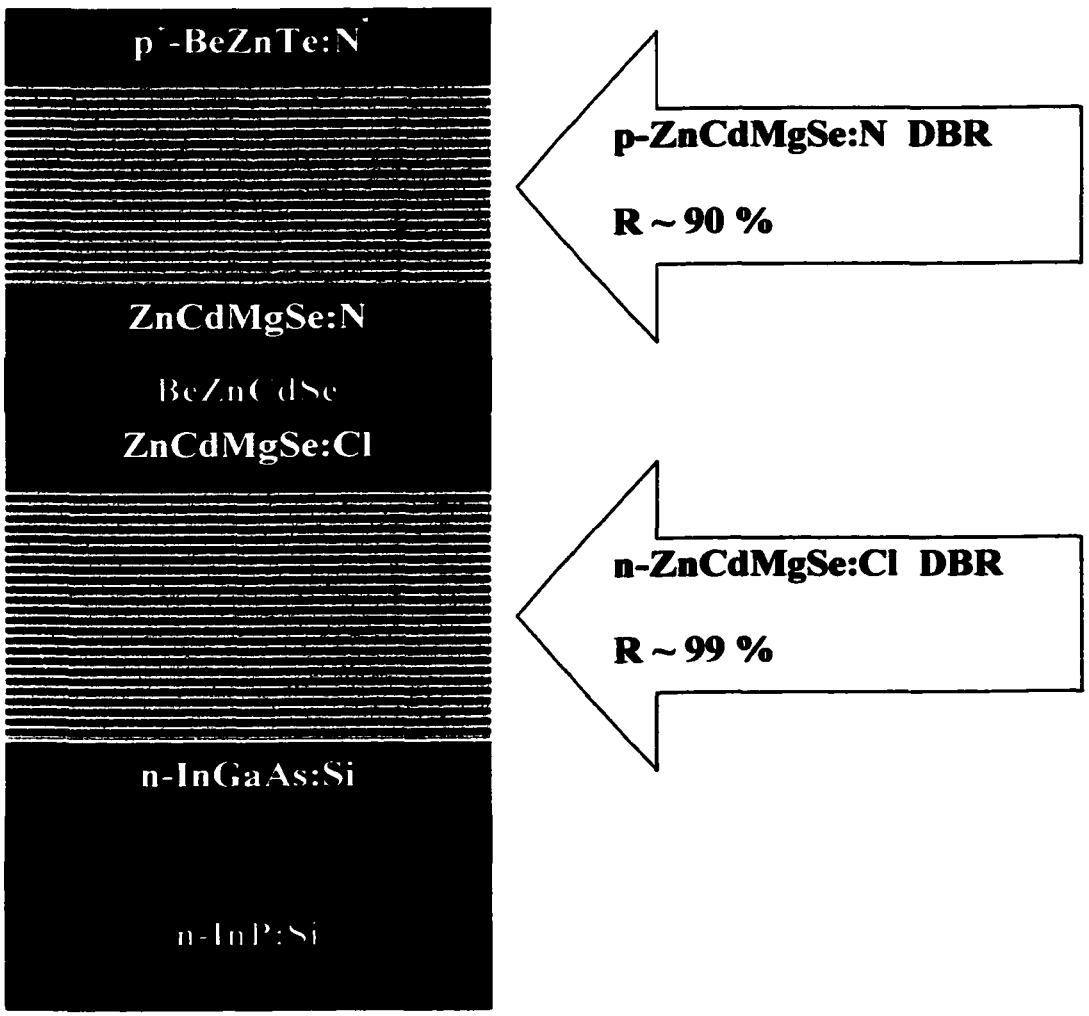

Fig. 7-2: The schematics of proposed RCLED.

Publications and conference presentations

Publications

1. *"Molecular beam epitaxy of ZnBeSe grown on GaAs with Be-Zn co-irradiation"*, S. P. Guo, Y. Luo, W. Lin, **O. Maksimov**, M. C. Tamargo, I. Kuskovsky, C. Tian, G. Neumark, J. Cryst. Growth. **208** (2000) 205.
2. *"Continuous wave and passively mode-locked operation of a cunyite (Cr^{4+}:Ca_2GeO_4) laser"*, B. Xu, M. Evans, V. Petricevic, S. P. Guo, **O. Maksimov**, M. C. Tamargo, R. R. Alfano, Appl. Optics. **39** (2000) 4975.
3. *"Distributed Bragg reflectors for visible range applications based on (Zn, Cd, Mg)Se lattice matched to InP"*, S. P. Guo, **O. Maksimov**, M. C. Tamargo, F. C. Peiris, J. K. Furdyna, Appl. Phys. Lett. **77** (2000) 4107.
4. *"Patterned three-color ZnCdSe/ZnCdMgSe quantum-well structures for integrated full color and white light emitters"*, Y. Luo, S. P. Guo, **O. Maksimov**, M. C. Tamargo, V. Asnin, F. H. Pollak, Y. C. Chen, Appl. Phys. Lett. **77** (2000) 4259.
5. *"Distributed Bragg reflectors based on (Zn, Cd, Mg)Se for use in the visible range applications "*, **O. Maksimov**, S. P. Guo, M. C. Tamargo, F. C. Peiris, J. K. Furdyna, J. Appl. Phys. **89** (2001) 2202.
6. *"Growth and characterization of BeCdSe alloys and BeCdSe/ZnCdMgSe quantum wells on InP substrates"*, **O. Maksimov**, S. P. Guo, M. C. Tamargo. Appl. Phys. Lett. **78** (2001) 2202.

7. *"High reflectivity symmetrically strained ZnCdMgSe-based distributed Bragg reflectors for current injection devices"*, **O. Maksimov**, S. P. Guo, M. C. Tamargo, F. C. Peiris, J. K. Furdyna, J. Vac. Sci. Tech. B. **19** (2001) 1479.
8. *"Red-green-blue light emitting diodes and distributed Bragg reflectors based on ZnCdMgSe lattice-matched to InP"*, M. C. Tamargo, S. P. Guo, **O. Maksimov**, Y. C. Chen, F. C. Peiris, J. K. Furdyna, J. Cryst. Growt **227/228** (2001) 710.
9. *"Direct-to-indirect band gap crossover for the BeZnTe alloy"*, **O. Maksimov** and M. C. Tamargo, Appl. Phys. Lett. **79** (2001) 782.
10. *"Effects of Be on the II-VI GaAs interface and CdSe quantum dot formation"*, S. P. Guo, X. X. Zhou, **O. Maksimov**, M. C. Tamargo, C. Chi, A. Couzis, C. Maldarelli, J. Vac. Sci. Tech. B. **19** (2001) 1479.
11. *"Optical properties of BeCdSe/ZnCdMgSe strained quantum well structures"*, **O. Maksimov**, S. P. Guo, M. Munoz, and M. C. Tamargo, J. Appl. Phys **90** (2001) 5135.
12. *"Be-chalcogenide alloys for improved R-G-B LEDs: $Be_xZn_yCd_{1-x-y}Se$ on InP"*, **O. Maksimov**, S. P. Guo, M. C. Tamargo, accepted by Phys. Status Solidi (a).
13. *"Heavily p-type doped ZnSe and ZnBeSe"*, I. L. Kuskovsky, Y. Gu, C. Tian, G. F. Neumark, S. P. Guo, W. Lin, **O. Maksimov**, M. C. Tamargo, A. N. Alyoshin, V. M. Belous, accepted by Phys. Status Solidi (a).
14. *"Properties of MBE grown ZnBeSe: study of isoelectronic traps and of dopant behavior"*, I. L. Kuskovsky, Y. Gu, M. van der Voort, G. F. Neumark, S. P. Guo, **O. Maksimov**, M. C. Tamargo, accepted by Phys. Status Solidi (a).

15. *"Molecular beam epitaxy growth and properties of $Be_xZn_{1-x}Te$ alloys for optoelectronic devices"*, **O. Maksimov**, Martin Muñoz, M. C. Tamargo, J. Lau, and G. F. Neumark, submitted to J. Vac. Sci. Tech B.

Conference presentations

1. *"ZnCdMgSe-based distributed Bragg reflectors grown by molecular beam epitaxy"*, **O. Maksimov**, S. P. Guo, Y. Y. Luo, W. Lin, M. C. Tamargo, 19th North American Conference on MBE, Oct. 4-7, 2000, Arizona State University, Tempe, AZ.

2. *"Growth and properties of ZnBeCdSe alloys for light emitting devices"*, **O. Maksimov**, S. P. Guo, M. C. Tamargo, American Physical Society March Meeting, March 17-21, 2001, Seattle, WA.

3. *"Be-chalcogenide alloys for improved R-G-B LEDs: $Be_xZn_yCd_{1-x-y}Se$ and $Be_xZn_{1-x}Te$ on InP"*, **O. Maksimov**, X. Zhou, S. P. Guo, M. C. Tamargo, 10th International Conference on II-VI Compounds, September 9-14, 2001, Bremen, Germany.

4. *"Molecular beam epitaxy growth and properties of $Be_xZn_{1-x}Te$ alloys for optical devices"*, **O. Maksimov** and M. C. Tamargo, 20th North American Conference on MBE, Oct. 1-3, 2001, Brown University, Providence, RI.

References

Chapter 1

1. S. Nakamura, M. Senoh, S. I. Nagahama, N. Iwasa, T. Yamada, T. Matsushita, Y. Sugimoto, H. Kiypku, Appl. Phys. Lett. **70**, 1417 (1997).

2. S. Taniguchi, T. Hino, S. Itoh, K. Nakano, N. Nakayama, A. Ishibashi, M. Ikeda, Electron. Lett. **32**, 552 (1996).

3. K. Koga, T. Yamaguchi, Prog. Crystal Growth Charact. **23**, 127 (1991).

4. M. C. Tamargo, A. Cavus, L. Zeng, N. Dai, N. Bamba, A. Gray, F. Semendy, W. Krystek, F. H. Pollak, J. Electron. Mater. **25**, 259 (1996).

5. M. C. Tamargo, W. Lin, S. P. Guo, Y. Guo, Y. Luo, Y. C. Chen, J. Crystal Growth **214/215**, 1058 (2000).

6. W. Faschinger, J. Nurnberger, Appl. Phys. Lett. **77**, 187 (2000).

7. W. Shinozaki, I. Nomura, H. Shimbo, H. Hattori, T. Sano, S. B. Che, A. Kikuchi, K. Shimomura, K. Kishino, Jpn. J. Appl. Phys. **38**, 2598 (1999).

8. Y. Luo, S. P. Guo, O. Maksimov, M. C. Tamargo, V. Asnin, F. H. Pollak, Y. C. Chen, Appl. Phys. Lett. **77**, 4259 (2000).

9. W. Lin, B. X. Yang, S. P. Guo, A. Elmoumni, F. Fernandez, M. C. Tamargo, Appl. Phys. Lett. **75**, 2608 (1999).

10. E. F. Schubert, Y. H. Wang, A. Y. Cho, L. W. Tu, G. J. Zydzik, Appl. Phys. Lett. **60**, 921 (1992).

11. U. Zehnder, D. R. Yakovlev, W. Ossau, T. Gerhard, F. Fischer, H. J. Lugauer, M. Keim, G. Reuscher, A. Waag, Th. Litz, K. Herz, G. Bacher, A. Forchel, G. Landwehr, J. Crystal Growth **184/ 185**, 541 (1998).

12. S. V. Ivanov, A. A. Toropov, T. V. Shubina, A. V. Lebedev, S. V. Sorokin, A. A. Sitnikova, P. S. Kop'ev, G. Reuscher, M. Keim, F. Bensing, A. Waag, G. Landwehr, G. Pozina, J. P. Bergman, B. Monamer, J. Crystal Growth **214/ 215**, 109 (2000).

13. M. Takizawa, I. Nomura, S. B. Che, A. Kikuchi, K. Shimomura, K. Kishino, J. Crystal Growth **227/228**, 661 (2001).

14. A. Waag, Th. Litz, F. Fischer, H. J. Lugauer, T. Baron, K. Schull, U. Zehnder, T. Gerhard, U. Lunz, M. Keim, G. Reuscher, G. Landwehr, J. Crystal Growth **184/ 185**, 1 (1998).

15. S. B. Che, I. Nomura, W. Shinozaki, A. Kikuchi, K. Shimomura, K. Kishino, J. Crystal Growth. **214/215**, 321 (2000).

16. M. W. Cho, S. K. Hong, J. H. Chang, S. Saeki, M. Nakajima, T. Yao, J. Crystal Growth. **214/215**, 487 (2000).

17. A. Waag, F. Fischer, H. J. Lugauer, Th. Litz, J. Laubender, U. Lunz, U. Zehnder, W. Ossau, T. Gerhardt, M. Moller, G. Landwehr, J. Appl. Phys. **80**, 792 (1996).

Chapter 2

1. A. Y. Cho, Thin Solid Films **100,** 291 (1983).

2. A. Y. Cho and J. R. Arthur, Prog. Solid. State Chem. **10**, 157 (1975).

3. A. Y. Cho, J. Vac. Sci. Technol. **8**, 31 (1971).

4. J. H. Neave and B. A. Joyce, J. Cryst. Growth, **44**, 387 (1978).

5. H. H. Farrel, M. C. Tamargo, J. H. de Miguel, F. S. Turso, D. M. Hwang, and R. E. Nahory, J. Appl. Phys. **69**, 7021 (1991).

6. J. H. Neave and B. A. Joyce, Appl. Phys. **A 31**, 1 (1983).

7. A. Krost, G. Bauer, J. Woitok, *High Resolution X-ray Diffraction*, in *Optical Characterization of Epitaxial Semiconductor Layers*, Springer, Berlin (1996).

8. K. Uesugi, T. Obinata, I. Suemune, H. Kumano, J. Nakahara, Appl. Phys. Lett. **68**, 844 (1996).

9. L. Pavesi, M. Guzzi, J. Appl. Phys. **75**, 4779 (1994).

10. H. G. Tompkins and W. A. McGahan, *Spectroscopic Ellipsometry and Reflectometry*, John Wiley and Sons, NY (1999)

11. A. Cavus, L. Zeng, B. X. Yang, N. Dai, M. C. Tamargo, N. Bambha, F. Semendy, J. Cryst. Growth, **175/176**, 558 (1997).

12. L. Zeng, S. P. Guo, Y. Y. Luo, W. Lin, M. C. Tamargo, H. Xing, and G. S. Cargill III, J. Vac. Sci. Technol. **B 17**, 1255 (1999).

Chapter 3

1. E. F. Schubert, Y. H. Wang, A. Y. Cho, L. W. Tu, and G. J. Zydzik, Appl. Phys. Lett. **60**, 921 (1992).

2. A. Convertino, A. Valentini, T. Ligonza, R. Cingolani, Appl. Phys. Lett. **71**, 732 (1997).

3. V. Bardinal, R. Legros, and C. Fontaine, Appl. Phys. Lett. **67**, 3390 (1995).

4. T. Anan, H. Shimomura, and S. Sugou, Electron. Lett. **30**, 2138 (1994).

5. O. Blun, M. J. Hafich, J. F. Klem, and K. L. Lear, Appl. Phys. Letters. **67**, 3233 (1995).

6. F. C. Peiris, S. Lee, U. Bindley, and J. K. Furdyna, Semicond. Sci. Technol. **14**, 878 (1999).

7. F. C. Peiris, S. Lee, U. Bindley, and J. K. Furdyna, J. App. Phys. **86**, 719 (1999).

8. A. Cavus, L. Zeng, M. C. Tamargo, N. Bamba, F. Semendy, and A. Gray, Appl. Phys. Lett. **68**, 3446 (1996).

9. L. Zeng, S. P. Guo, Y. Y. Luo, M. C. Tamargo, H. Xing, and G. S. Cargill III, J. Vac. Sci. Technol. **B 17**, 1255 (1994).

10. M. C. Tamargo, M. J. S. P. Brasil, R. E. Nahory, R. J. Martin, A. L. Weaver, and H. L. Gilchrist, Semicond. Sci. Technol. **6**, A8 (1991).

11. F. C. Peiris, J. K. Furdyna, S. P. Guo, M. C. Tamargo; unpublished.

12. F. C. Peiris, S. Lee, V. Bindley, and J. K. Furdyna, J. App. Phys. **84**, 5194 (1998).

13. L. Zeng, A. Cavus, B. X. Yang, M. C. Tamargo, N. Bamba, F. Semendy, and A. Gray, J. Crystal Growth, **175**, 541 (1997).

14. M. Born and F. Wolf, *Principles of Optics*, 3rd ed., p. 125, Pergamon, NY (1965).

15. W. Lin, S. P. Guo, M. C. Tamargo, J. Vac. Sci. Technol. B **18**, 1534 (2000).

16. K. Tai, L. Yang, J. D. Wynn, and A. Y. Cho, Appl. Phys. Lett. **56**, 2496 (1990).

17. E. F. Schubert, L. W. Tu, G. J. Zydzik, R. F. Kopf, A. Benvenuti, M. R. Pinto, Appl. Phys. Lett. **60**, 466 (1992).

Chapter 4

1. M. C. Tamargo, A. Cavus, L. Zeng, N. Dai, N. Bambha, A. Gray, F. Semendy, W. Krystek, F. H. Pollak, J. Electron. Mat. **25** (1996) 259.

2. Y. Luo, S. P. Guo, O. Maksimov, M. C. Tamargo, V. Asnin, F. H. Pollak, Y. C. Chen, Appl. Phys. Lett .**77**, 4259 (2000).

3. C. Verie, in *Semiconductor Heteroepitaxy*, B. Gil and R. L. Aulombard (Eds.), World Scientific (1995) p. 73.

4. A. Waag, Th. Litz, F. Fischer, H. J. Lugauer, T. Baron, K. Schull, U. Zehnder, T. Gerhard, U. Lunz, M. Keim, G. Reuscher, G. Landwehr, J. Crystal Growth **184/ 185**, 1 (1998).

5. K. Mauyama, K. Suto, J. Nishizawa, J. Crystal Growth. **214/215**, 104 (2000).

6. S. V. Ivanov, A. A. Toporov, T. V. Shubina, A. V. Lebedev, S. V. Sorokin, A. A. Sitnikova, P. S. Kop'ev, G. Reuscher, M. Keim, F. Bensing,

A. Waag, G. Landwehr, G. Pozina, J. P. Bergman, B. Monamer, J. Crystal Growth **214/ 215**, 109 (2000).

7. L. Zeng, S. P. Guo, Y. Y. Luo, W. Lin, M. C. Tamargo, H. Xing, G. S. Cargill III, J. Vac. Sci. Technol, B **17**, 1255 (1999).

8. L. Zeng, B. X. Yang, M. C. Tamargo, E. Snoeks, L. Zhao, Appl. Phys. Lett. **72**, 1317 (1998).

9. J. X. Shen, R. Pittini, Y. Oka, S. P. Guo, M. C. Tamargo, Appl. Phys. Lett. **75**, 3494 (1999).

10. M.C. Tamargo, S. P. Brasil, R. E. Nahory, R. J. Martin, A. L. Weaver, H. L. Gilchrist, Semicond. Sci. Technol. **6**, A8 (1991).

11. K. Wilmers, T. Wethkamp, N. Esser, C. Cobet, W. Richter, M. Cardona, V. Wagner, H. Lugauer, F. Fischer, T. Gerhard, M. Keim, Phys. Rev. B **59**, 10071 (1999).

12. O. V. Nekrutina, S. V. Sorokin, V. A. Kaigorodov, A. A. Sitnikova, T. V. Shubina, A. A. Toropov, S. V. Ivanov, P. S. Kop'ev, G. Reuscher, V. Wagner, J. Geurts, A. Waag, and G. Landwehr, Semiconductors **35**, 520 (2001).

Chapter 5

1. R. Cingolani, F. Sogawa, Y. Arakawa, L. Vanzetti, L. Sorba, A. Franciosi, Appl. Phys. Lett. **73**, 148 (1998).

2. H. Kalt, J. Collet, S. D. Baranovskii, R. Saleh, P. Thomas, L. S. Dang, J. Cilbert, Phys. Rev. B **45**, 4253 (1992).

3. M. Umlauff, J. Hoffmann, H. Kalt, W. Langbein, J. M. Hvam, M. Scholl, J. Sollner, M. Heuken, B. Jobst, D. Hommel, Phys. Rev. B **57**, 1390 (1998).

4. H. Mathieu, P. Lafebvre, P. Christol, Phys. Rev. B **54**, 4092 (1992).

5. H. T. Grahn, *Introduction to Semiconductor Physics* (World Scientific, Singapore, 1999).

6. A. Cavus, L. Zeng, M. C. Tamargo, N. Bambha, F. Semendy, A. Gray, Appl. Phys. Lett. **68**, 3446 (1996).

7. S. P. Guo, L. Zeng, M. C. Tamargo, Appl. Phys. Lett. **78**, 1 (2001).

8. E. Oh, S. D. Lee, H. D. Jung, J. P. Kim, M. D. Kim, B. J. Kim, J. K. Ji, H. S. Park, T. I. Kim, S. V. Ivanov, A. A. Toropov, T. V. Shubina, Appl. Phys. Lett. **80**, 5951 (1996).

9. R. P. Stanley, J. Hegarty, R. D. Feldman, R. F. Austin, Appl. Phys. Lett. **53**, 1417 (1988).

10. S. Rudin, T. L. Reinecke, B. Segall, Phys. Rev. B **42**, 11218 (1990).

11. L. Malikova, W. Krystek, F. H. Pollak, N. Dai, A. Cavus, M. C. Tamargo, Phys. Rev. B **54**, 1819 (1996) and references there in.

12. U. Woggon, F. Gindele, W. Langbein, J. M. Hvam, Phys. Rev. B **61**, 1935 (2000).

13. T. Miyajima, F. P. Logue, J. F. Donegan, J. Hegarty, H. Okuyama, A. Ishibashi, Y. Mori, Appl. Phys. Lett. **66**, 180 (1995).

14. C. W. Chang, H. C. Yang, C. H. Chen, H. J. Chang, Y. F. Chen, J. Appl. Phys. **89**, 3725 (2001).

15. V. P. Varshni, Physica, **34**, 149 (1967).

16. L. Vina, S. Logothetidis, M. Cardona, Phys. Rev. B 30, 1979 (1984).

Chapter 6

1. M. C. Tamargo, W. Lin, S. P. Guo, Y. Guo, Y. Luo, Y. C. Chen, J. Crystal Growth. **214/215**, 1058 (2000).

2. W. Faschinger, J. Nurnberger, App. Phys. Lett.**77**, 187 (2000).

3. W. Shinozaki, I. Nomura, H. Shimbo, H. Hattori, T. Sano, S.B. Che, A. Kikuchi, K. Shimomura, K. Kishino, Jpn. J. Appl. Phys. **38**, 2598 (1999).

4. W. Lin, B. X. Yang, S. P. Guo, A. Elmoumni, F. Fernandez, M. C. Tamargo, Appl. Phys. Lett. **75**, 2608 (1999).

5. S. B. Che, I. Nomura, W. Shinozaki, A. Kikuchi, K. Shimomura, K. Kishino, J. Crystal Growth. **214/215**, 321 (2000).

6. M. W. Cho, S. K. Hong, J. H. Chang, S. Saeki, M. Nakajima, T. Yao, J. Crystal Growth. **214/215**, 487 (2000).

7. A. Waag, F. Fischer, H. J. Lugauer, Th. Litz, J. Laubender, U. Lunz, U. Zehnder, W. Ossau, T. Gerhardt, M. Moller, G. Landwehr, J. Appl. Phys. **80**, 792 (1996).

8. A. Waag, Th. Litz, F. Fischer, H. J. Lugauer, T. Baron, K. Schüll, U. Zehnder, T. Gerhard, U. Lunz, M. Keim, G. Reuscher, G. Landwehr, J. Crystal Growth. **184/185**, 1 (1998).

9. S. P. Guo, Y. Luo, W. Lin, O. Maksimov, M. C. Tamargo, I. Kuskovsky, C. Tian, G. F. Neumark, J. Crystal Growth. **208**, 205 (2000).

10. F. Fisher, M. Keller, T. Gerhard, T. Behr, T. Litz, H. J. Lugauer, M. Keim, G. Reuscher, T. Baron, A. Waag, G. Landwehr, J. Appl. Phys. **84**, 1650 (1998).

11. M. Shiraishi, S. Tomiya, S. Tanigachi, N. Nakano, A. Ishibashi, M. Ikeda, Phys. Stat. Sol. (a) **152**, 377 (1995).

12. F. C. Peiris, U. Bindley, J. K. Furdyna, H. Kim, A. K. Ramdas, M. Grimsditch, Appl. Phys. Lett. **79**, 473 (2001).

13. K. Mauyama, K. Suto, J. Nishizawa, J. Crystal Growth. **214/215**, 104 (2000).

14. G. D. Lee, M. H. Lee, J. Ihm, Phys. Rev. B **52**, 1459 (1995), and references there in.

15. O. Zakharov, A. Rubio, X. Blase, M. L. Cohen, S. G. Louie, Phys. Rev. B **50**, 10780 (1994).

16. K. Sato, S. Adachi, J. Appl. Phys. **73**, 926 (1993).

17. K. Suzuki, S. Adachi, J. Appl. Phys. **82**, 1320 (1997).